Technische Universität München
TUM School of Natural Sciences

The Chemistry and Physics of Chemically Fueled Complex Coacervate Droplets

Carsten Adam Donau

Vollständiger Abdruck der von der TUM School of Natural Sciences der Technischen Universität München zur Erlangung eines

Doktors der Naturwissenschaften (Dr. rer. nat.)

genehmigten Dissertation.

Vorsitz: Prof. Dr. Matthias J. Feige

Prüfer*innen der Dissertation:

1. Prof. Dr. Job Boekhoven
2. Prof. Dr. Cathleen Zeymer
3. Prof. Christine Keating, Ph. D.

Die Dissertation wurde am 26.10.2022 bei der Technischen Universität München eingereicht und durch die TUM School of Natural Sciences am 01.12.2022 angenommen.

Technische Universität München
Chair of Supramolecular Chemistry

The Chemistry and Physics of Chemically Fueled Complex Coacervate Droplets

Carsten Adam Donau
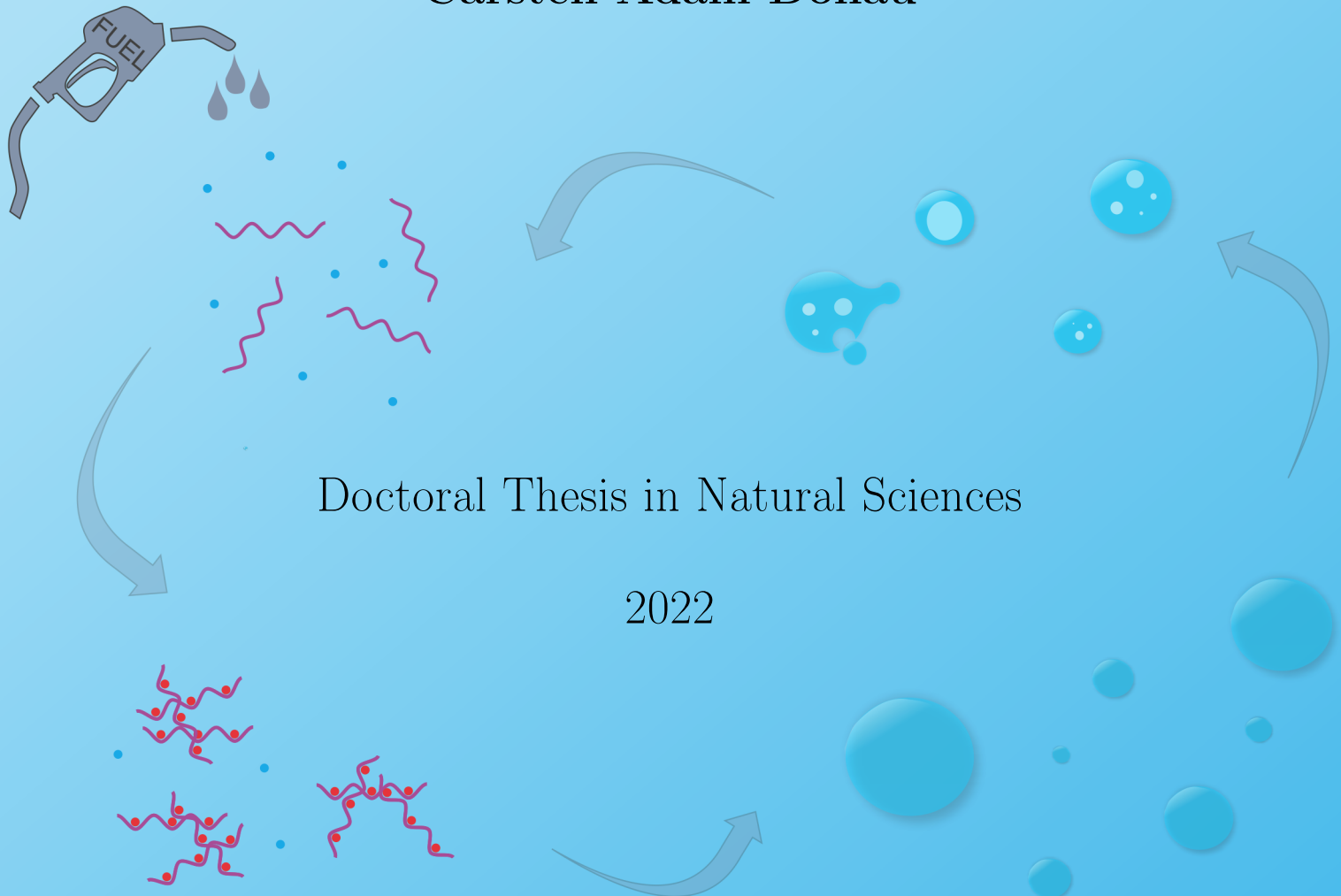
Doctoral Thesis in Natural Sciences

2022

You can have a Ph.D. and still be an idiot! Education and intelligence are two different things.

You're under no obligation to remain the same person you were a year ago, a month ago, or even a day ago. You are here to create yourself, continuously.

<div align="right">

R. Feynman

</div>

Scientists would rather use each other's toothbrushes than use each other's terminology.

<div align="right">

W. Feldberg

</div>

Man kann einen Doktortitel haben und trotzdem ein Idiot sein! Bildung und Intelligenz sind zwei verschiedene Dinge.

Du bist nicht verpflichtet, die gleiche Person zu bleiben, die du vor einem Jahr, vor einem Monat oder sogar vor einem Tag warst. Du bist hier, um dich selbst zu erschaffen, und das kontinuierlich.

<div align="right">

R. Feynman

</div>

Wissenschaftler würden lieber die Zahnbürsten ihrer Kollegen benutzen, als deren Terminologie zu verwenden.

<div align="right">

W. Feldberg

</div>

Abstract

In recent years, the discovery of liquid droplets as a tool to organize molecules and biochemical reactions in the cytosol led to a better understanding of how today's cells regulate reaction cascades spatiotemporally. At the same time, a new interest in synthetic liquid droplets emerged both as a model of these droplets in our cells or of a prebiotic compartment at the origin of life.

This thesis aimed to create a new chemically fueled droplet model to verify predictions from theory-based studies. I show insights into how such droplets can self-divide, how new phase transitions emerge and how such droplets transition into stable spherical shells. This model is useful to understand how cellular droplets are regulated by chemical reactions and the possible role of droplets as prebiotic compartments regulated by simple forms of metabolism.

I start my thesis with a brief description of liquid droplets in biology and at the origin of life (chapter 1). In chapter 2, I discuss the principles of phase separation of aqueous droplets in water and elaborate on how such droplets can be designed in the laboratory. I emphasize the role of chemical reactions in regulating droplet properties and highlight exciting behaviors that emerge when droplet formation and decay are coupled to a chemical reaction cycle, *i.e.*, chemically fueled droplets (chapter 3). In chapter 4, I discuss what aspects of current experimental models are missing and outline the aims of this thesis.

Specifically, the first aim of this thesis was to create a new liquid droplet model based on complex coacervation that is regulated by a chemical reaction cycle. I describe peer-reviewed work in chapter 5 where I designed such chemically fueled droplets based on a short peptide and homopolymeric RNA. The chemical reaction cycle temporarily increases the peptide's affinity for the polyanion and activates it for phase separation. As a result, droplets were formed that closely followed the kinetics of the reaction cycle. Excitingly, these droplets split into fragments and formed vacuoles in their dissolution pathway. Finally, functional RNA could remain in its active folded state inside these droplets. The transient up-concentration of functional RNA shows that the droplets can be considered potential prebiotic model compartments where the interior of the droplet offers an environment for the evolution of more complex molecules. Also, these droplets are regulated by chemical reactions, making them a great model for similar droplets in today's cells.

The second aim of this thesis was to understand how chemical reactions can affect the internal organization of droplets. For that, I used the droplet model from chapter 5 in the presence of a second polyanion in solution, *i.e.*, a synthetic polymer (chapter 6). In this peer-reviewed work, the two polyanions compete for the activated peptide, resulting in droplets with or without subcompartmentalization leading to distinct regimes inside the phase diagram. I identify new transitions that can only occur under kinetic control. Finally, the liquidity of the droplets is controlled by the

chemical reaction cycle, similar to active cellular processes regulating membraneless organelles. This work emphasizes the role of kinetics in the organization of multiple phases in droplets.

The third aim of this thesis was to build a droplet model that is continuously fueled so that it can be compared to the conditions in numerical simulations on chemically fueled droplets. In chapter 7, I describe unpublished work on continuously fueled droplets where I study surprising non-equilibrium transitions based on the droplet design of chapters 5 and 6. I discuss the formation of spherical shells from droplets that is size-dependent and not possible for droplets close to thermodynamic equilibrium. This work highlights how the behavior of assemblies changes when their properties are coupled to non-equilibrium processes.

The work presented in this thesis shows one of the first examples of coacervate droplets being regulated by chemical reactions and the first to demonstrate this without the need for enzymes or changes in pH. This droplet model thus fulfills one important aspect that is needed to understand cellular droplets, *i.e.*, their regulation by active processes. Also, it can serve as an attractive model to study potential prebiotic compartments that harbor primitive forms of metabolism where chemical energy is transduced.

Zusammenfassung

In den letzten Jahren hat die Entdeckung von flüssigen Tröpfen als Instrument zur Organisation von Molekülen und biochemischen Reaktionen im Zytosol zu einem besseren Verständnis geführt, wie die heutigen Zellen Reaktionskaskaden räumlich und zeitlich regulieren. Gleichzeitig erwachte ein neues Interesse an synthetischen Modellen für diese Tröpfchen in unseren Zellen sowie für präbiotische Kompartimente am Ursprung des Lebens.

Ziel dieser Arbeit war es, ein neues chemisch angetriebenes Tröpfchenmodell zu entwerfen, um die Vorhersagen aus theoriegestützten Studien zu überprüfen. Ich zeige, wie sich solche Tröpfchen selbst aufspalten können, wie neue Phasenübergänge entstehen und wie solche Tröpfchen in stabile kugelförmige Schalen übergehen. Dieses Modell ist nützlich, um zu verstehen, wie zelluläre Tröpfchen durch chemische Reaktionen reguliert werden, sowie die mögliche Rolle von Tröpfchen als präbiotische Kompartimente, die durch einfache metabolische Prozesse reguliert werden.

Ich beginne meine Arbeit mit einer kurzen Beschreibung von flüssigen Tröpfen in der Biologie und beim Ursprung des Lebens (Kapitel 1). In Kapitel 2 diskutiere ich die Prinzipien der Phasentrennung von wässrigen Tröpfchen in Wasser und erläutere, wie solche Tröpfchen im Labor hergestellt werden können. Ich betone die Rolle chemischer Reaktionen bei der Regulierung der Tröpfcheneigenschaften und zeige aufregende Verhaltensweisen auf, die sich ergeben, wenn die Bildung und der Zerfall von Tröpfchen an einen chemischen Reaktionszyklus gekoppelt sind, d.h. chemisch angetriebene Tröpfchen (Kapitel 3). In Kapitel 4 erörtere ich, welche Aspekte in derzeitigen experimentellen Modellen fehlen, und skizziere die Ziele dieser Arbeit.

Konkret bestand das erste Ziel dieser Arbeit darin, ein neues Modell für flüssige Tröpfen zu entwickeln, das auf komplexer Koazervation beruht und durch einen chemischen Reaktionszyklus gesteuert wird. In Kapitel 5 beschreibe ich eine wissenschaftlich begutachtete Publikation, in der ich solche chemisch angetriebenen Tröpfchen auf der Grundlage eines kurzen Peptids und homopolymerer RNA entwickelt habe. Der chemische Reaktionszyklus erhöht vorübergehend die Affinität des Peptids für das Polyanion und aktiviert es für die Phasentrennung. Infolgedessen bildeten sich Tröpfchen, die der Kinetik des Reaktionszyklus genau folgten. Spannenderweise spalteten sich diese Tröpfchen in Fragmente und bildeten Vakuolen während ihres Zerfalls. Schließlich konnte funktionelle RNA in diesen Tröpfchen in ihrem aktiven, gefalteten Zustand verbleiben. Die vorübergehende Anreicherung von funktioneller RNA zeigt, dass die Tröpfchen als potenzielle präbiotische Modellkompartimente betrachtet werden können, in denen das Innere der Tröpfchen eine Umgebung für die Entwicklung komplexerer Moleküle bietet. Außerdem werden diese Tröpfchen durch chemische Reaktionen reguliert, was sie zu einem hervorragenden Modell für ähnliche Tröpfchen in heutigen Zellen macht.

Das zweite Ziel dieser Arbeit war es, zu verstehen, wie chemische Reaktionen

die innere Organisation von Tröpfchen beeinflussen können. Dazu verwendete ich das Tröpfchenmodell aus Kapitel 5 in Anwesenheit eines zweiten Polyanions in Lösung, *d.h.*, eines synthetischen Polymers (Kapitel 6). In dieser wissenschaftlich begutachteten Publikation konkurrieren die beiden Polyanionen um das aktivierte Peptid, was zu unterschiedlichen Zuständen im Phasendiagramm führt, wie zum Beispiel Tröpfchen mit oder ohne Subkompartimenten. Ich identifiziere neue Übergänge, die nur unter kinetischer Kontrolle auftreten können. Schließlich wird die Liquidität der Tröpfchen durch den chemischen Reaktionszyklus gesteuert, ähnlich wie aktive zelluläre Prozesse, die membranlose Organellen regulieren. Diese Arbeit unterstreicht die Rolle von kinetischen Prozessen bei der Organisation von Tröpfchen mit mehreren Phasen.

Das dritte Ziel dieser Arbeit bestand darin, ein Tröpfchenmodell zu erstellen, das kontinuierlich mit chemischen Treibstoff versorgt wird, so dass es mit den Bedingungen in numerischen Simulationen zu chemisch angetriebenen Tröpfchen verglichen werden kann. In Kapitel 7 beschreibe ich ein unveröffentlichtes Projekt zu kontinuierlich angetriebenen Tröpfchen, in denen ich überraschende Nicht-Gleichgewichtsübergänge auf der Grundlage des Tröpfchendesigns der Kapitel 5 und 6 untersuche. Ich diskutiere die Bildung kugelförmiger Schalen aus Tröpfchen, die größenabhängig ist und für Tröpfchen nahe dem thermodynamischen Gleichgewicht nicht möglich ist. Diese Arbeit verdeutlicht, wie sich das Verhalten von intermolekularen Strukturen ändert, wenn ihre Eigenschaften mit Nicht-Gleichgewichtsprozessen gekoppelt werden.

Die in dieser Doktorarbeit vorgestellten Ergebnisse sind eines der ersten Beispiele für Koazervattröpfchen, die durch chemische Reaktionen reguliert werden, und das erste, das dies ohne die Notwendigkeit von Enzymen oder pH-Wertveränderungen zeigt. Dieses Tröpfchenmodell erfüllt somit einen wichtigen Aspekt, der zum Verständnis zellulärer Tröpfchen erforderlich ist, nämlich ihre Regulierung durch aktive Prozesse. Außerdem kann es als attraktives Modell für die Untersuchung potenzieller präbiotischer Kompartimente dienen, die primitive Formen eines Stoffwechsels beherbergen, bei denen chemische Energie umgewandelt wird.

List of abbreviations

|	
A	alanine
AMP	adenosine monophosphate
ATP	adenosine triphosphate
a.u.	arbitrary units
CSC	critical salt concentration
DIC	N,N'-diisopropylcarbodiimide
DIU	N,N'-diisopropylurea
D	aspartic acid
EDC	1-ethyl-3-(3-dimethylaminopropyl)carbodiimide
EDTA	ethylenediaminetetraacetic acid
et al.	et alii, and others
e.g.	exempli gratia, for example
FRAP	fluorescence recovery after photobleaching
FRET	Förster resonance energy transfer
F	phenylalanine
GDP	guanosine diphosphate
GFP	green fluorescent protein
GTP	guanosine triphosphate
G	glycine
HPLC	high-performance liquid chromatography
hr	hour
i.e.	id est, that is
K	lysine
L	leucine
LLPS	liquid-liquid phase separation
MLOs	membraneless organelles
mRNA	messenger ribonucleic acid
NMR	nuclear magnetic resonance
PDMS	polydimethylsiloxane
pSS	polystyrene sulfonate
rDNA	recombinant deoxyribonucleic acid
rRNA	ribosomal ribonucleic acid
R	arginine
RNA	ribonucleic acid
S	serine
UV	ultraviolet

Contents

Chapter 1

Liquid droplets as membrane-less compartments

During the last decade, experiments and theory discovered the importance of liquid droplets in organizing cellular processes. Moreover, they have also been proposed to be relevant as protocell models at the origin of life. In this chapter, I describe how cells use droplets to exert control over biochemical pathways and how the dysfunction of these mechanisms can lead to severe pathologies. I will also elaborate on the possible role of liquid droplets at the origin of life as a membrane-free compartment.

1.1 In today's cells

At the end of the 19$^{\text{th}}$ century, the biologists Wilson and Hardy viewed the cytoplasm as an emulsion.[1,2] However, the theory of polymer physics and advanced microscopic techniques such as electron and confocal microscopy were still lacking at the time. As a result, it was established only recently that the non-membrane-bound organelles in the cytosol of eukaryotes, such as centrosomes, nucleoli, or stress granules, are entities that can be described by the physics of liquid droplets (Figure 1.1).[3–5] Since then, it has become increasingly evident that cells use droplets to store and organize molecules, buffer noise, or influence signaling pathways, for example.[5–7] These membraneless organelles (MLOs), also referred to as biomolecular condensates, are composed of macromolecules such as proteins and RNA which diffuse rapidly within the droplet and into the surrounding cytosol. Strikingly, the concentration of the compartmentalized components can be orders of magnitude higher within MLOs than in the surrounding fluid. As a result, these droplets can exert control over biochemical pathways, *e.g.*, by either bringing components together or by selectively removing them from the cytosol.

Stress granules are an example of MLOs that form when a cell is under stress.[8–10] Specifically, stress factors such as heat or UV irradiation stall the initiation of translation, resulting in the accumulation of mRNA that condenses together with a variety of proteins via RNA-protein and protein-protein interactions into liquid-like droplets. These droplets dissolve again after the stress ceases, and the released mRNA can then be translated. Cells thus use stress granules as storage for mRNA when translation needs to be controlled due to environmental factors. Interestingly, stress granules are heterogeneous structures with core-shell architectures (Figure 1.2a-b).[9,11,12] These distinct domains within the droplet are not separated by a
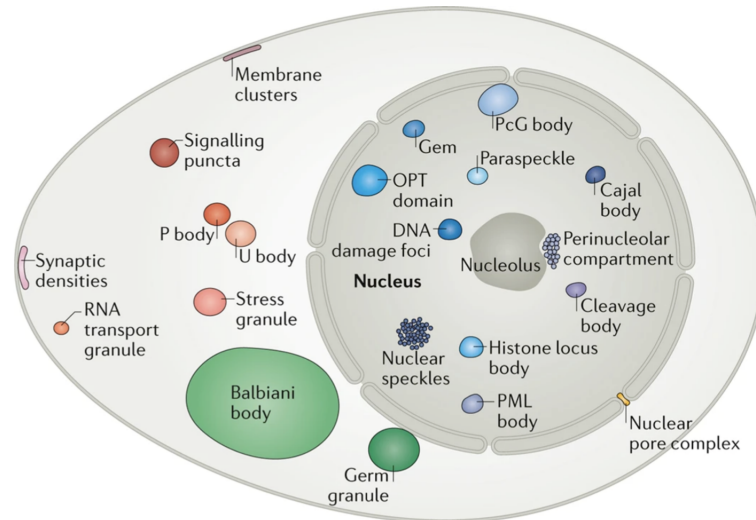
Figure 1.1: Liquid droplets in biology. Schematic representation of membraneless organelles in eukaryotic cells.[5] Some compartments occur only in specific cell types. Reprinted with permission from Springer Nature, Copyright © 2017.

membrane. In simple terms, one could view these assemblies as droplets within droplets, *i.e.*, multiphase droplets. Surface tension differences between the phases result in their formation and empower cells with further control over molecules and their related pathways spatiotemporally. In chapter 2.4, I will discuss the mechanism of multiphase formation in more detail.

The nucleolus is another MLO with multiple phases that comprises RNA and proteins.[13–15] Nucleoli are involved in ribosome biogenesis and thus play a fundamental role in cellular protein synthesis. Strikingly, the multiple stages of this process, *i.e.*, rDNA transcription, rRNA processing, and ribosome assembly, are spatially separated within the droplet (Figure 1.2c-d).[13] Each of the phases has a different set of components, *e.g.*, the fibrillar center (FC) is enriched in the RNA polymerase I whereas the granular component (GC) is enriched in the protein nucleophosmin. Although the nucleolus is not indispensable for the assembly of ribosome subunits, the presence of nucleoli across all eukaryotes suggests an evolutionary advantage.[16] All in all, cells use subcompartmentalized droplets to control complex and fundamental processes.

Compartmentalizing macromolecules into dense, liquid droplets also has its downsides. The droplet properties may change over time, resulting in the formation of solid aggregates which is referred to as maturation.[17–19] The components of these aggregates have stronger intermolecular interactions with one another, rendering these assemblies less dynamic than liquid droplets. As a result, matured MLOs may lose their function which is hypothesized to be the cause of diseases such as amyotrophic lateral sclerosis, frontotemporal dementia, Alzheimer's disease, and cancer.[17] Therefore, the cell must control the assembly and disassembly of MLOs, and their physical properties such as size, subcompartmentalization, or liquidity.

One way through which cells regulate MLOs is by chemical modifications of their constituents. Increasing evidence suggests that ATP-dependent processes such as acetylation, phosphorylation, or methylation modulate the properties of MLOs.[20–22] For example, the RNA helicase DDX3X is a stress granule component that, when acetylated at multiple lysine residues, leads to the formation of stress granules
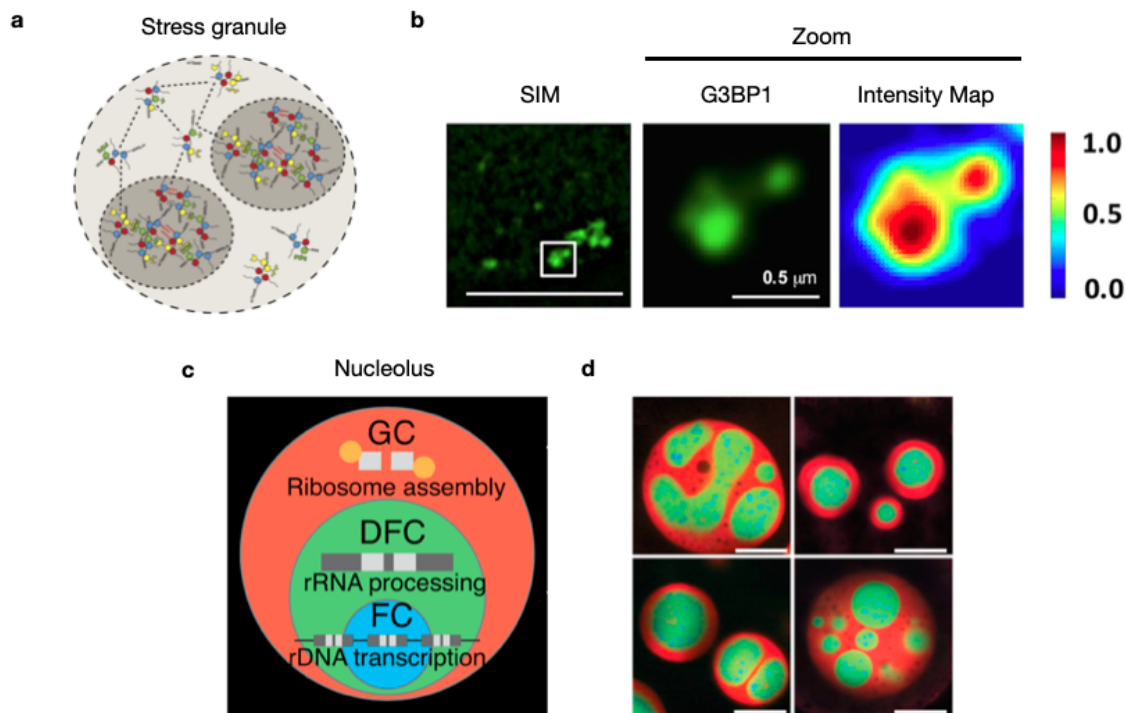
Figure 1.2: Multiple phases in cellular droplets. (a) Schematic representation of the core-shell architecture of a stress granule.[9] Reprinted and adapted with permission from Elsevier, Copyright © 2016. (b) Structured illumination micrographs (SIM) of stress granules after NaAsO$_2$ stress containing GFP-G3BP1.[12] The intensity map represents relative grayscale intensity. Unless stated otherwise, the scale bar is 5 μm. Reprinted and adapted with permission from Wheeler et al., Copyright © BY 4.0, 2016, https://creativecommons.org/licenses/by/4.0/. (c) Schematic representation of ribosome biogenesis in the nucleolus.[13] Three distinct regimes: FC (fibrillar center), DFC (dense fibrillar component) and GC (granular component). (d) Examples of nucleoli after coarsening in X. laevis nuclei treated with Lat-A.[13] GC is visualized with NPM1 (red), DFC with FIB1 (green), and FC with POLR1E (blue). Scale bar: 20 μm. (c-d) Reprinted and adapted with permission from Elsevier, Copyright © 2016.

with irregular size.[23] Phosphorylation of FMRP/CAPRIN1-based model MLOs can either induce or inhibit multiphase formation.[24] Finally, methylation of arginine residues can induce the formation of aggregates.[25] Post-translational modifications thus influence the properties of MLOs such as size, subcompartmentalization, and liquidity. Taken together, chemical reactions regulate MLOs and MLOs regulate chemical reactions reciprocally.

1.2 At the origin of life

In the previous section, I have outlined that today's cells use droplets for intracellular organization and processes. Remarkably, these droplets are evolutionarily conserved in eukaryotes[5] and prokaryotes[26]. In other words, the formation of liquid droplets seems to have brought advantages to organisms over the course of evolution.

In the 1920s, gel-like droplets were hypothesized to have been one of the first protocells on earth.[27–29] So-called coacervate droplets made from macromolecules could have up-concentrated biomolecules and facilitated prebiotic reaction pathways (Figure 1.3a).[30] The reasoning was that these droplets can be spontaneously formed and
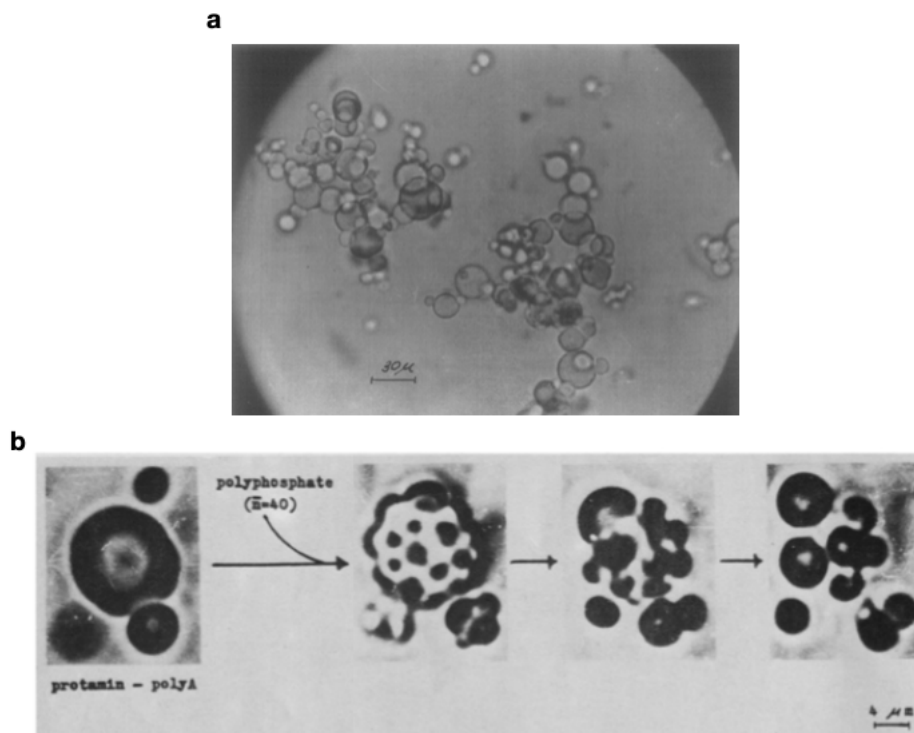
Figure 1.3: Synthetic aqueous droplets as protocell models. (a) Bright-field micrograph of coacervate droplets from polyphenoloxidase-histon-quinones.[30] Scale bar: 30 μm. Reprinted with permission from Elsevier, Copyright © 1971. (b) Micrograph series of coacervate droplets from protamine and poly(A) after the addition of polyphosphate.[33] Scale bar: 4 μm. Reprinted and adapted with permission from Elsevier, Copyright © 1980.

with their aqueous interior could have harbored primitive forms of metabolism.[31,32] Furthermore, they represent feasible reaction hubs due to their liquid-like nature which allows for fast diffusion of molecules within the droplet and across the droplet boundary. Indeed, coacervate droplets were shown to up-concentrate molecules, drive *in situ* enzymatic reactions and show life-like behavior such as droplet growth and division (Figure 1.3b).[33] However, the idea of coacervate droplets as a viable protocell model lost interest mid-20th century due to not being biologically relevant, the lack of a membrane, the need for large molecules for their assembly, and the emergence of liposome models as a competitive hypothesis.[34]

In the last decade, coacervate droplets have gained traction as a protocell model.[35–37] Firstly, it was found that these droplets can be made from small molecules such as ATP and oligolysines, rendering their assembly more prebiotically plausible.[38] Secondly, the discovery that today's organisms rely on liquid-like droplets made from macromolecules (see section 1.1) points to the importance of droplets as a (sub)compartment during the emergence of life. As a result, protocell models based on coacervate droplets were developed that enclose simple biochemical processes. For instance, a hammerhead ribozyme was compartmentalized into coacervate droplets composed of polylysine and a dextran derivative (Figure 1.4a).[39] The ribozyme cleaved a substrate with a FRET pair, resulting in a fluorescence increase upon product formation (Figure 1.4b). Strikingly, the RNA cleavage inside the droplets was occurring considerably faster than in the phase outside of the droplets (bulk). Localizing RNA into compartments is of general interest to the
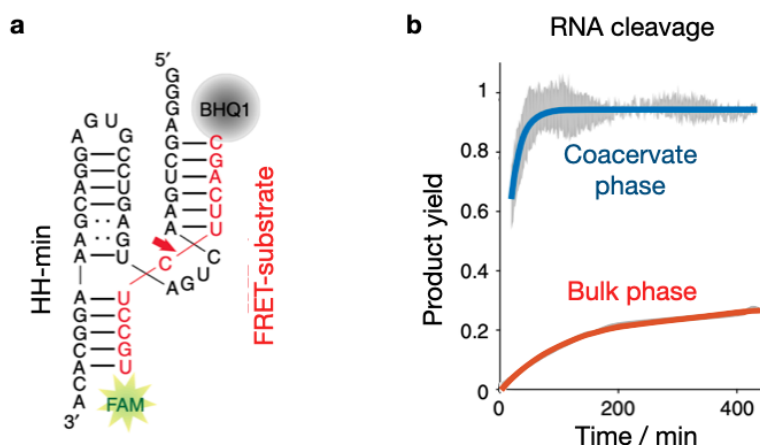
Figure 1.4: RNA catalysis in droplets as compartments. (a) Structure of hammerhead ribozyme (HH-min) and its RNA substrate.[39] The cleavage site is shown with a red arrow. (b) Cleavage of the substrate as a function of time inside the coacervate phase (blue) and the bulk phase (red).[39] Coacervate droplets are made from carboxymethyl dextran sodium salt and polylysine. (a-b) Reprinted with permission from Drobot et al., Copyright © BY 4.0, 2018, https://creativecommons.org/licenses/by/4.0/.

origin of life field because of the RNA's ability to store genetic information and catalyze its replication.[40] Other examples of enhanced biochemical reactions inside coacervate droplets include template-directed RNA polymerization[41], in vitro gene expression[42,43] and enzymatic reactions[44] which shows the droplets' capability as compartments that may facilitate metabolic pathways. All in all, membrane-free droplets show exciting properties that make them viable protocell models.

Open questions of the field

In recent years, the discovery of liquid droplets as a tool to organize molecules and biochemical reactions in the cytosol led to a better understanding of how today's cells regulate reaction cascades spatiotemporally. At the same time, a new interest in synthetic liquid droplets emerged both to model these droplets in our cells and to compartmentalize prebiotic chemistry at the origin of life. While phase-separated droplets represent a powerful framework to conceptualize the intracellular organization of molecules and biochemical processes, a clear understanding of how exactly cells regulate MLOs is still missing.[6,45,46] The reason for this uncertainty lies in part in the complex nature of these cellular droplets with hundreds of components going in and out of the droplet. As a result, the determination of the exact cellular function of an MLO *in vivo* is far from trivial. One of the ways to address these difficulties is by designing models with reduced complexity. These model systems may help us to understand the underlying concepts of cellular phase separation. More and more evidence suggests that post-translational modifications are a key mechanism of how cells exert control over the interactions between droplet components. Experimental and theory-based models are thus needed that are regulated by chemical reactions. This knowledge could be particularly useful in the future to understand the formation and prevention of protein aggregates that lead to age-related human diseases.

Outline of this thesis

In this thesis, I design liquid droplets as a simplified model for today and prebiotic cellular droplets. In the following two chapters, I first describe the necessary background for my experimental work. Specifically, I discuss in chapter 2 the physics of phase separation that is needed to understand how liquid droplets such as MLOs can form. Then, I focus on complex coacervation to build similar droplets synthetically. I show that complex coacervate droplets are promising experimental models because the interactions between their components are very similar to the ones found in cellular droplets. I describe how coacervate droplets can be designed and internally organized, and emphasize the role of chemical reactions in regulating their properties. In chapter 3, I discuss that chemically fueled droplets are powerful to understand how biology uses and regulates liquid droplets and how membrane-free compartments might have facilitated the emergence of life. I describe experimental and theory-based work on chemically fueled droplets that show exciting behavior vastly different from droplets close to equilibrium. In chapter 4, I discuss what aspects of the field are not yet covered by experimental models and outline the aims of this thesis. In chapter 5 and 6, I present my peer-reviewed experimental work based on chemically fueled coacervate droplets. In chapter 7, I discuss unpublished results from a project involving continuously fueled coacervate droplets. Finally, I conclude my thesis in chapter 8 and give a brief outlook on the future of the field.

Chapter 2

Complex coacervate droplets

Liquid droplet models are needed to understand better how MLOs function and how membrane-free compartments may have facilitated the emergence of life. In this chapter, I discuss the thermodynamic driving forces concerning liquid-liquid phase separation, *i.e.*, the formation of an emulsion full of liquid droplets. Then, I will outline how aqueous droplets can be built synthetically in water as a media, and what factors influence their properties. I conclude with how such droplets can be regulated and how they can be organized internally.
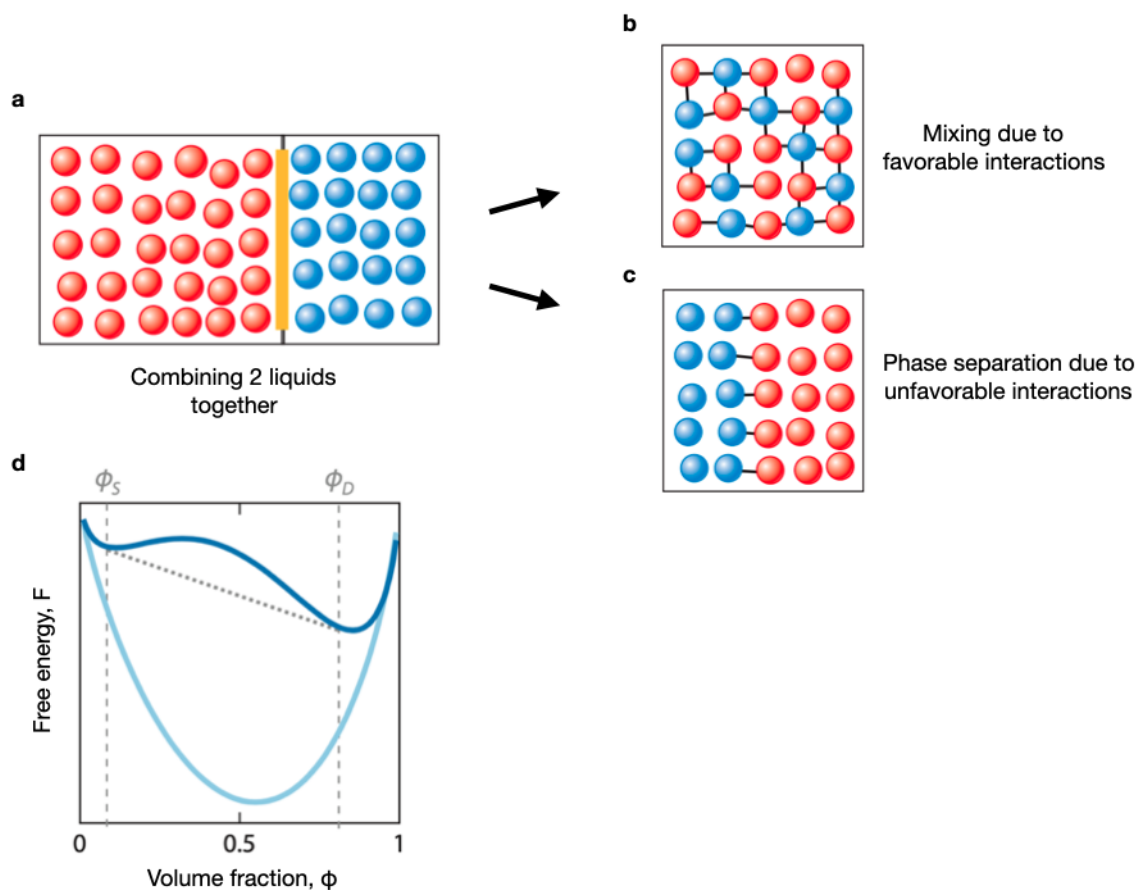
2.1 Physics of liquid-liquid phase separation

How can MLOs form and select specific molecules from the cytosol when water is the solvent in both phases? Why do the components of MLOs not just homogeneously mix within the cell? This behavior is particularly surprising considering that MLOs are liquid and not cross-linked aggregates. Simply put, the components of MLOs can easily rearrange unlike components inside more solid-like structures.

The two main factors that allow for coexisting liquid phases are the interaction energy E between the components within a phase and the mixing entropy S, following the equation for the free energy of mixing F

$$F = E - TS \tag{2.1}$$

where T is the temperature.[47] Let's consider a demixed state of two liquids where the individual components are separated from each other by a barrier (Figure 2.1a).[47] Without the barrier, components would homogeneously distribute, driven by the increase in the mixing entropy S (Figure 2.1b). However, the interaction energy E between the components can oppose the mixing entropy and disfavor certain orderings, *e.g.*, blue components prefer to be surrounded by blue neighbors instead of red ones. In these cases, the energetically most favorable ordering may be the demixed state (Figure 2.1c).[47] One way to depict this is by a phase diagram (Figure 2.1d). In the absence of intermolecular interactions, the free energy minimum is reached when both components are homogeneously mixed, *i.e.*, the volume fraction ϕ of the red molecules is 0.5 (light blue graph). When unfavorable interactions between the red and blue molecules are present, the system phase separates into two phases of volume fraction ϕ_S (more blue molecules) and ϕ_D (more red molecules) where the free energy is minimized (dark blue graph). A classical example of such a liquid-liquid

Figure 2.1: The physics of liquid-liquid phase separation. (a) Schematic representation of a demixed state with two types of molecules that are separated by a barrier.[47] (b) Lowest free energy configuration of (a) without the barrier in case of favorable molecular interactions between red and blue molecules.[47] (c) Lowest free energy configuration of (a) without the barrier in case of unfavorable interactions between red and blue molecules.[47] (d) The free energy F as a function of volume fraction ϕ of red molecules (volume fraction of blue molecules is $1 - \phi$) in the absence of molecular interactions (light blue graph) and the presence of unfavorable molecular interactions between red and blue molecules (dark blue graph).[47] Dashed lines depict the regime where demixing is energetically favorable. (a-d) Reprinted and adapted with permission from Annual Reviews, Inc., Copyright © 2014.

phase separation (LLPS) in everyday life is vinaigrette which is an unstable emulsion resulting in the separation of the oil molecules from vinegar.

This description of LLPS does also apply to complex fluids such as the cytosol with a plethora of different types of molecules.[47] Here, a subset of RNA and proteins phase-separates into droplets from their surroundings due to unfavorable interactions between the phase-separating components and the ones from the cytosol. Factors that contribute to the interaction energy of this phase separation process include electrostatic and supramolecular forces such as ion-pairing, cation-π interactions, π-π stacking, and hydrophobic interactions.[5,20,48] For this reason, proteins involved in LLPS show characteristic domains with heterogenous conformations, so-called intrinsically disordered regions (IDRs), that allow them to interact better with other macromolecules that phase-separate along them.[5,6] Moreover, these domains contain repetitive motifs that increase the proteins' multivalency which has a large contribution to the interaction energy and the resulting phase separation.[5] In other words, the longer a protein and the more IDRs it contains, the easier it will form

8

insoluble complexes with other macromolecules to phase separate into liquid droplets. While the concentration of these phase-separated molecules is high in the droplet phase (high volume fraction), it is considerably lower in the surrounding dilute phase (low volume fraction).

LLPS is thus a powerful tool for cells to compartmentalize and separate molecules on short time scales, thereby organizing the cellular contents and regulating metabolic pathways. In the context of the origin of life, protocells might have used the concept of LLPS to condense macromolecules of sufficient length into similar aqueous droplets. In the next chapter, I will show how such droplet models can be built synthetically.

2.2 Complex coacervation

Coacervation, a form of LLPS, describes the condensation of polymeric molecules into liquid, hydrated droplets.[37,49,50] These droplets do not have a fixed membrane, up-concentrate molecules, and their components diffuse rapidly within the droplet and across the droplet boundary. Coacervation can be subdivided into simple coacervation and complex coacervation (Figure 2.2a).[37,51] While the former is a form of segregative phase separation where one molecule is self-associating, the latter describes the complexation of oppositely charged polyelectrolytes leading to the formation of a dense droplet phase, *i.e.*, coacervate, and a dilute phase (Figure 2.2b-c).[52] While simple coacervates recently gained traction,[44,53–56] I will focus on complex coacervates for the rest of this chapter.

The formation of complex coacervate droplets is driven by enthalpic and entropic effects.[49,57] Specifically, changes in the enthalpy are caused by the ion-pairing of opposite charges whereas the entropy increases due to the release of water and counter ions when macromolecules partially complex each other. An early approach to assessing the mixing free energy from equation 2.1 for coacervates was the Voorn-Overbeek model which combined the Flory-Huggins theory[58] of mixing for polymer solutions with the Debye-Hückel theory[59] of dilute electrolytes.[36,50] The model was designed to assess the interactions between a polycation and a polyanion resulting in the equation for the mixing free energy F_{VO}:[60,61]

$$\frac{F_{\mathrm{VO}}}{V k_{\mathrm{B}} T} = \sum_i \frac{\phi_{\mathrm{i}}}{N_{\mathrm{i}}} \ln \phi_{\mathrm{i}} - \alpha \left[\sum_i \sigma_{\mathrm{i}} \phi_{\mathrm{i}} \right]^{3/2} + \frac{1}{2} \sum_{ij} \chi_{\mathrm{ij}} \phi_{\mathrm{i}} \phi_{\mathrm{j}} \qquad (2.2)$$

The first term on the right-hand side describes the mixing entropy for each species (including salt ions and the solvent).[36] The second term is the Debye-Hückel free energy which considers the attraction between a small, molecular charge and the average distribution of the surrounding oppositely-charged species. The last term captures the short-range interactions included in the Flory parameter χ.[36] This model is typically limited to polyelectrolytes that only interact weakly with each other.[49] Other models exist that capture better parameters such as the strength and size of the polyelectrolyte complexes.[62,63]

Coacervate droplets can be made from a plethora of building blocks, including synthetic polymers[49,65–69], polysaccharides[39,70,71], short and long peptides[72–75], nucleic acids[52,72,76–80], and from proteins in vitro[71,81–83]. As a result, coacervate-based materials were designed that show exciting morphologies beyond mere spherical droplets. These include coacervate-core micelles, coacervate-core vesicles, and hexag-
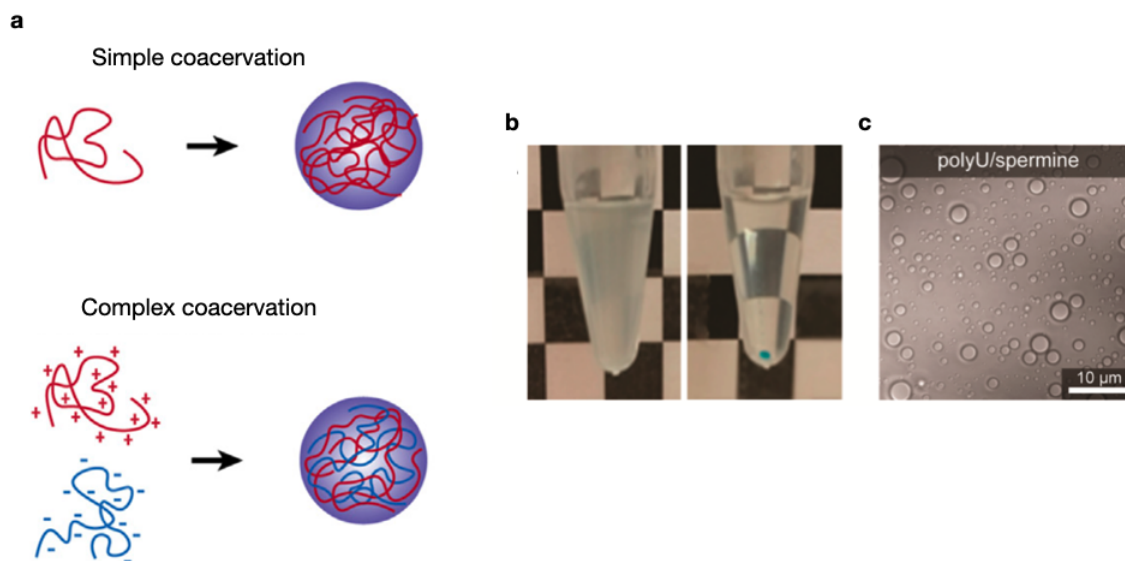
Figure 2.2: An overview over coacervation. (a) Schematic representation of simple and complex coacervation.[51] Reprinted and adapted with permission from Yewdall et al., Copyright ⓒⒸ BY 4.0, 2021, https://creativecommons.org/licenses/by/4.0/. (b) Photograph of a solution containing poly(uridylic acid) (polyU)/spermine complex coacervate droplets before (left) and after (right) centrifugation.[52] A dye-labeled RNA was added to aid in visualization. (c) Transmitted light differential interference contrast images of a solution from (b).[52] (b-c) Reprinted with permission from American Chemical Society, Copyright ⓒ 2016, https://pubs.acs.org/doi/10.1021/acs.langmuir.6b02499, refer to ACS for further permission.
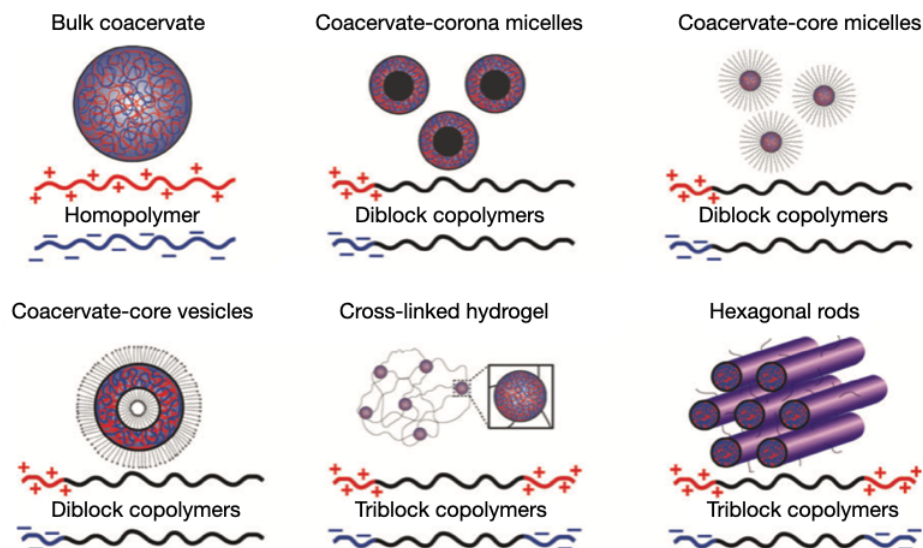
Figure 2.3: Morphologies of coacervate droplets. Architectural schemes of various hierarchically structured coacervate-based materials including bulk coacervates, coacervate-corona micelles, coacervate-core micelles, coacervate-core vesicles, and triblock copolymer coacervate hydrogels with spherical or hexagonal coacervate geometries.[64] Reprinted and adapted with permission from John Wiley and Sons, Copyright ⓒ 2016.

onal rods, for instance (Figure 2.3).[64,84] Their building blocks contain polymers that, apart from the electrostatic component, have hydrophobic motifs that have a low tendency to partition into the coacervate phase. One distinction between diblock and triblock copolymers is dependent on whether one or both ends of the polymer contain charged groups. In addition, the length of the hydrophobic tail influences the resulting assembly. For example, short alkyl chains form coacervate-core micelles, whereas longer alkyl chains yield corresponding vesicles.[85] Changing the morphology of coacervate droplets has the advantage that the size of the assemblies can be suppressed to a colloidal level, making them ideal candidates as drug carriers where hydrophilic drugs can be encapsulated in the coacervate core.[86]

In the next section, I discuss what factors tune the affinity of oppositely charged polyelectrolytes to each other which in turn influences the properties of coacervate droplets. I will also show how the affinity between the phase-separating molecules can be regulated by chemical reactions.
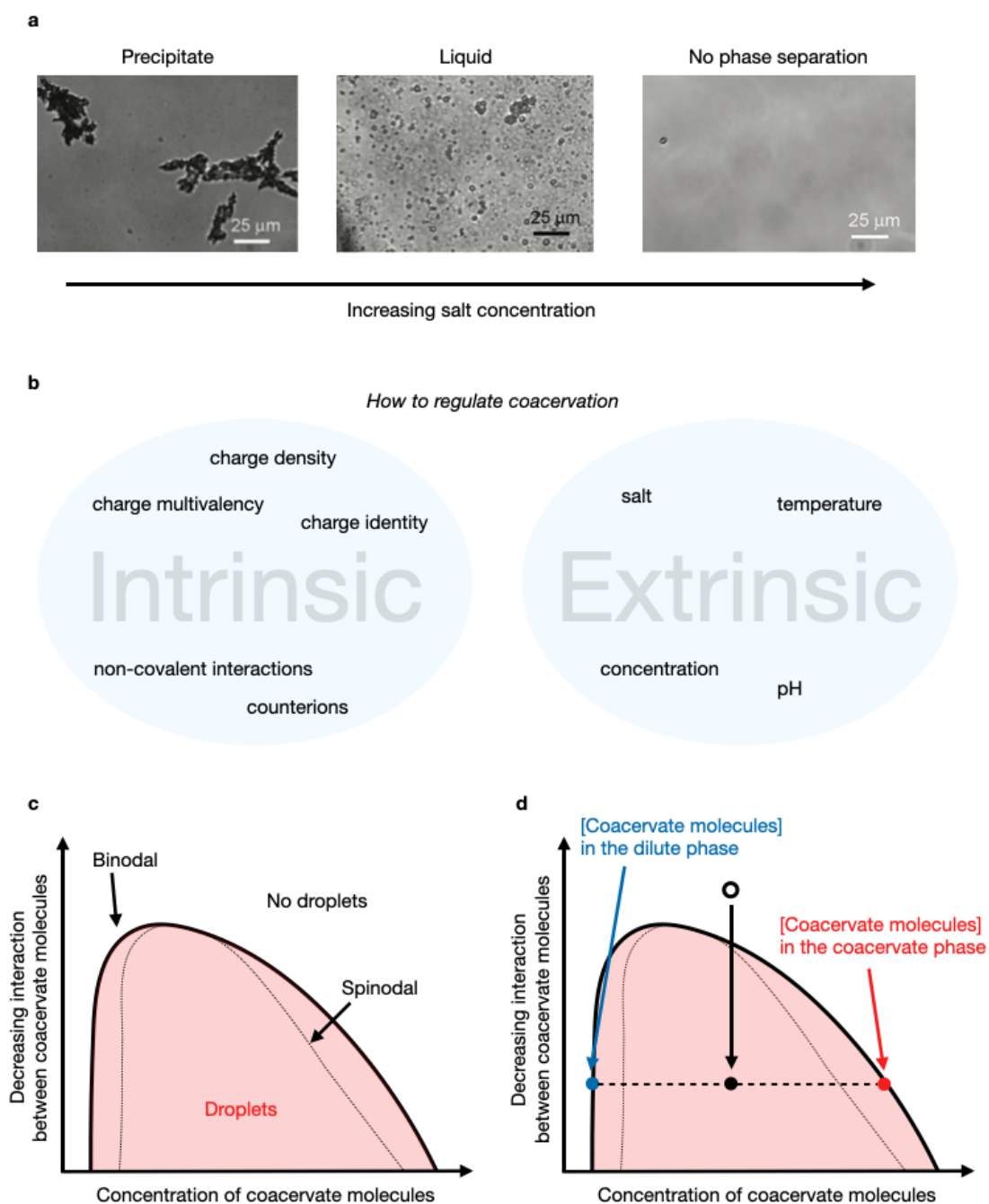
2.3 Regulation of coacervate droplets

Coacervation is used extensively in everyday life such as in food or cosmetics[87] because the material properties span from a liquid to gel-like state to precipitates dependent on the interaction strength of the polyelectrolyte complexes.[70] For example, coacervation between poly(allylamine hydrochloride) and poly(acrylic acid) led to precipitates at low salt concentration, whereas the addition of 400 mM NaCl resulted in the formation of droplets (Figure 2.4a).[67] Further increasing the salt concentration to 3 M eventually dissolved the droplets.

To regulate coacervate droplets and their properties it is crucial to modulate the binding between the droplet molecules (Figure 2.4b). Intrinsic factors are related to the molecular design of the droplet components, such as charge multivalency, charge density, the type of counterions, the nature of the charge, and non-covalent interactions.[49,88] For example, guanidinium cations from arginine residues interact more strongly with molecules than ammonium cations from lysines due to increased cation-π interactions.[89,90] Non-covalent interactions such as π-π stacking or the hydrophobic effect further contribute to the resulting interaction energy between coacervate molecules.[49,91,92] Extrinsic factors that regulate coacervate droplets include salt, pH, temperature, and the concentration of the polyelectrolytes.[64,93] For example, increasing the salt concentration in the solution will lead to a weakening and eventually disappearance of coacervation because the charge of the polymers is screened more effectively (see Figure 2.4a).[67] Also, the concentration of polyelectrolytes in solution and their ratio to each other is important, *i.e.*, coacervation is particularly favorable if negative and positive charges are balanced in solution.[94,95]

While the intrinsic factors determine the shape of the phase diagram, extrinsic factors set which conditions coacervate droplets are formed (Figure 2.4c). Here, parameters that change the interaction strength between the coacervate molecules, such as pH, temperature, or salt concentration, are plotted over the volume fraction of the coacervate molecules, *i.e.*, their concentration in the respective phases. The binodal line separates the regime where phase separation is expected (Figure 2.4c, red area) and where droplets are absent (white). The regime where phase separation is expected subdivides into a regime where droplet formation is possible but slow which is also referred to as the nucleation and growth regime (Figure 2.4c, in-

11

Figure 2.4: The material properties of coacervates and their regulation. (a) Optical micrographs of the coacervation of poly(allylamine hydrochloride) and poly(acrylic acid).[67] Increasing the sodium chloride concentration changes the phase-separated state from a precipitate to a liquid state, or a mixed solution, respectively. Reprinted and adapted with permission from American Chemical Society, Copyright © 2010. (b) Intrinsic and extrinsic factors that regulate complex coacervate droplets. (c) Phase diagram of complex coacervation. Droplets exist within the binodal line which is dependent on the interaction strength between coacervate molecules (y-axis). The area between the binodal and spinodal line depicts the nucleation and growth regime. The area below the spinodal depicts spontaneous nucleation, *i.e.*, spinodal decomposition. (d) Exemplary phase diagram of complex coacervation when the interaction strength between coacervate molecules is altered. No droplets are present when the interaction strength is sufficiently low (empty circle). When the interaction is increased, *e.g.*, when the temperature is decreased, droplets form (black disk). The equilibrium concentrations of the coacervate molecules in the dilute phase and within the droplets are obtained from a tie line (dotted line) that intersects the binodal. The resulting intersection points express the concentration of coacervate molecules in the dilute phase (blue disk) and inside the droplets (red disk).

between binodal and spinodal line).[49,50,96] Below the spinodal, droplets readily form via spontaneous nucleation, also referred to as spinodal decomposition.[50,96] Let's consider a case in the absence of droplets (Figure 2.4d, empty circle). When the interaction strength is increased, *e.g.*, by lowering the temperature, the new state is located within the binodal (black disk), and thus droplets form. The composition of the demixed phases, *i.e.*, the concentrations of the coacervate molecules in the dilute phase and within the coacervates, is determined by a tie line that intersects the binodal. In summary, coacervate droplets can be regulated by changing the respective extrinsic parameter leading to access to different regimes inside the phase diagram. Furthermore, the droplet properties and the resulting phase diagram can be tuned by molecular design.

Coacervate droplets share similarities with MLOs and serve as a model to understand better how MLOs work conceptually. As mentioned in section 1.1, MLOs are droplets that are maintained away from equilibrium by the continuous dissipation of chemical energy. Because of this reason, coacervate droplets were designed that are regulated by chemical reactions. Examples include reactions that activate or deactivate building blocks for phase separation by light-driven reactions[97–100], redox chemistry[55,101,102], changes in pH[38,86,103–107], enzymes[54,72,108–114], and others[115–117]. For example, coacervates were formed from poly(uridylic acid) (polyU) and a short peptide containing arginine and serine residues with the amino acid sequence RRASLRRASL (Figure 2.5a).[72] Using an enzyme pair that phosphorylates and dephosphorylates the serine residues, *i.e.*, protein kinase A (PKA) and lambda protein phosphatase (LPP), the affinity of the peptide towards the polyanion could be tuned (Figure 2.5b).[72] Specifically, when the peptide was in its phosphorylated state (RRApSLRRApSL), the solution was indicating the absence of droplets (Figure 2.5c, 0 min).[72] When LPP and its co-factor manganese were added, the peptide was dephosphorylated. In other words, the net positive charge of the peptide increased resulting in the formation of droplets (Figure 2.5c, 10 min). The peptide's phosphorylation state was reversed by the addition of PKA, ATP, and EDTA (Figure 2.5b). While the EDTA is needed to complex manganese and render phosphatase LPP inactive, re-phosphorylation of the peptide using kinase PKA and ATP results in the dissolution of the droplets again (Figure 2.5c, 40 min). This reversible cycle of droplet formation and decay can then be repeated by the sequential addition of manganese ions, ATP, and EDTA, respectively. Taken together, this example shows how the interactions between coacervate components can be transiently altered by chemical modifications which ultimately affects the droplets' stability. Chemical reactions are thus a powerful tool to regulate coacervate droplets.

In the next section, I discuss how subcompartments form within MLOs and how the internal hierarchy of coacervate droplets can be controlled.
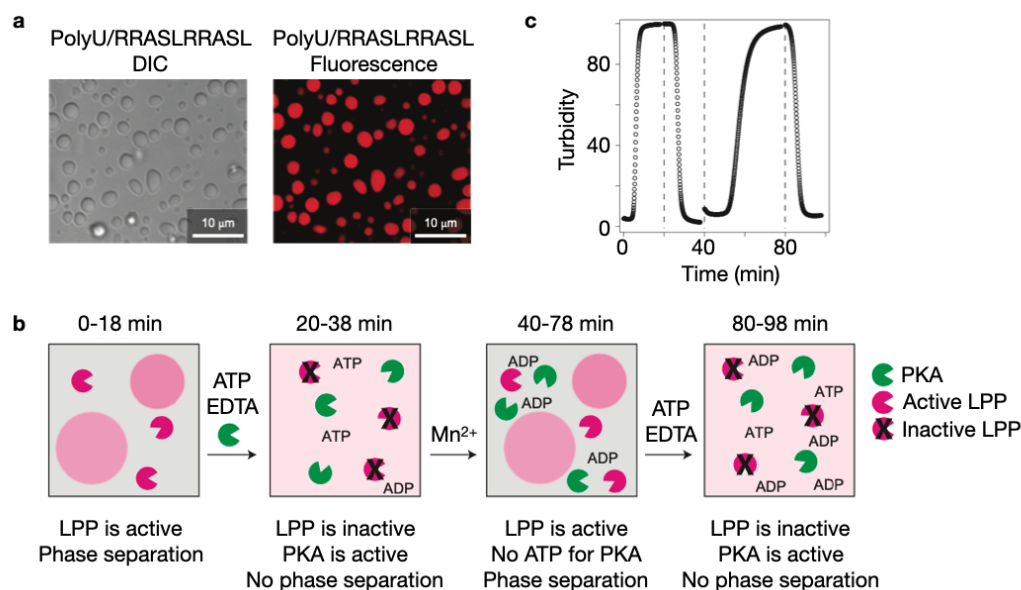
Figure 2.5: Reversible coacervation by enzyme-induced phosphorylation and dephosphorylation of a peptide. (a) Transmitted light differential interference contrast (DIC, left) and fluorescence (right) micrographs of polyU/RRASLRASL coacervate droplets.[72] Fluorescence from TAMRA-RRASLRASL. (b) Schematic illustration of the activities of an enzyme pair that phosphorylates and dephosphorylates a short peptide resulting in reversible coacervation.[72] At the start of the experiment, Lambda protein phosphatase (LPP) is active in the presence of manganese ions and dephosphorylates the peptide RRApSLRRApSL. Non-phosphorylated RRASLRRASL has a high affinity for polyU resulting in the formation of droplets. While the addition of EDTA complexes manganese which inactivates LPP, the addition of protein kinase A (PKA) and ATP results in re-phosphorylation of the peptide and droplet dissolution. Once the ATP is consumed, PKA becomes inactive. This reversible cycle of droplet formation can be repeated by the sequential addition of manganese ions, ATP, and EDTA, respectively. (c) Turbidity as a function of time of solutions from (b).[72] Droplets form when phosphatase (LPP) is active and dissolve when the kinase (PKA) is active. (a-c) Reprinted and adapted with permission from Springer Nature, Copyright © 2015.
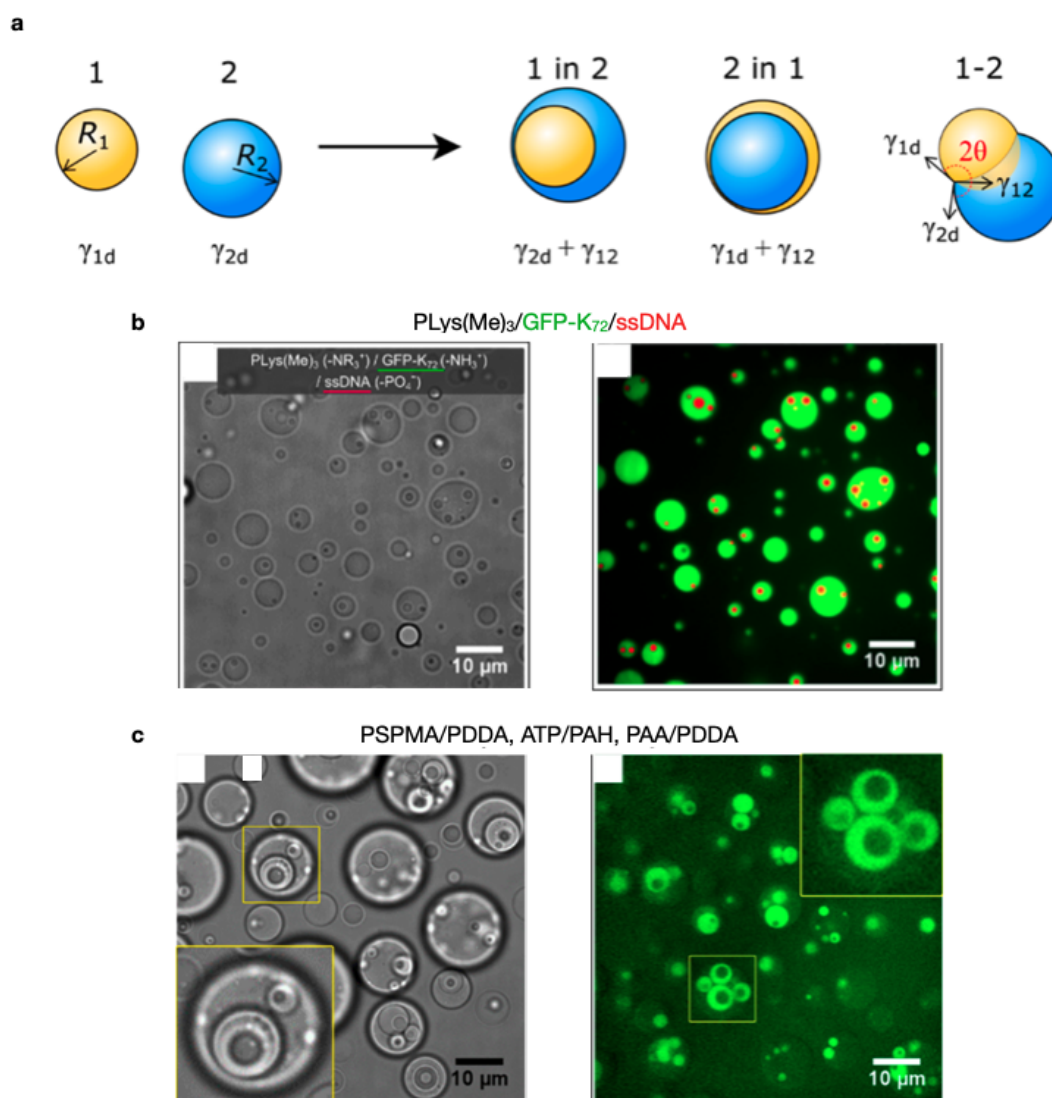
2.4 Multiphase coacervate droplets

In recent years, coacervate droplets have been reported that are internally organized. [77,90,107,118–125] As discussed in section 1.1, also the contents of MLOs are not always homogeneously distributed but may localize in distinct regimes within the droplet. The nucleoli proteins NPM1 and FIB1 can also form multiphase droplets *in vitro* (Figure 2.6a).[13] Two droplets can fuse but not mix when their surface tensions in water are sufficiently different (Figure 2.6b).[13] The droplet with the higher surface tension will prefer to be enclosed by the other droplet to avoid unfavorable interfacial energy with water. For example, if two oils with disparate surface tensions are mixed in water, *e.g.*, silicone and Crisco oil, they will form multiphase oil droplets where the oil with the higher surface tension (silicone) will be the inner compartment (Figure 2.6c).[13] To estimate the surface tension of both NPM1 and FIB1 droplets, the contact angle with hydrophilic and hydrophobic surfaces can be measured (Figure 2.6d).[13] A hydrophilic droplet with low surface tension in water has a lower contact angle on top of a hydrophilic surface than on top of a hydrophobic one. In other words, a droplet with low surface tension in water wets hydrophilic surfaces strongly whereas it can maintain its spherical shape on hydrophobic ones. Similarly, NPM1 droplets had a lower contact angle with a hydrophilic surface than with a hydrophobic one, indicating that NPM1 droplets have a low surface tension (Figure 2.6e-f, red).[13] In contrast, FIB1 droplets (green) showed the reversed behavior, indicating that FIB1 droplets have a considerably higher surface tension in water than NPM1 droplets (Figure 2.6e-f).[13] A high surface tension suggests that the water content in such droplets is low resulting in a decreased diffusivity of the molecules. Indeed, fluorescence recovery after photobleaching (FRAP) experiments showed that droplets of NPM1 are more liquid than FIB1 droplets.[13] In other words, the molecules move around quicker in NPM1 droplets than in the FIB1 droplets. As a result, the more hydrophobic FIB1 droplets settle into the NPM1 droplets. Taken together, multiphase MLOs can form when the respective droplet phases differ sufficiently in their surface tensions with water resulting in disparate liquid states where the inner phase is typically the more hydrophobic compartment.

Recently, this concept was extended and generalized for complex coacervate droplets.[119] Specifically, two liquid droplets of different compositions can either remain separated or fuse into three different multiphase rearrangements (Figure 2.7a).[119] If the interfacial energy between the surfaces of the two droplets 1 (yellow) and 2 (blue) is not too high, they will always fuse to minimize surface area and decrease the interfacial energy with the surrounding dilute phase. In other words, multiphase droplets will form if the surface tension between droplets (γ_{12}) is smaller than the respective droplets' surface tension with the dilute phase (γ_{1d} or γ_{2d}).[119] However, to obtain multiphase droplets, the fused droplets need to have disparate surface tensions to not just homogenously mix or display non-spherical shapes (Figure 2.7a). Similar to MLOs, the sum of all interfacial energies is lowest when the droplet that has the higher surface tension with water is the core of the multiphase droplet. Importantly, this only holds if the size of the droplets allows for it. If droplet 2 is larger and has a higher surface tension than droplet 1, then the most favorable ordering would be a multiphase droplet where droplet 1 is located at the core.[119] If droplet 1 were to grow, *e.g.*, by the addition of new droplet material, then the order would reverse so that droplet 2 would be the inner core.
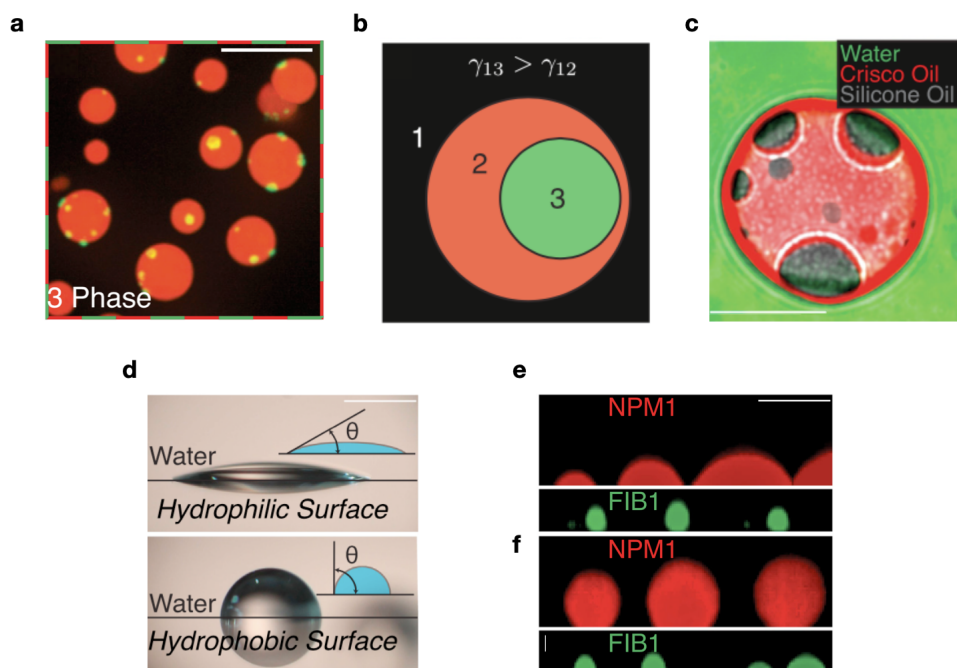
Figure 2.6: The mechanism behind multiphase formation in cellular droplets. (a) In vitro images of mixtures of purified nucleoli components NPM1 (red) and FIB1 (green).[13] Scale bar: 10 μm. (b) Schematic organization of three immiscible liquids resulting in multiphase droplets.[13] The more hydrophobic phase (green) has a higher surface tension with water (black) than the more hydrophilic phase (red) which has a lower surface tension with water. (c) Image of non-biological multiphase droplets: water (green), Crisco oil (red), and silicone oil (gray).[13] Scale bar: 20 μm. (d) A water droplet on a hydrophilic surface (top) and a hydrophobic surface (bottom).[13] Contact angles are shown schematically. Scale bar: 1 mm. (e) NPM1 droplets (red) and FIB1 droplets (green) on a hydrophilic surface (Pluronic-treated).[13] Scale bar: 5 μm. (f) NPM1 droplets (red) and FIB1 droplets (green) on a hydrophobic surface (Sigmacote-treated).[13] Scale bar: 5 μm. (a-f) Reprinted and adapted with permission from Elsevier, Copyright © 2016.
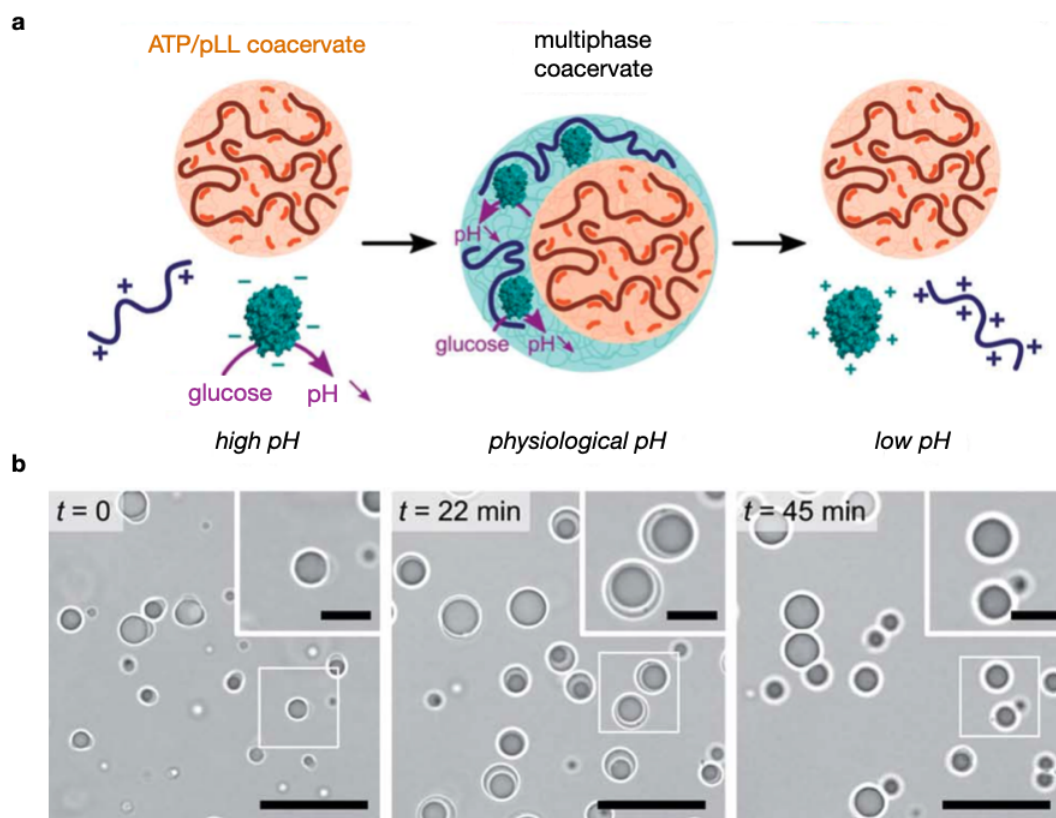
Figure 2.7: Multiphase formation in coacervate droplets. (a) Schematic illustration of four scenarios of two coexisting liquid droplets.[119] (b) Bright-field (left) and confocal fluorescence microscopy (right) micrographs of multiphase complex coacervate droplets formed from mixtures of polylysine and an oligolysine with single-stranded DNA.[119] Fluorescence from GFP-K_{72} (green) and Alexa-647 labeled ssDNA (red). The inner core mainly constitutes ssDNA and PLys(Me)$_3$ whereas the outer coacervate phase is made from ssDNA and GFP-K_{72}. Scale bar: 10 μm. (c) Bright-field (left) and confocal fluorescence microscopy (right) micrographs of multiphase complex coacervate droplets formed from mixtures of poly(3-sulfopropyl methacrylate) (PSPMA), poly(diallyl dimethylammonium chloride) (PDDA), ATP, poly(allylamine hydrochloride) (PAH) and poly(acrylic acid) (PAA).[119] Fluorescence from fluorescein-labeled PSPMA. The ATP/PAH inner core is surrounded by a PSPMA/PDDA shell in a PAA/PDDA outer coacervate phase. Note that bright-field and fluorescence do not show the same position. Scale bar: 10 μm. (a-c) Reprinted and adapted with permission from Lu et al., Copyright ⓒ BY 4.0, 2020, https://creativecommons.org/licenses/by/4.0/.

The multiphase formation can be predicted based on differences in the critical salt concentration (CSC).[119] The CSC is defined as the amount of salt needed to dissolve coacervate droplets. It is thus a measure of the stability of coacervate droplets where a higher CSC indicates stronger binding between the polyelectrolytes. Since the CSC is connected to the amount of water and the molecular density in a coacervate, one can make an indirect estimation of the droplets' surface tension.[68,119] For example, if droplet 1 (Figure 2.7a) has a higher CSC than droplet 2 then also the surface tension

17

of droplet 1 in water will be higher. Because the quantification of the droplets' CSC is typically easier than quantifying their surface tension, this approach facilitates the prediction of multiphase formation. Indeed, differences in the CSC successfully predicted the multiphase formation of coacervates droplets that are composed of methylated polylysine (CSC of 0.2 M) and an unmethylated oligolysine (0.11 M) with single-stranded DNA (Figure 2.7b).[119] Multiple phases inside one droplet are also possible if several coacervate pairs are present (2.7c).[119]

The multiphase formation is thus a powerful mechanism to organize the contents of a droplet without a membrane. These phases have disparate stabilities as indicated by their CSC which can be used to selectively dissolve phases, *e.g.*, by raising the salt concentration which destabilizes the more hydrophilic layer.[119] In line with that, pH changes can have a similar effect (Figure 2.8a).[107] Here, coacervates from ATP and polylysine were formed at high pH in the presence of a polysaccharide (DEAE-dextran) and glucose oxidase (GOx) in the dilute phase. With the addition of glucose, the pH decreased due to the formation of gluconic acid which led to partial protonation of GOx. As a result, coacervate droplets made from GOx as polyanion and DEAE-dextran as polycation were formed at a pH of around 7 where charge neutrality between the two polyelectrolytes was reached. These droplets then fused with the present ATP/pLL coacervates giving rise to multiphase droplets (Figure 2.8b).[107] Since gluconic acid was formed continuously, GOx eventually lost all of its negative charges leading to the disassembly of the outer layer of the multiphase droplets. Taking together, changes in pH can modulate the charge of a polyion giving rise to the temporal formation of multiphase coacervates.

Figure 2.8: pH-induced transient multiphase formation in coacervate droplets. (a) Schematic representation of Glucose oxidase-mediated (GOx) dynamic formation of multiphase coacervate droplets with an ATP/polylysine (pLL) core and a GOx/diethylaminoethyl-dextran (DEAE-dextran) shell.[107] At low glucose concentrations, stable multiphase droplets are formed as the pH stabilizes to physiological values while higher glucose turnover gives rise to a transient multiphase droplet organization. (b) Optical microscopy snapshots of ATP/pLL/GOx/DEAE-dextran mixtures produced at $pH = 10.2$ at different times after addition of $100\,\text{mM}$ glucose, showing the formation of transient multiphase coacervate droplets.[107] Scale bar: $20\,\mu\text{m}$. Insets show zoomed areas (white box). Scale bar: $5\,\mu\text{m}$. (a-b) Reprinted and adapted with permission from Karoui et al., Copyright © BY 3.0, 2021, https://creativecommons.org/licenses/by/3.0/.

Concluding remarks

Liquid droplets regulated by chemical reactions are crucial in organizing cellular processes. They could have been critical compartments at the origin of life, too. Increasing work shows how chemical reactions may regulate synthetic models such as coacervate droplets by the activation and deactivation of droplet building blocks. However, both reactions typically do not occur simultaneously in these studies. In the next chapter, I show what exciting properties emerge when droplet building blocks are chemically activated and deactivated at the same time. I discuss that these chemically fueled droplets are powerful to understand better how biology uses and regulates liquid droplets and to understand the possible role of droplets as prebiotic compartments that are regulated by simple forms of metabolism.

Chapter 3

Chemically fueled droplets as a liquid droplet model

The following chapter is based on a review article that I wrote for the journal *Trends in Chemistry*.[126]

I have outlined the necessity to build droplet models that are regulated by chemical reactions. In this chapter, I focus on a subset of such droplets, *i.e.*, chemically fueled droplets. I describe the prerequisites for their design and discuss exciting phenomena that emerge when the chemical reactions that regulate these droplets are localized into distinct phases.

3.1 Simultaneous activation and deactivation of droplet building blocks

In the previous chapters, I discussed that liquid compartments without a surrounding membrane control vital functions and chemistries in living cells. Chemical reactions can regulate these droplets' properties. As mentioned in section 2.3, numerous synthetic models were designed that are regulated by chemical reactions. However, the activation and deactivation of droplet building blocks typically do not take place simultaneously in these studies.

In this chapter, I chose to focus on droplet models where activation and deactivation are taking place at the same time, *i.e.*, chemically fueled droplets. Work by theoretical physicists and experimentalists is shedding light on the fundamentals of these chemically fueled droplets, allowing us to generalize some of their behaviors. I define *chemically fueled droplets* as droplets in which the phase separating molecules are regulated by a chemically fueled reaction cycle (Figure 3.1). This cycle comprises a minimum of two reactions: 1) an activation reaction that activates a building block for phase separation at the expense of chemical fuel, and 2) a deactivation reaction that reacts the activated building block back to the building block (Figure 3.1a). Thus, building blocks are temporarily activated for phase separation at the expense of the chemical fuel.[127] In the finite time the building blocks are active, they diffuse into a droplet. When deactivated, the building block molecule leaves the droplet again (Figure 3.1b). Consequently, chemically fueled droplets in a steady-state look like droplets close to equilibrium in that the concentrations of the activated building blocks are constant. However, the continuous activation and deactivation lead to
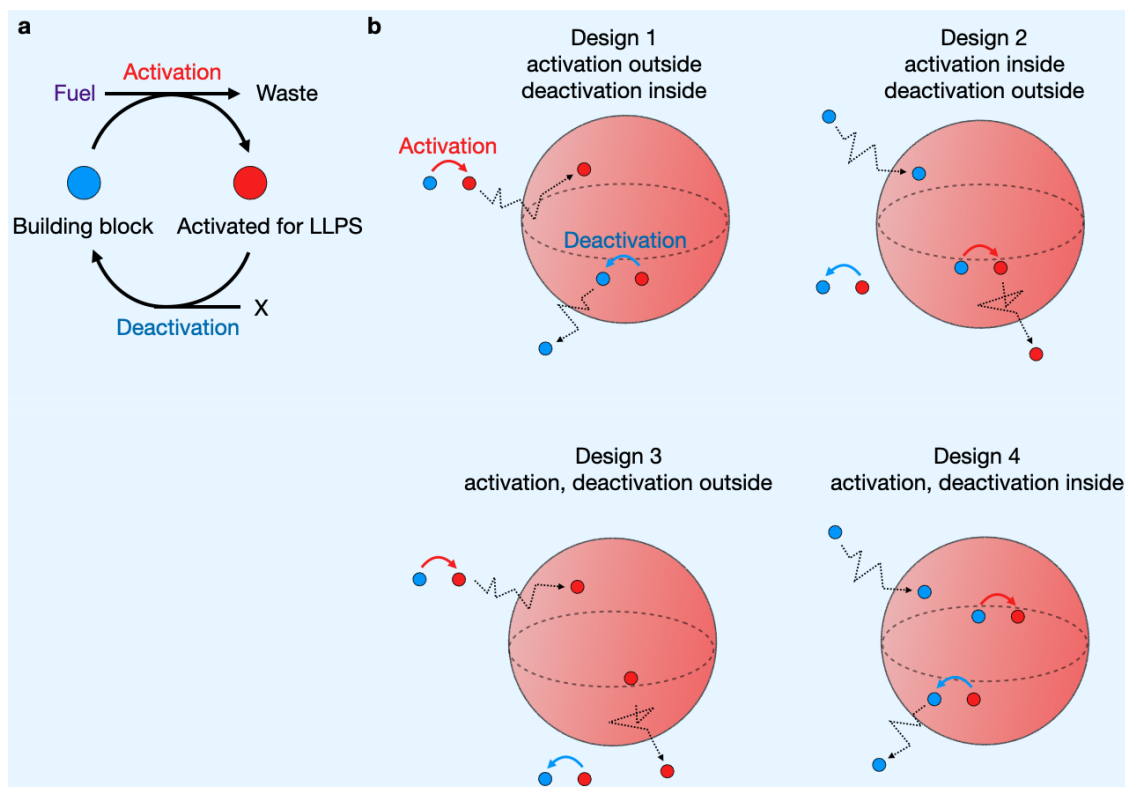
Figure 3.1: Design of chemically fueled droplets.[126] (a) A chemical reaction cycle that transiently activates a building block (blue disk) for LLPS at the expense of chemical fuel. The activated building block (red disk) can phase-separate in its finite lifetime until it is deactivated by a ubiquitous molecule X. (b) Four designs of chemically fueled droplets. Each droplet is regulated by chemically fueled activation and spontaneous deactivation simultaneously. The designs differ in where the droplets take place.

atypical fluxes over the droplet interface that gives rise to exciting, non-equilibrium behavior vastly different from droplets that are not regulated by chemical reactions. For example, it has been predicted that chemically fueled droplets can resist Ostwald ripening and evolve to a stable droplet size.[128–130] Under other conditions, these droplets can even self-divide.[131,132] Furthermore, another design shows that the ripening of these droplets can be accelerated by tuning the reaction rates.[133] Because these unique properties are regulated by rates of reactions and diffusion constants, they are not limited to one type of droplet. Indeed, the building blocks for chemically fueled droplets can be small molecules, peptides, or entire proteins. Chemically fueled droplets are non-equilibrium droplets and have also been referred to by others as *active droplets*. I prefer to reserve the term *chemically fueled droplets* as it sets them apart from other types of active matter, *e.g.*, self-propelled active droplets.[134,135]

Synthetic strategies towards chemically fueled droplets are reported based on oil- and coacervate-based droplets. Since coacervate droplets are considered a relevant protocell model at the origin of life (see section 1.2), more detailed studies of chemically fueled droplets offer not only insight into the fundamental behavior of the cell's phase-separated organelles but also prebiotic compartments.

I have established four possible designs of chemically fueled droplets depending on where activation and deactivation predominantly occur concerning the droplet (Figure 3.1b). Either the reactions are separated by the droplet boundary, *i.e.*, the activation occurs outside whereas deactivation occurs in the droplet (1), or activation

occurs in the droplet and deactivation outside (2). Alternatively, both reactions are localized outside the droplet (3), or both occur within the droplet (4). I have established here that each of these designs comes with unique properties. I will review these cases and illustrate what experimental and theoretical efforts have been made to understand such chemically fueled droplets.

## 3.2 Delocalizing activation and deactivation into separate phases

3.2.1 Design 1: deactivation inside of the droplets

I first discuss the design where droplet building blocks are activated outside the droplet and deactivated inside (Figure 3.2a). Such a design has the unique property that an activated building block must diffuse into a droplet before it can be deactivated. Similarly, a deactivated building block must leave the droplet before it can be reactivated. Thus, the droplet is endowed with influxes and effluxes that are regulated by the kinetics of the chemical reaction cycle. In such a design, one exciting property arises from the kinetics of the influx and efflux. That is, droplets all evolve to one preferred size that is dependent on the rate of deactivation. Simply put, the greater the droplet volume, the more activated building blocks it contains. Since the deactivation scales linearly with the number of activated building blocks, it will also scale linearly with the volume of the droplet. A molecule that is deactivated diffuses out of the droplet. As a result, the efflux of deactivated building blocks scales with the volume of the droplet. In contrast, the influx of activated droplet building blocks scales with its surface area. Simply put, a molecule is activated outside the dilute phase, after which it diffuses until it enters a droplet. The greater the droplet surface area, the greater the chance this activated building block hits it.

Because of the surface-area-dependent influx and volume-dependent efflux, all droplets evolve to one optimal size.[128,130] Droplets smaller than this optimal size will grow. In contrast, droplets larger than this size will shrink. Droplets in an emulsion close to equilibrium differ vastly from such chemically fueled droplets.[130] The undesirable interfacial energy between the droplets and their surrounding media means that an emulsion close to equilibrium aims to decrease its surface area, a process that is called coarsening. To coarsen, droplets can either fuse or undergo Ostwald ripening. Ostwald ripening is a process driven by Laplace pressure differences between droplets.[130] Specifically, the Laplace pressure of tiny droplets is higher compared to larger droplets. This pressure difference leads to a concentration gradient of droplet molecules from smaller to larger droplets, ultimately resulting in larger droplets growing at the expense of smaller ones. Therefore, coarsening results in a continuous increase in the droplet radius, which can be calculated as demonstrated in Figure 3.2b.[130] Here, the growth rate, i.e., the change in the droplet size over time, is dependent on the size of the droplet. In passive droplets close to equilibrium (Figure 3.2b, blue trace), tiny droplets above a nucleation threshold grow quickly, whereas droplets below this value are not stable and dissolve. Very big droplets grow continuously, dependent on the system size.

In contrast, droplets of design 1 (Figure 3.2b, orange trace) can suppress Ostwald ripening to favor multiple droplets around the critical volume.[128] Indeed, calculations
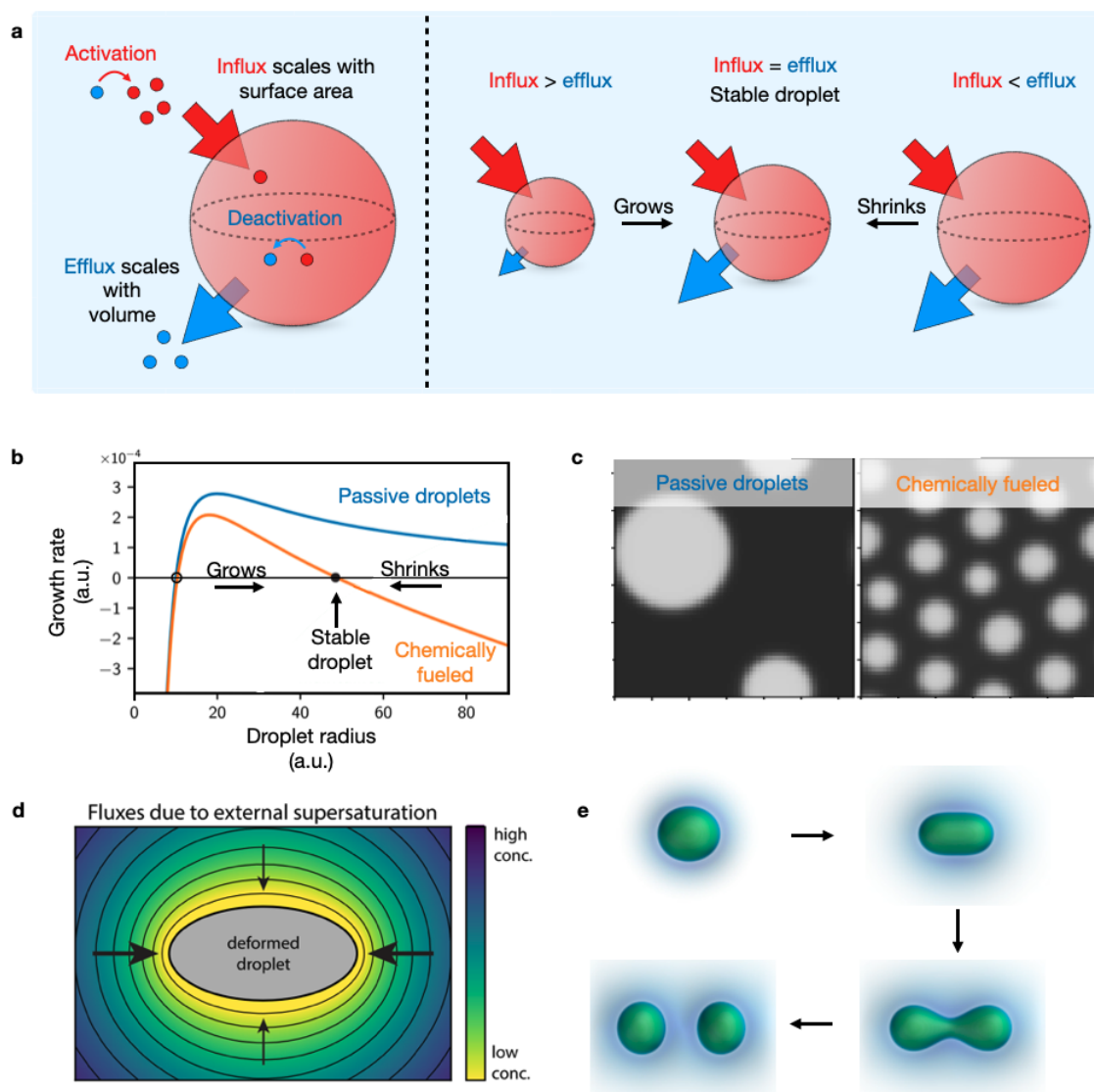
Figure 3.2: Theoretical simulations of droplets following design 1.[126] (a) Schematic representation of a chemically fueled droplet where activated building block (red disk) is deactivated (blue disk) inside and reactivated outside the droplet. The balance between influx (red arrow) and efflux (blue arrow) regulates whether a droplet grows or shrinks. (b) The growth rate of passive (blue) and chemically fueled droplets (orange) as a function of the droplet size.[130] Stationary states are shown for stable (filled circle) and unstable (empty) states. Reprinted and adapted with permission from IOP Publishing, Ltd, Copyright © 2019. (c) Numerical simulations of passive (left) and chemically fueled (right) droplets by design 1.[136] Reprinted and adapted with permission from Elsevier, Copyright © 2022. (d) Chemical fluxes in a deformed chemically fueled droplet.[130] Reprinted and adapted with permission from IOP Publishing, Ltd, Copyright © 2019. (e) Simulation of the self-division of a chemically fueled droplet.[131] Reprinted with permission from Springer Nature, Copyright © 2017.

show that droplets below the stationary size grow (Figure 3.2b), whereas droplets bigger than the stationary size have a negative growth rate and shrink (Figure 3.2b). This unique property was demonstrated in a simulation depicted in Figure 3.2c.[136] Close to equilibrium, passive droplets ripen into a few large droplets through Ostwald ripening. In contrast, multiple chemically fueled droplets of design 1 coexist and grow towards an optimal volume at a steady state. While droplets not regulated by chemical reactions typically maintain a spherical shape due to surface tension effects, diffusive fluxes in a chemically fueled droplet with a very large stationary size can deform the droplet once a critical size is reached.[137] Since the influx of new activated building blocks scales with the surface area and is more favorable at a high mean curvature, shape instabilities lead to the continuous elongation of a deformed droplet (Figure 3.2d).[130] Conversely, the efflux of deactivated droplet building blocks outcompetes the influx in the middle part of the droplet due to a lower mean curvature. These imbalances in the diffusive fluxes result in separating the large, deformed droplet into two smaller droplets of spherical shape (Figure 3.2e).[131,132] This self-division process can repeat itself via regrowth of the newly formed droplets until the supersaturation is sufficiently depleted.[130] This finding is remarkable given the simplicity of the droplet system and serves as an inspiring example of how chemical reactions can alter droplet behavior.

Two reported droplet systems are conceptually similar to design 1, i.e., droplet building blocks are activated outside and deactivated within the droplet. Fanalista et al. designed complex coacervate droplets that form when guanosine triphosphate (GTP) and polylysine are mixed in a PDMS-based microchamber (Figure 3.3a).[78] When the authors added FtsZ, a tubulin homolog in bacteria that uses GTP to assemble into filaments,[138] it preferentially localized on the coacervates' surface. Since FtsZ catalyzes GTP hydrolysis to GDP, it catalyzes the deactivation. Indeed, the droplets were unstable in the presence of FtsZ and shrunk in tens of minutes (Figure 3.3b).[78] The total consumption of GTP did not entirely dissolve the droplets but left behind aggregates hypothesized to comprise FtsZ, GDP, and polylysine. Next, the authors supplied GTP from the dilute phase by flushing fresh GTP through the microchamber. In other words, new droplet building blocks were supplied from the outside and deactivated inside the droplets. Indeed, droplets could be stabilized, resulting in stable droplet sizes for more than an hour (Figure 3.3c).[78] Even though the droplets most probably remained polydisperse, this example shows that droplets regulated by spatial fluxes and chemical reactions can stabilize if the droplet boundary's chemical fluxes are balanced. Finally, the authors show that coupling the deactivation of building blocks to the formation of filaments on the droplets' surface may lead to morphological transitions, e.g., when the droplets are exposed to mechanical stress (Figure 3.3d).[78]

In this thesis (see chapter 5), I also introduce a droplet system following design 1 (Figure 3.4a).[139] I used a chemical reaction cycle that converts a C-terminal aspartic acid into its anhydride state by consuming a carbodiimide-based fuel (fuel-driven activation). That anhydride hydrolyzes back to aspartic acid spontaneously (deactivation). When designed in an arginine-containing peptide, the building block has a low affinity for RNA. However, upon fuel-driven activation, the peptide loses its two negative charges, which increases its affinity for RNA (Figure 3.4a-b). The activated building block can bind RNA, which induces coacervate droplet formation. Because the deactivated building block has a poor affinity for RNA, it primarily resides outside
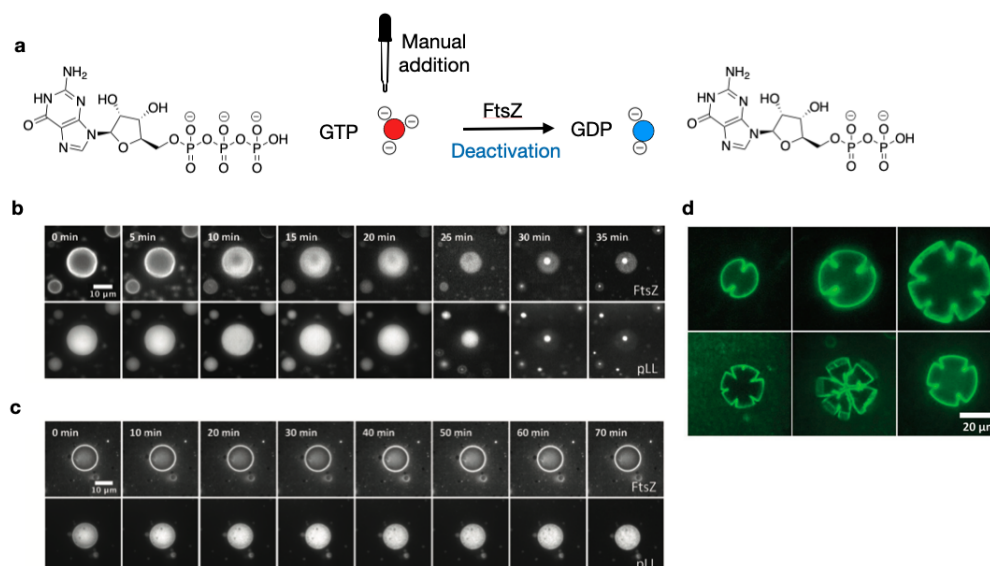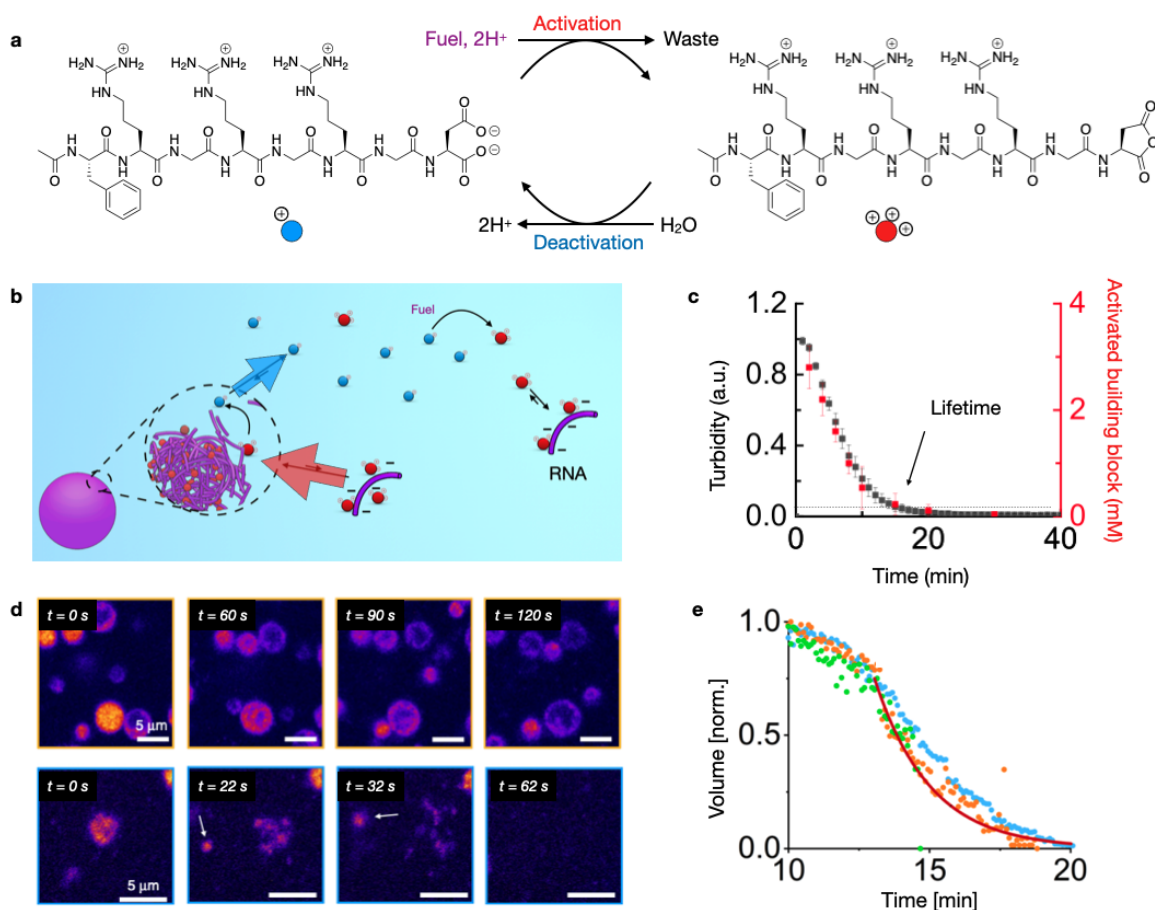
Figure 3.3: GTP-fueled droplets following design 1.[126] (a) Deactivation of GTP to GDP by the addition of FtsZ results in the deactivation of coacervate building blocks.[78] (b-c) Microscopic images of the droplet evolution with no (b) or continuous (c) supply of GTP from the outside.[78] (d) Shape deformations of droplets from (a) under mechanical stress.[78] (b-d) Reprinted and adapted with permission from John Wiley Sons, Copyright © 2018.

of the droplets. Thus, the activation occurs mostly outside. Because of the activated building block's high affinity for RNA, it primarily resides inside the droplets, and deactivation mainly occurs within the droplets (Figure 3.4b). Consequently, the droplet is regulated by the kinetics of the reaction cycle and the amount of fuel added. Indeed, in response to fuel, the evolution of the droplets was tightly regulated by the reaction cycle. The turbidity of the sample, which is a measure of the presence of droplets, evolved similarly to the concentration of the activated building block (Figure 3.4c).[139] The chemically fueled droplets rapidly grew via fusion and decayed after 20 min because all fuel had been consumed. During this decay process, these dynamic droplets showed unexpected behavior that included vacuolization and irregular droplet division into tiny droplet fragments (Figure 3.4d).[139] I hypothesized that, as the deactivation was out-competing the activation towards the end of the reaction cycle, the increase in unfavorable interactions inside the droplet would lead to the efflux of molecules and droplet disassembly. A follow-up study from the Boekhoven group demonstrated that when polystyrene sulfonate was used as a polyanion instead of RNA, these droplets did not self-divide.[140,141] Instead, they tended to shrink as the system ran out of chemical fuel. Excitingly, the droplet's dissolution kinetics matched the deactivation kinetics accurately, further demonstrating that the droplet properties are regulated through the kinetics of the reaction cycle (Figure 3.4e).[140] In all these experiments, the droplets are fueled with a batch of chemical fuel and thus never reach a steady state as in the theoretical simulations. Therefore, to find size-control behavior based on design 1, these droplets should be kept in a steady state.

Figure 3.4: Carbodiimide-fueled droplets following design 1.[126] (a) A chemical reaction cycle that converts a chemical fuel (EDC) into waste (EDU) while transiently removing two negative charges on a building block.[139] (b) Schematic representation of complex coacervate droplets composed of RNA and a chemically fueled peptide following design 1. (c) Turbidity (black) and concentration of activated building block (red) as a function of time when 25 mM fuel is added as a batch.[139] (d) Microscopic images of the fusion, vacuole formation, and fragmentation of droplets when fuel is scarce.[139] (e) Normalized droplet volume of three droplets with different sizes as a function of time.[140] The red line represents a fit using the deactivation rate constant of the activated building block. (c-d) Reprinted and adapted with permission from Donau et al., Copyright ⓒ BY 4.0, 2020, https://creativecommons.org/licenses/by/4.0/. (e) Reprinted and adapted with permission from Bergmann et al., Copyright ⓒ BY 4.0, 2020, https://creativecommons.org/licenses/by/4.0/.

3.2.2 Design 2: deactivation outside of the droplets

In design 2, the activation occurs within the droplet, whereas deactivation is predominantly outside (Figure 3.5a). A theory-based study on such a design describes an autocatalytic droplet catalyzing the activation of its building blocks.[128,142] The activation is therefore volume-dependent, i.e., a big droplet synthesizes more building blocks than a small one. The influx of building blocks is coupled to the activation reaction, i.e., when a building block is activated, the droplet can partition a new, not yet activated building block. As a result, also the influx of building blocks into the droplet is volume-dependent. In contrast, the efflux of activated building blocks into the dilute phase depends on the droplet's surface area. On the one hand, big droplets with a small surface area to volume ratio will grow faster than small ones. On the other hand, tiny droplets will shrink due to a high surface area-to-volume ratio. Thus, tiny droplets will dissolve, and large droplets will grow. This behavior is reminiscent of Ostwald ripening but occurs faster than in droplets that are not regulated by chemical reactions.[128,142] In other words, the fuel-driven chemical reaction cycle can accelerate droplet ripening.

While these autocatalytic droplets can grow exponentially once they cross a critical radius, their nucleation is inherently difficult, considering the activated building blocks are not produced without droplets.[128] A method to decrease this nucleation barrier is by incorporating an active core that catalyzes the activation, e.g., by the localization of an enzyme (Figure 3.5b). Here, the activation of building blocks via a catalytic activity Q is dependent on the core's relative volume and far less on the size of the droplet, in contrast to purely autocatalytic droplets. Therefore, the limiting factor for droplet growth is the influx of deactivated building blocks which favors the growth of smaller droplets and the shrinkage of larger ones. Similar to design 1, stable droplet size is obtained when influxes and effluxes are matched, leading to suppressed Ostwald ripening and multiple droplets coexisting at a stationary size.[128,130,142] Interestingly, droplets of unequal sizes can coexist if they possess disparate catalytic activities in the active core.[128] Furthermore, activation and deactivation in such autocatalytic droplets can regulate the positioning of particles within the droplet.[143] The growth rates of such autocatalytic droplets are depicted in Figure 3.5c.[128] An autocatalytic droplet will grow until the system size is reached (blue trace). In contrast, an autocatalytic droplet with an active core (green trace) has a shallow nucleation barrier, and therefore, small droplets grow considerably faster than droplets without an active core. These droplets then grow until the system size is reached as well. In an infinite system (orange trace), autocatalytic droplets behave like passive droplets (see Figure 3.2b). An example of how active cores can regulate droplet growth comes from centrosomes,[144] which are liquid-like droplets in the cell nucleus and which are crucial for the positioning of the mitotic spindle during cell division (Figure 3.5d-e).[145]

It is thus vitally important for the cell to control the centrosome's number and size, which can be accomplished by autocatalytic droplets with an active core. While the activation of building blocks inside the droplets leads to the experimentally observed sigmoidal growth behavior (Figure 3.5d), i.e., the exponential growth plateaus, the number of active cores in the cell regulates how many centrosomes are formed (Figure 3.5e).[142]
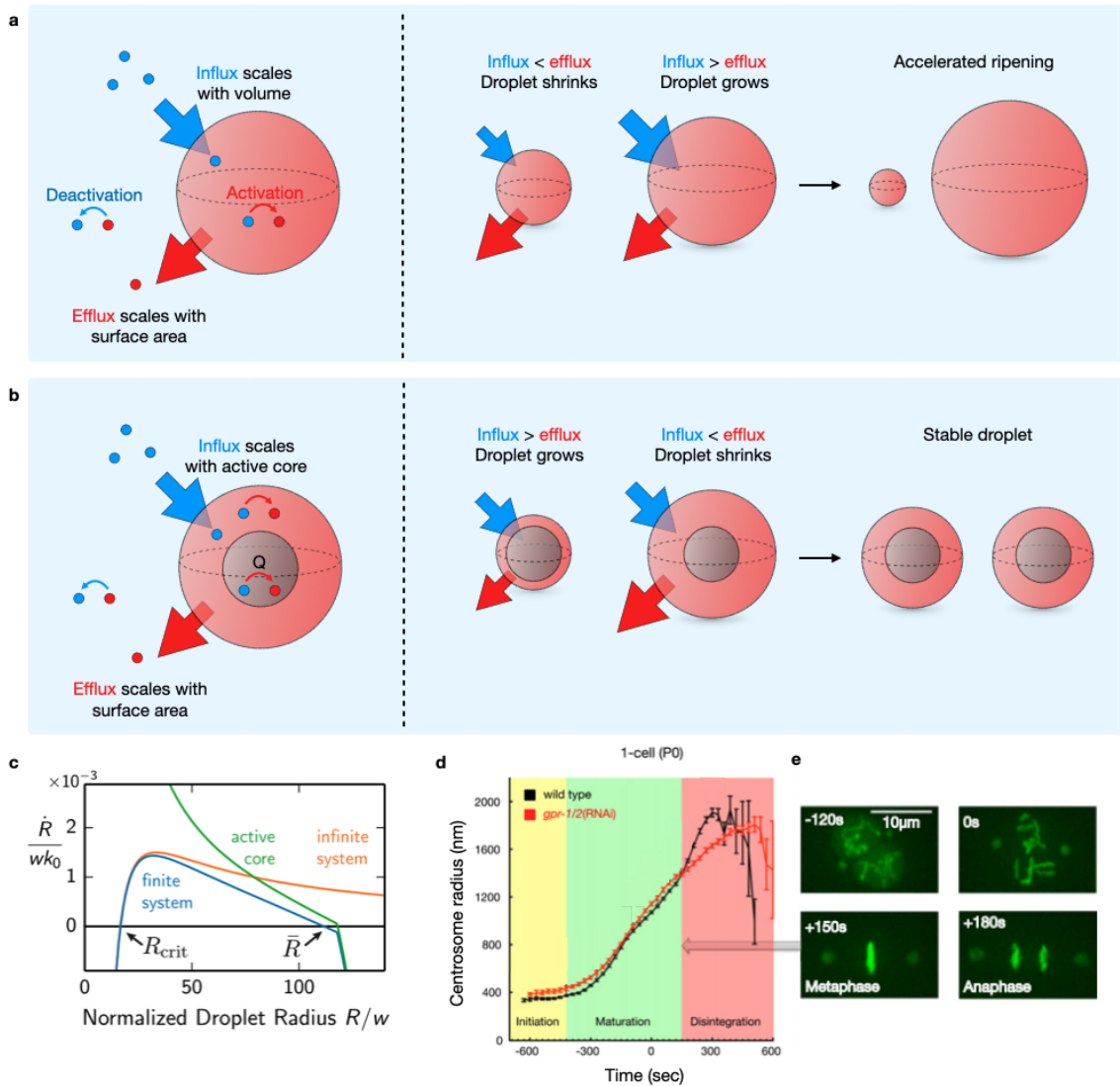
Figure 3.5: Chemically fueled droplets whose building blocks are being activated inside and deactivated outside following design 2.[126] (a) Schematic representation of an autocatalytic droplet where an activated building block catalyzes its formation in the droplet, whereas deactivation occurs outside.[128,142] The size of a droplet is decisive for droplet shrinkage or growth, ultimately resulting in accelerated Ostwald ripening. (b) The autocatalytic droplet from (a) contains an active core with a catalytic activity Q.[128,142] The core's relative size is decisive for droplet shrinkage and growth, ultimately resulting in droplets coexisting at a stable size. (c) The growth rate as a function of the droplet size.[128] Profiles of autocatalytic droplets in a finite (blue) and infinite (orange) system as well as autocatalytic droplets with an active core in a finite system (green) are shown. Reprinted and adapted with permission from Elsevier, Copyright © 2015. (d) Centrosome radius over time from an average of 20 wild-types and 7 gpr-1/2(RNAi) embryos.[144] Error bars are the standard error of the mean. (e) Image sequence of embryos expressing both g-tubulin::GFP and histone::GFP, illustrating the formation of the centrosomes and mitotic spindle.[144] (d-e) Reprinted and adapted with permission from Elsevier, Copyright © 2011.

## 3.3 Localizing activation and deactivation into the same phase

3.3.1 Design 3: both reactions outside of the droplets

In this design, activation and deactivation occur outside of the droplets. The Boekhoven group demonstrated this design using the carbodiimide fuel-driven reaction cycle that transiently activates an anionic diacid into an uncharged anhydride. When the building block has a hydrophobic tail, i.e., a chain of six to ten carbons, it is soluble, yet it phase separates into oil droplets upon activation (Figure 3.6a).[148] Since the fuel, deactivated building block, and water are excluded from the oil phase, activation and deactivation occur in the dilute phase. An attractive unique property emerges from this design. Because the deactivation occurs outside of the droplets, the droplets are essentially "protecting" their activated building blocks from the deactivation.[146] As a result, the deactivation only occurs on the fraction of activated building blocks that are present in the solution, which is equal to their solubility. Therefore, the deactivation rate equals the deactivation rate constant multiplied by the solubility. Because both factors are constant, the deactivation rate is also constant, i.e., zero-order deactivation. Moreover, the rate decreases with decreasing solubility of the activated building blocks.

When the levels of these activated building blocks decay over time when a finite amount of fuel is added, their decay profiles differ from each other. Indeed, when the activated building blocks cannot phase-separate, they decay with pseudo-first-order kinetics which is the case for C6-succinic anhydride (Figure 3.6b, green trace).[147] In contrast, for the droplet-forming C8-succinic anhydride (red), the deactivation kinetics follow a zero-order reaction, i.e., the activated building blocks deactivate with linear kinetics after all fuel is depleted. Moreover, the zero-order rate of deactivation scales with the solubility of the activated building block. In other words, the poorly soluble C10-succinic anhydride deactivates drastically slower than C8-succinic anhydride. Excitingly, this self-protection mechanism can be applied as transient emulsions that deliver hydrophobic drugs with linear decay kinetics.[147] Also, this feedback mechanism provides access to parasitic behavior in which molecules that partition into the droplets benefit from the protective environment.[149]

Another consequence of this design is that Ostwald ripening can be accelerated. The authors observed this behavior when they maintained these anhydride-based oil droplets in a steady state by continuously pipetting in chemical fuel. For example, when C8-succinic acid droplets were actively maintained with a constant flux of $60\,\mu m/min$ fuel, the droplets coarsened into a few large droplets within two hours without any evidence of droplet fusion (Figure 3.6c).[133] This ripening behavior is faster than the Ostwald ripening of passive droplets with similar interfacial surface tension and solubility. Moreover, the ripening rate was correlated to the deactivation rate of the activated building blocks, i.e., a higher deactivation rate led to a faster ripening of droplets (Figure 3.6d).[133] The authors found that the ripening of these chemically fueled droplets was accelerated by up to two orders of magnitude compared to Ostwald ripening of passive droplets (Figure 3.6e).[133]

The authors explained the acceleration of Ostwald ripening by an increased flux between small and large droplets (Figure 3.6f).[133] They embedded the experimental results into a theoretical framework. As mentioned above, Ostwald ripening is
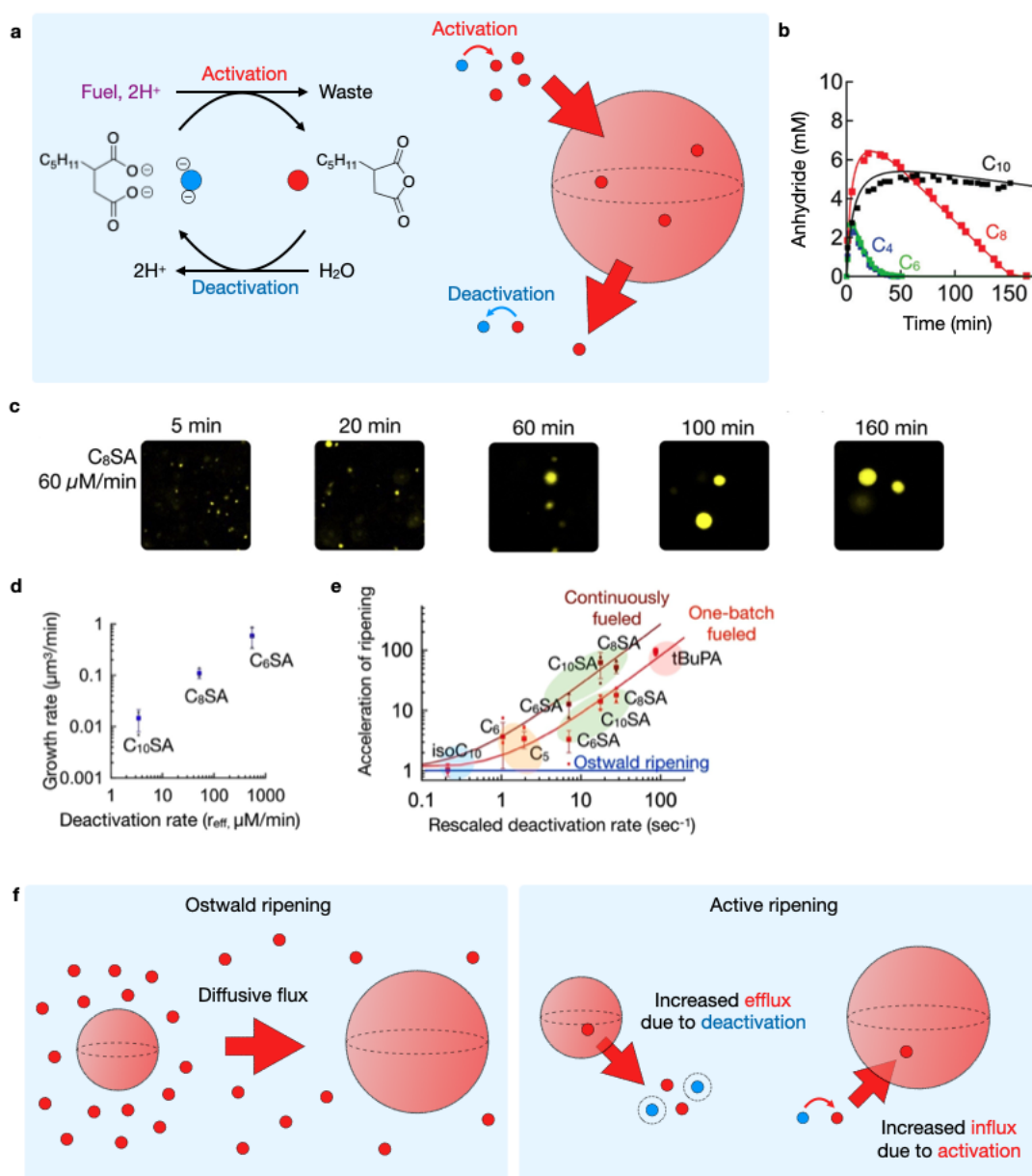
Figure 3.6: Carbodiimide-fueled droplets following design 3.[126] (a) A chemical reaction cycle converts a chemical fuel (EDC) into waste (EDU) and transiently removes two negative charges on a molecule with a hydrophobic tail.[146] A schematic representation of a droplet where a building block is activated and deactivated in the dilute phase. (b) The concentration of activated building block (anhydride) with a varying hydrophobic tail as a function of time after adding 10 mM fuel.[147] Markers represent HPLC data while solid lines represent fits from the kinetic model. Reprinted and adapted with permission from Royal Society of Chemistry, Copyright © 2020. (c) Confocal microscopy micrographs of C8 succinic acid (building block) with continuous fueling of 60 μm/min fuel.[133] (d) Droplet growth rate as a function of the deactivation rate of succinic acid building blocks.[133] (e) Acceleration of ripening as a function of the deactivation rate for various building blocks.[133] The fueling mode and the deactivation rate regulate the degree of acceleration. (f) Schematic representation of the mechanism of Ostwald ripening and active ripening. (c-e) Reprinted and adapted with permission from Tena-Solsona et al., Copyright © BY 4.0, 2020, https://creativecommons.org/licenses/by/4.0/.

driven by a concentration gradient between small and large droplets caused by Laplace pressure differences. Specifically, small droplets have a high concentration of building blocks around them. In contrast, large droplets are surrounded by a lower concentration of building blocks due to a lower Laplace pressure than smaller droplets. In chemically fueled droplets following design 3, the deactivation reaction occurs in the solution. It thus locally lowers the concentration gradient between small and large droplets. Lowering the gradient preferentially removes activated building blocks from small droplets with a high Laplace pressure. In other words, the probability that the deactivated molecule is substituted from a molecule from a small droplet is higher than that from a large droplet. In contrast, activation creates new activated building blocks on the concentration gradient. That excess activated building block is more likely to diffuse down the concentration gradient into larger droplets with a low Laplace pressure.

Taken together, activation accelerates the growth of large droplets. Deactivation preferentially dissolves small droplets. As a result, both reactions contributed to an accelerated ripening until, eventually, only one droplet remained. Unlike droplet designs 1 and 2, this design cannot lead to a stable emulsion.

3.3.2   Design 4: both reactions inside of the droplets

Lastly, I discuss the design where droplet building blocks are activated and deactivated inside the droplets. While theory-based work is scarce on droplets following design 4, Deng and Walther reported an experimental approach based on coacervate droplets that comprise DNA (Figure 3.7a-b).[150] Specifically, DNA-based constructs with complementary sticky ends were activated via ligation and deactivated through cleavage by an enzyme pair, T4 DNA ligase, and BsaI, respectively, resulting in transient elongation of DNA strands. The distance between identical and complimentary sticky ends could tune the multivalency leading to droplets with a broad strand length distribution of up to 1500 base pairs. Concretely, droplets were formed that survived for up to two days, dependent on the amount of ATP added. The authors provided experiments that allow estimating where activation and deactivation took place. First, it was demonstrated that new monomers added to pre-formed fuel-driven droplets were incorporated into the droplet phase within hours (Figure 3.7c).[150] This activation of freshly supplied building blocks shows the dynamic re-shuffling in this droplet system, which indicates that activation occurs in the droplet. Secondly, individual droplets formed vacuoles, indicating that activated building blocks were deactivated within the droplet. Finally, the authors demonstrated that the interactions of complementary sticky ends of DNA are highly specific, allowing for self-sorting mechanisms where droplets made from differently constructed monomers do not fuse and mix material. Such exciting behavior is typically not accessible to other aqueous droplets such as complex coacervates which are composed of non-specific electrostatic interactions.

Two other synthetic examples fulfill the criteria of activation and deactivation occurring inside the droplets. In these cases, the deactivation reaction was associated with morphological changes where activated building blocks were deactivated to form filaments within the droplets instead (Figure 3.7d). Monterroso and co-workers reported coacervate droplets composed of FtsZ and the SlmA protein, a biological inhibitor of FtsZ.[79] Adding GTP temporally transformed the droplets into fibrous
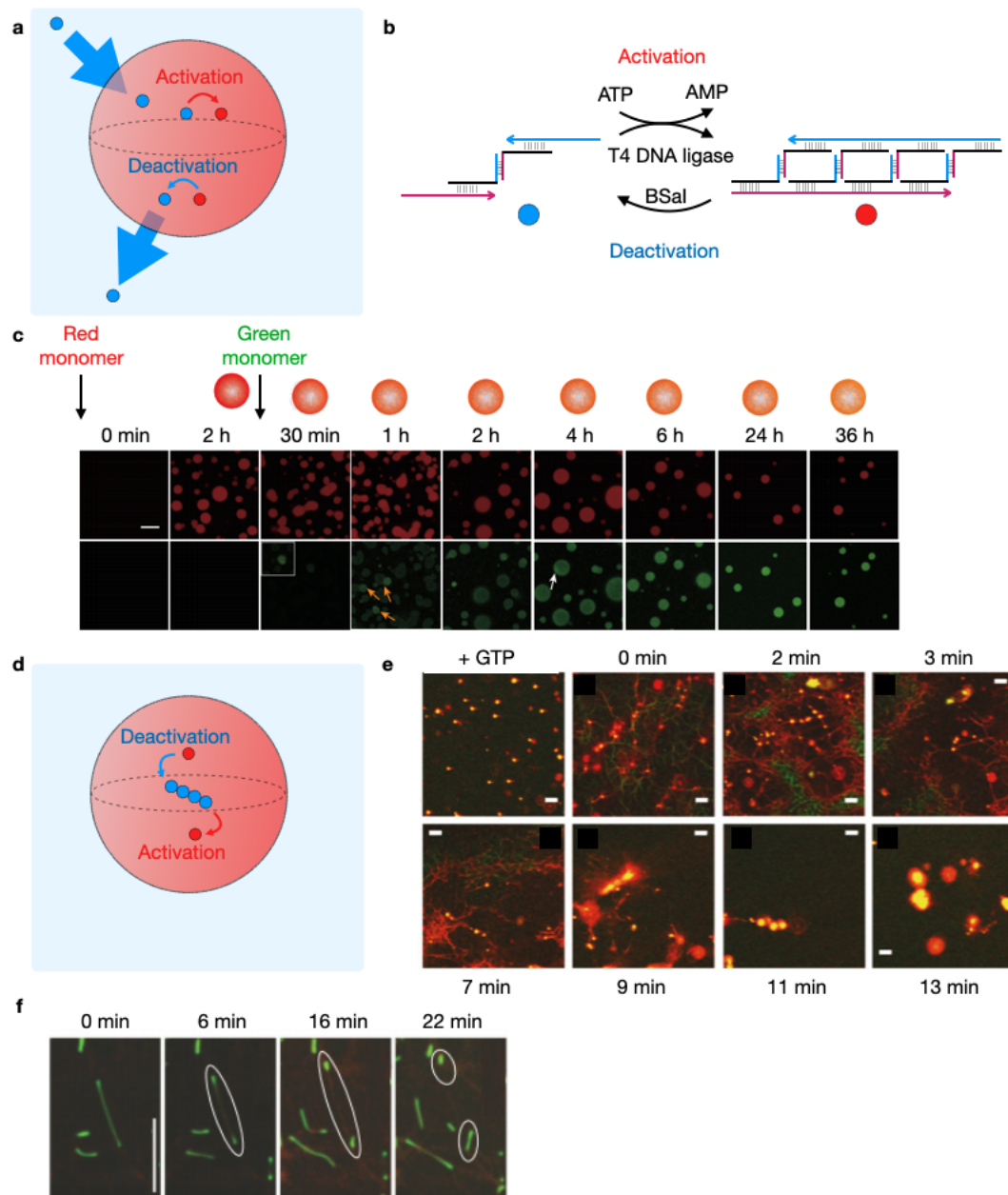
Figure 3.7: ATP- and GTP-fueled droplets following design 4.[126] (a) Schematic representation of a droplet where a building block is activated and deactivated inside the droplet. (b) A chemical reaction cycle where an enzyme pair activates (elongation) and deactivates (shortening) DNA strands inside the droplet at the expense of ATP.[150] (c) Dynamic incorporation of new DNA strands into DNA coacervates.[150] Addition of new DNA strands (green, ATTO488), 2 hr after the formation of DNA coacervates (red, ATTO647). Yellow arrows indicate inhomogeneous fluorescence within droplets due to fusion events that homogenize over the course of several hours (white arrow). Scale bar: 20 µm. Reprinted and adapted with permission from Elsevier, Copyright © 2020. (d) Schematic representation of a droplet where an activated building block is deactivated to form filaments and reactivated inside the droplet. (e) Confocal micrographs of the transient reorganization of FtsZ coacervate droplets to fibers by the addition of GTP.[79] Scale bar: 5 µm. Reprinted and adapted with permission from John Wiley and Sons, Copyright © 2018. (f) Confocal micrographs of a self-dividing fiber that grows from within droplets.[80] Scale bar: 10 µm. Reprinted and adapted with permission from Springer Nature, Copyright © 2018.

structures (Figure 3.7e).[79] These fibers are formed due to a stronger binding and stacking between FtsZ monomers when GTP is present.[138,151] In other words, in the presence of GTP, FtsZ as an activated building block was deactivated to assemble into fibers instead. Activation of FtsZ by GTP hydrolysis then restored the droplets within minutes. Te Brinke et al. published the formation of FtsZ fibrils in GTP/polylysine complex coacervate droplets.[80] In this work, the amount of FtsZ and GTP influenced the change in the droplet morphology (Figure 3.7f).[80] At selected conditions, fibrils grew inside the droplets. These fibrils showed various growth, shrinkage, bending, and fusion behaviors. Excitingly, some fibrils split the original droplet in two. The authors explained this division process by a reaction-diffusion model where deformed droplets favor the elongation at the fibril ends, which is in line with simulations on self-dividing droplets.[131,132]

Co-localizing both activation and deactivation of building blocks into liquid droplets may thus lead to exciting non-equilibrium behavior. Specifically, this experimental work shows the regulation of droplet morphology through chemical reactions which should inspire us to build better liquid droplet models.

Concluding remarks

Chemically fueled droplets show exciting properties that make them a viable model for MLOs. Moreover, the self-division of droplets induced by a chemical reaction cycle is appealing for the origin of life, too. I gave design considerations for chemically fueled droplets and outlined what unique properties can be expected. In the next chapter, I discuss what aspects of experimental models are missing so far and I outline the aims of this thesis.

Chapter 4

Aim of the thesis

In chapter 1, I have outlined the importance of liquid droplet models that are regulated by chemical reactions. In particular, complex coacervate droplets show great potential due to their similarities with cellular droplets. Also, they are interesting candidates as prebiotic compartments due to their aqueous interior that may localize chemical processes without the need for a surrounding membrane. In chapter 2, I described how these droplets can be designed. Numerous experimental models were reported based on coacervate droplets regulated by chemical reactions. However, these models typically evolve from one equilibrium state to another. In other words, the employed chemical reactions either activate or deactivate molecules for phase separation, resulting in the formation of stable droplets or their dissolution. A dynamic model where droplet building blocks are continuously activated and deactivated simultaneously is missing. I have shown in chapter 3 that new behaviors emerge when a chemical reaction cycle is regulating droplet building blocks. However, most work up until now is based on numerical simulations. It remains an open question whether these theoretical predictions are relevant to biology or the origin of life. Is it possible to reproduce these observations experimentally? Does new physics emerge or other unexpected behavior?

The first aim of this thesis was to create a new liquid droplet model that is regulated by a known chemical reaction cycle. For that, I describe in chapter 5 how we designed a chemically fueled droplet model based on complex coacervation. The second aim of this thesis was to understand how chemical reactions can affect the internal organization of droplets. For that, I used the liquid droplet model from chapter 5 and adjusted the design to form multiphase droplets (see chapter 6). The third aim of this thesis was to build a droplet model that is continuously fueled so that it can be compared to the conditions in numerical simulations on chemically fueled droplets. For that, I describe how the droplet model from chapters 5 and 6 can be continuously fueled which can be used to study surprising non-equilibrium transitions (see chapter 7).

Taken together, this thesis aimed to create a new chemically fueled droplet model that can help to verify predictions from theory. By studying this model, new concepts might be developed to understand better the underlying mechanisms that govern cellular droplets in biology. Finally, this model might be useful to understand the droplets' role as prebiotic compartments regulated by simple forms of metabolism.

Chapter 5

Active coacervate droplets as a model for membraneless organelles and protocells

In this chapter, I wanted to construct chemically fueled droplets as a model for membraneless organelles and protocells. Therefore, I designed coacervate droplets composed of a short peptide and RNA that are regulated by a fuel-driven reaction cycle. Excitingly, the droplets' properties such as lifetime and total volume were regulated by the kinetics of the underlying chemical reaction cycle. In other words, when the activated peptide was abundant, many droplets formed and grew via fusion events. When it was scarce, the droplets started to decay. Surprisingly, these droplets did not dissolve solely by shrinkage but through dissolution from within, *i.e.*, forming a hollow droplet with a so-called vacuole. Finally, these droplets self-divided into tiny fragments that survived for tens of seconds before they dissolved. For proof of principle, I also showed that these droplets are relevant protocell models by incorporating functional RNA that remained in its active fold inside the droplets. The transient up-concentration of functional RNA shows that the droplets can be considered potential prebiotic model compartments where the interior of the droplet offers an environment for the evolution of more complex molecules. Also, these droplets are regulated by chemical reactions, making them a great model for membraneless organelles in today's cells.

This work has been published:

Contribution of the authors: C. Donau and J. Boekhoven conceived the research and wrote the manuscript. C. Donau, J. Boekhoven, M. Tena-Solsona, M. Sattler, and H. Mutschler designed the experiments. C. Donau, F. Späth, M. Sosson, B. A. K. Kriebisch, F. Schnitter, M. Tena-Solsona, H-S. Kang, E. Salibi, and J. Boekhoven performed experiments and analyzed the data.

37

Check for updates

Active coacervate droplets as a model for membraneless organelles and protocells

Carsten Donau[1], Fabian Späth[1], Marilyne Sosson[1], Brigitte A. K. Kriebisch[1], Fabian Schnitter[1], Marta Tena-Solsona[1,2], Hyun-Seo Kang [1,3], Elia Salibi[4], Michael Sattler[1,3], Hannes Mutschler [4] & Job Boekhoven [1,2✉]

Membraneless organelles like stress granules are active liquid-liquid phase-separated droplets that are involved in many intracellular processes. Their active and dynamic behavior is often regulated by ATP-dependent reactions. However, how exactly membraneless organelles control their dynamic composition remains poorly understood. Herein, we present a model for membraneless organelles based on RNA-containing active coacervate droplets regulated by a fuel-driven reaction cycle. These droplets emerge when fuel is present, but decay without. Moreover, we find these droplets can transiently up-concentrate functional RNA which remains in its active folded state inside the droplets. Finally, we show that in their pathway towards decay, these droplets break apart in multiple droplet fragments. Emergence, decay, rapid exchange of building blocks, and functionality are all hallmarks of membrane-less organelles, and we believe that our work could be powerful as a model to study such organelles.

[1] Department of Chemistry, Technical University of Munich, Lichtenbergstrasse 4, 85748 Garching, Germany. [2] Institute for Advanced Study, Technical University of Munich, Lichtenbergstrasse 2a, 85748 Garching, Germany. [3] Institute of Structural Biology, Helmholtz Zentrum München, Ingolstädter Landstrasse 1, 85764 Neuherberg, Germany. [4] Max Planck Institute of Biochemistry, Am Klopferspitz 18, 82152 Martinsried, Germany. ✉email: job.boekhoven@tum.de

37

M embraneless organelles, which include the nucleoli and P granules, rely on liquid–liquid phase separation in order to compartmentalize biochemical reactions.[1–6] They typically comprise proteins and RNA held together by entropic and ion-pairing effects in a process called complex coacervation,[7] resulting in an organelle with liquid-like properties.[8,9] Recent work has demonstrated that some of these organelles are actively regulated by ATP-dependent chemical reaction cycles.[7,9,10] These findings suggest that some of the membraneless organelles are active droplets, i.e., these droplets exist out of equilibrium and are regulated by chemical reactions. However, how the cell regulates phase separation of these droplets remains poorly understood.

Numerous synthetic complex coacervate-based droplets exist,[11–18] which are used to investigate the characteristics of membraneless organelles.[19,20] Examples of reversible complex coacervate droplets have been reported that form or dissolve upon a change in pH,[21] temperature,[19] salt or polymer concentration,[19,22] or in response to UV light[23] or an enzymatic reaction[24–26]. These models provide valuable information on the formation or dissolution of droplets. However, these droplets evolve from one equilibrium state to another (e.g., from droplets to solution) in response to a change in their environment. An ideal model to study how dynamic assembly and disassembly affect droplet behavior would include the fuel-driven behavior as observed in biology.[27,28] Such a model could reveal insights on how chemical reactions regulate droplet growth or how kinetics can regulate droplet composition. Moreover, chemically fueled active coacervate droplets have been proposed as a protocell model capable of self-division.[29,30]

The field of fuel-driven self-assembly has recently gained traction.[31–34] Here, the self-assembly of molecules is regulated by a chemical reaction cycle that comprises two reactions: a building block activation and deactivation reaction. In the activation, a precursor molecule is activated for self-assembly by the irreversible consumption of a chemical fuel. In the deactivation, the product is reverted to the precursor. Consequently, the self-assembling product is present for a finite amount of time, and the assembly's properties are regulated by the kinetics of the reaction cycle. Such kinetic regulation is inspired by biology's mode of controlling assemblies like the membraneless organelles. Examples of synthetic dissipative assemblies include fibers driven by photochemical[35] or fuel-driven reaction cycles,[36–40] vesicles driven by ATP[41] or carbodiimides,[42] and others.[43]

In this work, we thus introduce a model for membraneless organelles based on complex coacervate droplets regulated by a fuel-driven chemical reaction cycle. We find that droplet behavior is regulated by the conversion of a chemical fuel. For example, these droplets form spontaneously and decay in the absence of fuel. Moreover, in their pathway towards decay, they show active behavior such as the formation of vacuoles and breaking apart into fragments. Finally, we show that functional RNA, like ribozymes, can be transiently up-concentrated in these droplets and can remain in its active folded state inside the droplets.

Results and discussion
Design of fuel-driven complex coacervation. The active droplets are based on the complexation of RNA and a peptide. The RNA component of the droplets is homo-polymeric RNA (poly-U, ± 2,200 bases), which is frequently used in coacervate-based studies.[19,25,44,45] The droplet dynamics are regulated by a peptide of which the RNA affinity is controlled by a chemical reaction cycle. The activation reaction converts a negatively charged aspartate into its corresponding anhydride driven by the hydrolysis of EDC (1-ethyl-3-(3-dimethylaminopropyl)carbodiimide,

fuel) to its urea (EDU, Fig. 1a and Supplementary Fig. 2).[46–49] In the deactivation reaction, the anhydride product spontaneously hydrolyzes to the precursor peptide. The result is a transient anhydride at the expense of EDC.

The design criteria for the peptide were that in the anhydride state (product), it can induce complex coacervation with poly-U (RNA), but not the aspartate state (precursor). We tested several peptide designs (see Table 1), but the most successful sequence was: Ac-FRGRGRGD-OH (phenyl alanine (F), arginine (R), glycine (G), and aspartate (D), Fig. 1a). In our design, three cationic arginines were required to interact with the anionic RNA. However, in line by reports with others, it appeared to be crucial to separate the charges with the non-charged glycine amino acid. That motif is also a common motif in biology and membraneless organelle related proteins.[50–52] We purposefully terminated the sequence with an aspartate. Thus, in the precursor state, the overall charge of the peptide was +1, but in the product state, it was +3. In that way, droplet formation via complex coacervation is expected for the product but not the precursor (Fig. 1b).

Transient formation of droplets. We dissolved 23 mM of the peptide precursor in an aqueous 200 mM MES buffer solution at pH 5.3 with 4.1 mM RNA (expressed in [Uracil nucleotides]). Isothermal titration calorimetry (ITC) showed a weak interaction between the precursor and the RNA with a dissociation constant (K_d) of 2.9 mM (see Supplementary Fig. 3). The precursor solution was optically clear (Fig. 2a), pointing towards the absence of droplets.

In contrast, upon the addition of 25 mM EDC (fuel), the solution immediately turned turbid (Fig. 2a) as a result of droplet formation. The fuel-induced turbidity faded rapidly, and the solution was clear after 18 min. Control experiments confirmed that the transient droplet formation was a result of fuel, RNA, and peptide combined (see Supplementary Fig. 4). In addition, droplets re-emerged after the addition of a second batch of fuel (see Supplementary Fig. 5). A plate reader-study confirmed the rapid increase of turbidity after the addition of fuel to a maximum reached after 3 min (Fig. 2c, black trace). After 18 min, the turbidity decayed to its original level.

The concentrations of the product and fuel were measured by HPLC, and the data was used to develop a kinetic model that predicts the concentration of fuel, precursor, and product throughout the cycle (Fig. 2c, Supplementary Fig. 6, and Table 2). Noteworthy, one set of rate constants in our kinetic model could accurately predict the kinetic profiles of the fuel, precursor, and product. That is a good indication that the droplets do not affect the reaction kinetics of product activation or deactivation. The concentration of fuel rapidly decayed (see Supplementary Fig. 6), leading to the transient presence of product (Fig. 2c). Moreover, the time at which the fuel was depleted coincided with the time at which we detected no more product. Therefore, fuel was present throughout the cycle and, thus, activation and deactivation were always operating simultaneously. We noted a strong correlation between HPLC data and the turbidity: at the highest product concentration, the turbidity peaked, and, when the product and fuel were exhausted, the samples returned to transparent. We refer to these droplets as "dynamic droplets" since their presence and absence seemed to be dynamically regulated by the kinetics of the reaction cycle.

The droplets behaved differently when more fuel (60 mM) was added (Fig. 2d). While HPLC showed that the fuel and product were absent after 30 min (see Supplementary Fig. 6), the turbidity of the solution persisted for 76 min. The latter observation was a strong indication that these droplets were in a kinetically arrested state; despite being transient, the dynamics of disassembly were
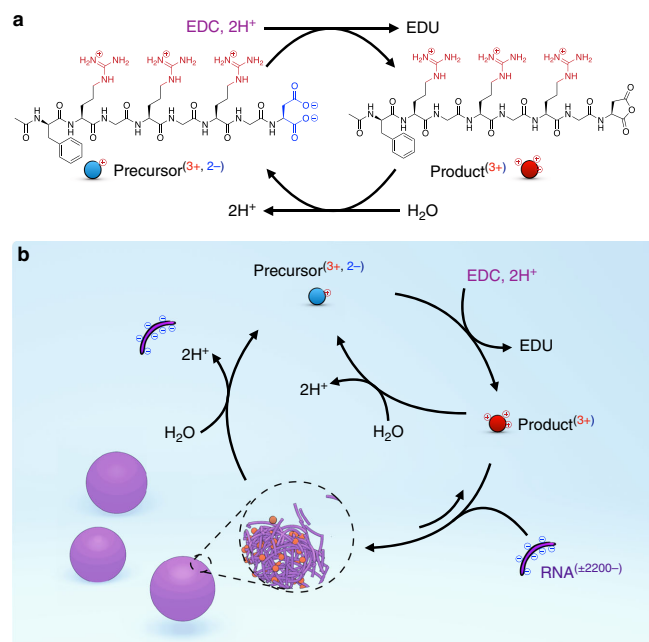
Fig. 1 Coacervation between a peptide and RNA driven by a chemical fuel. a The chemical reaction cycle that converts a chemical fuel (EDC) into waste (EDU) while removing two negative charges on a peptide (precursor) resulting in a cationic transient anhydride (product). **b** A schematic representation of the chemical reaction cycle combined with complex coacervation with RNA (poly-U). The influx and efflux of droplet materials are regulated by the chemical reaction cycle.

much slower than the kinetics of the reaction cycle allowing the droplets to persist for longer. We refer to these droplets as metastable droplets.

We performed the same experiments with various fuel concentrations to make a phase diagram (Fig. 2e and Supplementary Fig. 7). We found that more than 7.5 mM fuel was required to induce an increase in turbidity, which corresponds to 0.9 mM product. This result suggests a critical coacervation concentration of 0.9 mM anhydride product. Between 7.5 mM and 40 mM fuel, we found dynamic droplets. Above 40 mM of fuel, the droplets were metastable. We tested the effect of the RNA concentration on the droplet's behavior (Fig. 2f and Supplementary Figs. 8 and 9). For any RNA concentration, no increased turbidity was observed below 7.5 mM fuel, indicating that the RNA concentration was not the limiting factor for droplet formation. At lower RNA concentrations, less fuel was required to obtain the metastable droplets, e.g., 25 mM fuel or more for 1.4 mM RNA. We hypothesized that these metastable droplets can complex most RNA in the solution and that addition of more fuel results in more peptide product per RNA. The increased ratio of peptide to RNA results in an increased packing density compared to dynamic droplets, which may increase the energy barrier for disassembly. We thus measured the RNA concentration in the phase outside of the droplets. We used fluorescently labeled RNA to form dynamic droplets (25 mM fuel, 4.1 mM RNA), and, after 2 min, the droplet-containing solution was centrifuged to separate the two phases. Fluorescence spectroscopy showed that 10% of the initially added RNA remained in the supernatant (see Supplementary Fig. 10).

In contrast, no RNA was found in the supernatant when we did the same experiment with metastable droplets (60 mM fuel). The data from these experiments indicate that dynamic droplets leave behind some RNA in the outer phase, whereas metastable droplets capture all RNA.

Next, we measured the concentrations of fuel and product after filtering the droplet solution (see Supplementary Fig. 11). The filtration removed all droplets, and the measurements were thus indicative of the concentration of fuel and product outside of the droplets. Moreover, this data, combined with the dataset without filtration, was used to calculate the respective concentrations inside and outside of the droplet phase. For both dynamic (25 mM fuel) and metastable droplets (60 mM fuel), the concentration of fuel with or without filtration was similar, which suggest almost all fuel was present in the phase outside of the droplets at all times (see Supplementary Fig. 11a). This observation suggests that the activation of our reaction cycle predominantly occurs outside of the droplets in accordance with our design in Fig. 1. In contrast, we found a large decrease in the concentration of product when the samples were filtered compared to without filtration, especially early in the cycle (see Supplementary Fig. 11b). That observation suggests that the droplets comprise a significant amount of the anhydride product. Specifically, after 2 min, we measured that 1.7 mM product remained in the filtrate for the dynamic droplets (roughly 55% of the total product). Next, we measured the volume of the droplet phase by centrifuging the total solution and measuring the volume of the pellet. That volume, combined with the missing fraction of product, allows us to calculate the concentration of product inside

39
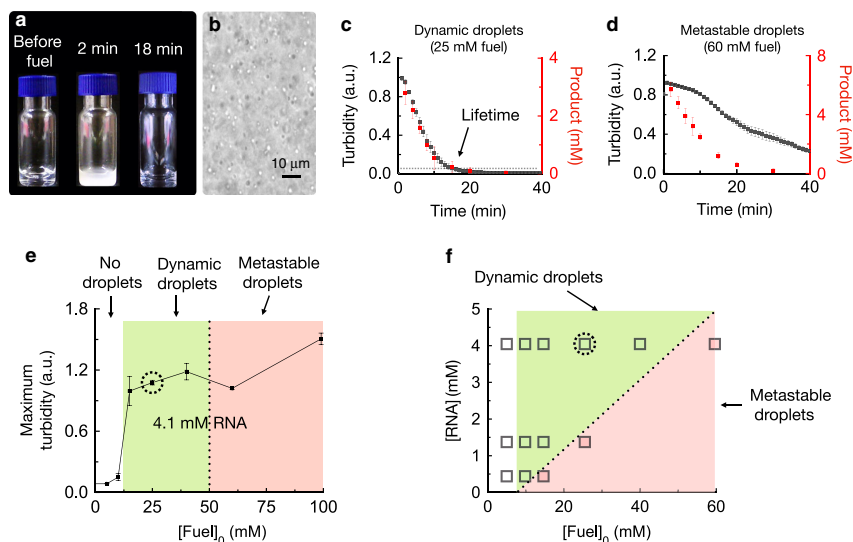
Fig. 2 Macroscopic analysis of the droplets. a Photographs of solutions of 23 mM Ac-FRGRGRGD-OH (precursor), 25 mM EDC (fuel), and 4.1 mM poly-U (RNA, monomer concentration), before, 2 min after and 18 min after the addition of fuel. **b** Bright field-micrograph of a solution described in **a** after 2 min. **c**, **d** Absorbance of 600 nm light as a measure of turbidity (left y-axis, black traces) and anhydride product concentration in the solution (right y-axis, red traces) as a function of time for the same condition as described in **a** with 25 mM fuel (**c**) or 60 mM fuel (**d**). Dynamic droplets show a strong correlation between the concentration of product and the turbidity. **e** The maximum turbidity as a function of fuel for samples with 4.1 mM RNA. The three regimes are shaded: no droplets (white), dynamic droplets (green), and metastable droplets (red). **f** Behavior of the droplets as a function of RNA monomer concentration and amount of fuel. All error bars show the standard deviation from the average ($N = 3$).

the droplets. We found that, after 2 min, ~0.9 M product was inside the dynamic droplets, while ~1.8 M was present inside the metastable droplets (see Supplementary Fig. 11c). These observations mean that metastable droplets comprised roughly two times more product than dynamic droplets. Considering that the amount of RNA in the droplet phase was almost similar in these experiments (*vide supra*), the ratio of product to RNA was significantly higher in metastable droplets. Specifically, the ratio of cations to anions, after 2 min, was 2.0 for the metastable droplets compared to 1.1 for the dynamic droplets.

From the experiments above we can conclude that precursor and RNA do not sufficiently interact, and cannot form droplets without activation of the peptide. The active product, in contrast has a higher affinity to the RNA leading to phase-separated droplets. Since coacervate droplets are typically highly hydrated, the product hydrolyzes back to the precursor inside of the droplets, decreasing the affinity between the peptide and RNA. In the case of dynamic droplets that loss in affinity leads to the immediate dissolution of droplets. In the case of metastable droplets, the deactivation of the product does not immediately disassemble the droplets. We hypothesize that, even though droplet dissolution is thermodynamically favored, the disassembly process is kinetically hindered. Compared to dynamic droplets, more peptide per unit of RNA is present in metastable droplets, which may result in an increased barrier of disassembly. We have observed such differences in the energy landscape in other chemically fueled assemblies[46,53].

Droplet evolution and disassembly. We further studied the emergence, evolution, and decay of the dynamic and metastable

droplets by confocal microscopy using Cy3-tagged A15 hybridized with RNA (Fig. 3a, b). In the first part of the cycle of dynamic droplets, the droplets were spherical and polydisperse (Fig. 3a). Halfway through the cycle, vacuoles (holes) started to appear in the remaining droplets. Towards the end of the cycle, the droplets suddenly fragmented in smaller, not perfectly spherical droplets. These final fragmented droplets finally dissolved. We quantified the above described trend by calculating the droplet number, their size, and their average fluorescence intensity (Fig. 3c–e, black traces). Within a minute after addition of 25 mM fuel, we observed a high number of droplets (Fig. 3a, c). In line with the turbidity measurements, the droplet number decayed after 3 min. Towards the end of the cycle, the number of droplets suddenly increased (Fig. 3c). The droplet volume immediately increased early in the cycle and started to decrease after 12 min (Fig. 3d). We found a high fluorescence intensity that rapidly decayed as time progressed (Fig. 3e). The decay in the intensity points to the fast release of RNA as droplets collapse.

When we performed the same experiments with the metastable droplets (60 mM fuel), we also found a high number of spherical, polydisperse droplets in the first minutes (Fig. 3b). Again, the droplet number rapidly decreased (Fig. 3c, red traces). However, droplets were still present even after complete fuel consumption (e.g., 60 min). After 20 min, the average volume of the metastable droplets remained constant (Fig. 3d). The most obvious difference between dynamic and metastable droplets was in their mean intensity of the fluorescent RNA (Fig. 3e). In dynamic droplets, the intensity decreased as the cycle progressed while in metastable droplets, it did not change significantly throughout the cycle. We conclude that the RNA remained in metastable droplets, long after all product had hydrolyzed (e.g., 40 min).
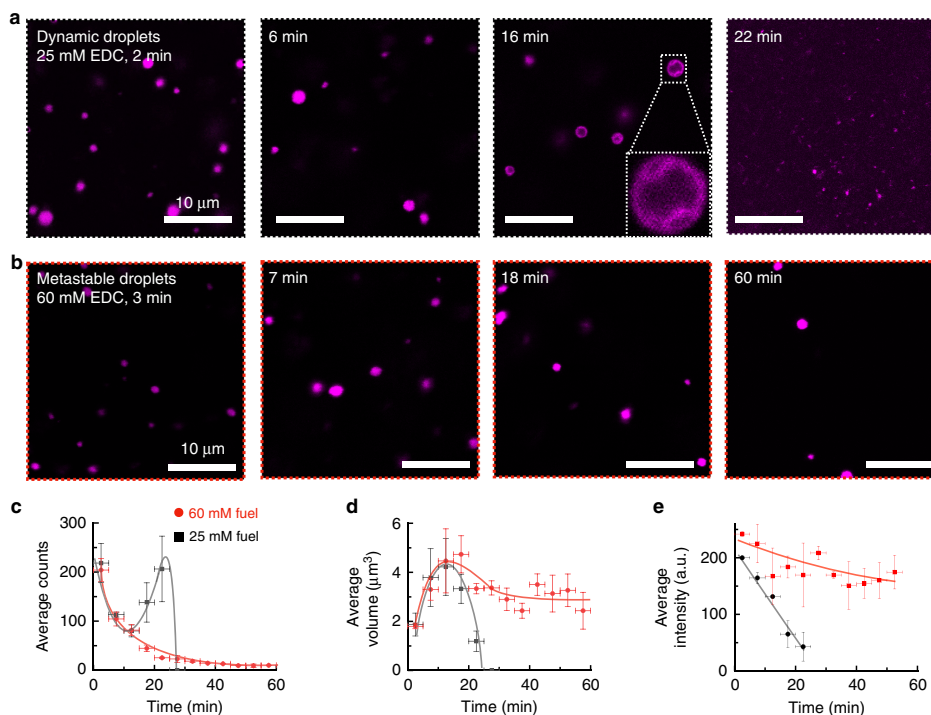
Fig. 3 Microscopy analysis of dynamic and metastable droplets. a, b Confocal micrographs of solutions of 23 mM precursor and 4.1 mM poly-U (Cy3-A15 hybridized) after the addition of 25 mM EDC (**a**) or 60 mM EDC (**b**). **c–e** Statistical analysis of confocal micrographs of the solutions described in **a** (black squares) and **b** (red circles) for the number (**c**), volume (**d**), and the average intensity (**e**) of the respective droplets after addition of fuel. Vertical error bars show the standard deviation from the average ($N = 3$). Horizontal error bars show binned data of 5 min. The lines are added to guide the eye. Source data are provided as a Source Data file.

In other words, the peptide is able to hold together the droplet to some degree after it has been deactivated.

Confocal microscopy time-lapses with higher acquisition rates revealed further dynamic behavior in the dynamic droplets (Fig. 4a and see Supplementary Movie 1). We could not observe the droplet nucleation, likely because it occurred rapidly after fuel addition (20 mM fuel). In the first minutes, we did observe a frequent fusion of the small droplets (Fig. 4b), which is common for coacervate-based droplets.[54] As time progressed, fusion became less apparent. After 12 min, we observed the first formation of vacuoles. In some cases, we found multiple vacuoles per droplet that grew or fused until they became the major component of the droplet (Fig. 4c). Interestingly, as the vacuoles grew, the droplet itself also increased in size, likely because of water uptake (see Supplementary Movie 2). We hypothesize that vacuoles are a result of deactivation of the peptide and the consequent efflux with RNA. The efflux is hindered by a diffusion barrier formed by the remaining part of the droplet, which yields in the accumulation of RNA at the droplet periphery. Moreover, studies of membraneless organelles in vitro[22] and in vivo[55] showed the dynamic formation of similar vacuoles. Around 14 min after fuel addition, we observed the first dissolution events of droplets (Fig. 4d, e). The droplet lost its roundness, and protrusions formed. Excitingly, these protrusions pinched off and became independent segments of the original droplets

(Fig. 4e and Supplementary Movies 3 and 4). In some cases, these segments drifted off by Brownian motion and could survive for tens of seconds before finally dissolving. Such droplet fragmentation would be a form of ill-controlled asymmetric division, which occurs as the original droplet is losing integrity due to the loss of anhydride product, which we will further study in future work.

From these combined experiments, we conclude that dynamic droplets almost immediately nucleate and take up RNA rapidly in response to fuel. Then, their average volume grows, while their number decreases due to fusion events. When product deactivation is faster than peptide activation, the product concentration starts decreasing, and the droplets release RNA, as can be concluded from the decline in the fluorescence intensity. In some cases, this release of RNA is hindered by the droplet itself and results in vacuole formation, i.e., areas with low RNA surrounded by a diffusion barrier with high RNA concentration. Towards the last minutes of the cycle, the droplets rapidly collapsed resulting in fragmentation and further release of the RNA.

Transient up-concentration of functional RNA. Complex coacervate droplets containing RNA have frequently been proposed as a potential protocell that emerged at the origin of life.[12,56] To demonstrate that our dynamic droplets can indeed up-concentrate functional RNA during their limited lifespan, we

41
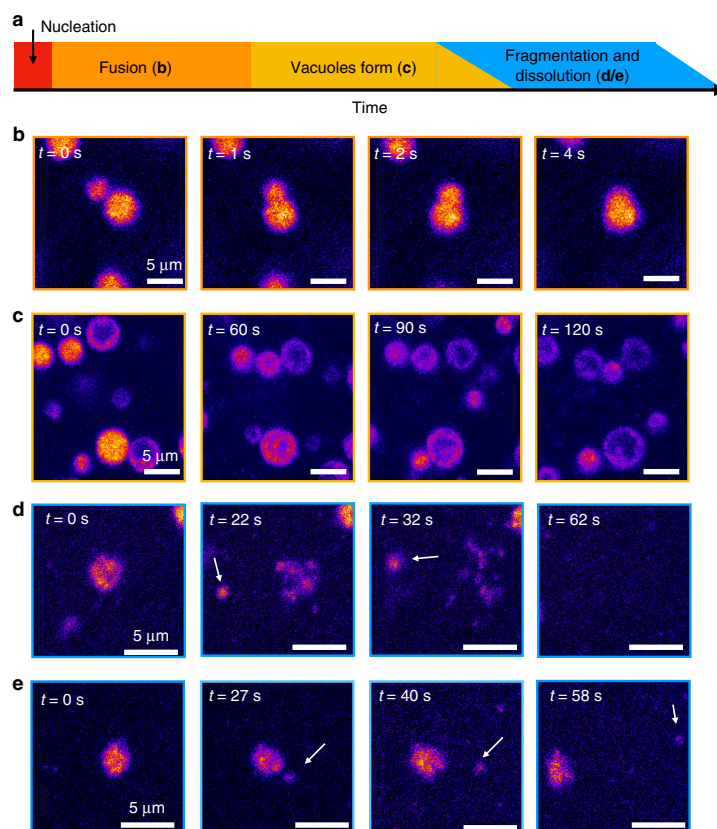
Figure 4 Microscopy analysis of the behavior of dynamic droplets. a The sequence of events occurring during the lifetime of dynamic droplets.
b–e Selected events of confocal micrograph time-lapses of solutions of 23 mM precursor and 4.1 mM poly-U (Cy3-A15 hybridized) after addition of 20 mM
EDC. **b** Fusion of droplets at the beginning of the cycle (<5 min). **c** Vacuole formation towards the end of the cycle (>12 min). **d, e** The fragmentation and
dissolution of a droplet, ~15 min after fuel addition. In some cases, the fragments survive for tens of seconds as indicated by the white arrows. Experiments
were performed for $n > 10$.

investigated the evolution of partitioning of functional RNA
sequences into the dynamic droplets (Fig. 5a–c). We used a
ligating ribozyme, a cleaving ribozyme, and a fluorophore-
binding aptamer (SunY,[57] Hammerhead,[12] and Broccoli,[58]
respectively). Their sequence and synthesis details are provided in
Tables 3–6. We added fuel to the solutions containing the pre-
cursor, poly-U, and one of the functional RNA sequences, and
imaged the droplets by confocal microscopy. Five minutes after
the addition of fuel (25 mM), we observed that all three functional
RNA sequences had partitioning coefficients >10. (Fig. 5b and
Table 3). In line with other reports, the partitioning seemed to be
size-dependent; i.e., the longest sequence had the highest parti-
tioning coefficient (SunY, 187 nucleotides, $K = 37$), while the
shortest strand had the lowest (Hammerhead, 44 nucleotides,
$K = 13$). As the cycle was progressing, an increasing amount of
functional RNA was observed outside of the droplets until the
droplets dissolved (Fig. 5c). Taken together, upon emergence, our
droplets partition the functional RNA, and release it upon decay,

resulting in the transient up-concentration of functional RNA
driven by a chemical reaction cycle.
To test whether functional RNA remains active in our droplets,
we first tested the robustness of the reaction cycle against metal
ions, such as potassium and magnesium, and temperature which
are important biochemical parameters (see Supplementary Fig. 12).
In general, the turbidity decreased with increasing salt concentra-
tion which is common for coacervation due to screening effects.
Below 50 mM of salt as well as at 37 °C, fuel-driven droplets can
still be formed and thus opening the possibility for compartmen-
talized biochemical reactions. We therefore examined the binding
of the Broccoli aptamer to its ligand DFHB1T by fluorescence
spectroscopy. DFHB1T is non-fluorescent, but, upon binding with
Broccoli, emits bright green fluorescence.[58] When we added the
ligand to a buffered solution of precursor, poly-U and Broccoli at
low to medium levels of magnesium and potassium, the
fluorescence intensity increased by a factor of 5 (Fig. 5d). Addition
of 10 mM fuel decreased the intensity by 30% in the first minutes
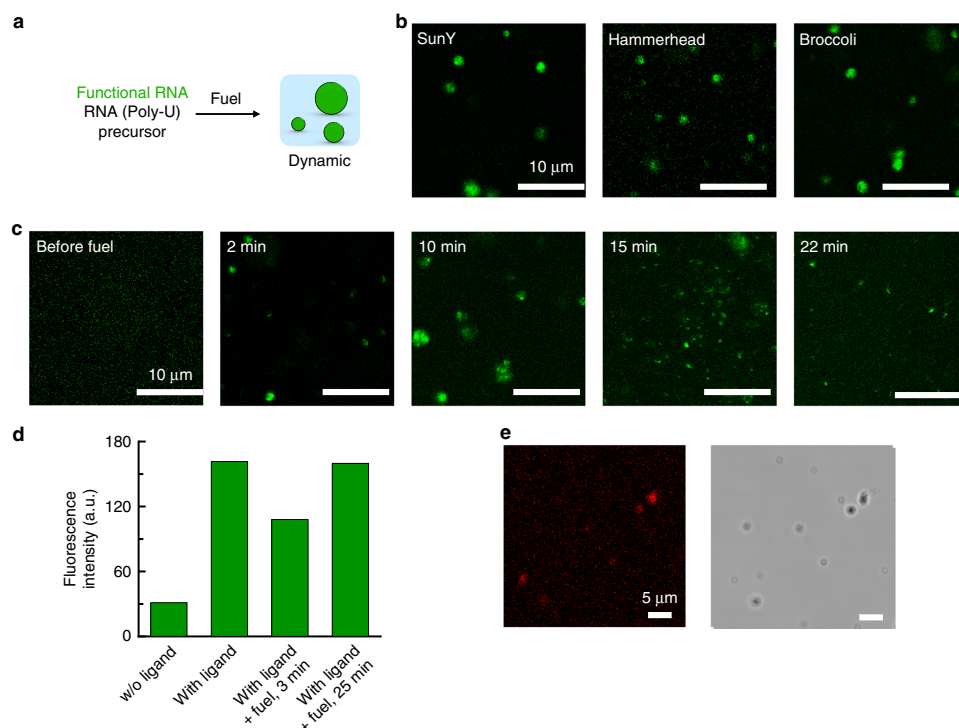
Fig. 5 Functional RNA inside fuel-driven droplets. a Schematic representation of the experimental procedure for dynamic droplets with functional RNA. **b** Confocal micrographs of 23 mM precursor, 4.1 mM poly-U, 25 mM EDC with 0.2 μM Cy5-RNA (SunY ribozyme, Hammerhead ribozyme or Broccoli aptamer), 5 min after addition of EDC. **c** Confocal micrographs of the SunY containing solution described in **d** (with 27 mM EDC) at different time points before or after EDC addition. **d** Fluorescence intensity of solutions containing the Broccoli aptamer with or without DFHB1T (ligand), in the presence and absence of droplets. Maximum fluorescence intensity at 504 nm. Standard conditions with 2 mM MgCl₂, 30 mM KCl, and 1.5 μM Broccoli aptamer. Addition of 10 mM EDC (fuel) to induce droplet formation. **e** Confocal and bright field micrographs under the conditions described in **d**, 5 min after the addition of 15 mM EDC. Experiments were perfomed for $n = 2$. Source data are provided as a Source Data file.

followed by a complete recovery once all fuel has been consumed. The decrease in intensity is likely because the droplets increase the sample's turbidity. We performed the same experiment at the confocal microscope to examine where the binding of the aptamer with the ligand occurs once droplets are present. In line with the broccoli partitioning, the broccoli-DFHB1T complex colocalizes within the droplets by more than an order of magnitude (Fig. 5e). We thus conclude that functional RNA can remain in its folded active state inside the droplets which is an important prerequisite for ribozyme activity. In future work, the combination with self-replicating RNA strands could result in the up-concentration and activation of catalytic RNA sequences whose activity helps to sustain the droplets.

We made droplet formation via complex coacervation a fuel-driven process. RNA-containing droplets emerge in response to fuel and decay when the fuel is depleted. We envision that our droplets could be powerful to study how chemical reactions can regulate liquid–liquid phase-separated droplet behavior, which could provide valuable insight in the mechanisms that govern membraneless organelles. We also believe these droplets can serve as a great model for protocells, as they spontaneously emerge and decay. We show that they transiently partition functional RNA

which is able to remain in its active folded state. More excitingly, we show the first signs of spontaneous asymmetric division towards the end of a coacervate droplet cycle.

Methods

Primers, RNA, and splints. All DNA primers were bought from IDT (see Supplementary Table 4). Primers were annealed and filled in using the Taq polymerase to create dsDNA templates used for T7 transcription and the RNA sequence listed in Supplementary Table 5. The underlined sequences are complementary to the Cy5-tagged pentamer, whereas the rest of the 10 nucleotides are complementary to the 3′ end of the respective RNA (see Supplementary Table 6).

General sample preparation. For most experiments, we used these standard conditions: 23 mM Ac-FRGRGRGD-OH (tri-trifluoroacetic acid salt), 4.1 mM poly-U (uridine units), 200 mM MES, pH 5.3, and 25 mM EDC (in case of dynamic droplets) or 60 mM EDC (metastable).

Stock solutions of the precursor (75 mM, tri-trifluoroacetic acid salt), MES buffer (500-1000 mM), poly-U (600-1000 kDA, ~2-15 µg/µL), and EDC (1–2 M) were prepared in nuclease-free water. The pH of the peptide and MES stock were adjusted to 5.3. Typically, stock solutions of EDC and poly-U as well as the resulting peptide-poly-U solution in MES were prepared freshly for each experiment. Reaction networks were started by addition of EDC to the peptide-poly-U solution in MES.

ITC measurements. All ITC measurements were performed using a MicroCal PEAQ-ITC instrument (Malvern Pananalytical) by injecting (26 points, 1.5 µL/inj) with a total of 37.5 µL of Ac-FRGRGRGD-OH (38 mM in 200 mM MES, pH 5.3) into 250 µL of poly-U (1.1 mM uridine units in 200 mM MES, pH 5.3) into the cell at 25 °C, reaching a final molar ratio of 6.6 (peptide/RNA). Using the MicroCal PEAQ-ITC Analysis software (v1.22), for each experiment first, a control experiment was subtracted, where the peptides (38 mM in 200 mM MES, pH5.3) were titrated into 200 mM MES (pH5.3) in the absence of RNA. All experiments were performed in triplicate (N = 3).

Turbidity measurements and lifetime determination. Turbidity measurements were carried out at 25 °C on a Microplate Spectrophotometer (Thermo Scientific Multiskan GO, Thermo Scientific SkanIt Software 6.0.1). Measurements were performed in a non-tissue culture treated 96-well plate (Falcon, flat bottom). Every minute, the absorbance of the 200 µL samples was measured at 600 nm. All experiments were performed in triplicate. The lifetime refers to the time it takes for the absorption to drop under 0.01 a.u. (blank subtraction) after EDC addition.

Kinetic model. A kinetic model written in MATLAB (v9.7.0) was used to predict the evolution of the EDC, precursor, and anhydride concentration over time. The model is described in detail in our previous work[41]. The rate constants we used in this work are given in Table S2. The Matlab-code we used is available here: https://github.com/BoekhovenLab/Dynamic-droplets. Briefly, a set of differential equations determines the concentration of EDC, precursor, O-acyl urea, EDU, and anhydride in the cycle every second.

Determining the concentrations in the total reaction mixture. The kinetics of the chemical reaction networks were monitored over time by means of analytical HPLC (Thermofisher Dionex Ultimate 3000, Hypersil Gold 250 × 4.6 mm, Chromeleon software 7.2 SR4). The turbid (in case of 5 mM EDC: clear) samples were directly injected without further dilution, and all compounds involved were separated using a linear gradient of ACN (2 to 98%) and water with 0.1% TFA.

Calibration was not possible for the anhydride product due to its intrinsic instability, proximity to the original precursor peak as well as low yield. Instead, an indirect quantification technique was used by converting the anhydride irreversibly into a mono-amide to determine the anhydride concentration (see Supplementary note 1). Measurements were performed at 25 °C. Briefly, after the addition of EDC (total volume = 200 µL) into a mixture of peptide and RNA in buffer (see general sample preparation), 20 µL of the turbid (in case of 5 mM EDC: clear) reaction mixture were added into 10 µL of an aqueous solution of benzylamine (900 mM) at each time point. The resulting clear solution (pH > 9) was then measured via HPLC to determine [mono-amide].

Method to determine the anhydride and EDC concentrations outside the droplet phase. Due to the inherent instability of the transient coacervate droplets, we chose a filtration protocol which separates the droplet phase from the phase outside of the droplets (see below). Moreover, unlike conventional centrifugation protocols in literature, this method allows for fast separation and enables us for fast quenching of the solution with benzylamine.[59] The speed of the separation method is important because anhydride product is constantly being produced in the supernatant due to the presence of EDC and precursor peptide, which can be calculated with our model. After calculating the anhydride concentration from the HPLC experiments of the filtrate, we corrected the resulting values for the anhydride product which was generated in the supernatant after separation from the droplet phase according to the model (typically it took 15–25 s between filtering and quenching). From these results, we can estimate the amount of EDC and anhydride in the droplet phase by subtraction from the total amount in both phases. In order to calculate the concentrations of

anhydride in the droplet phase, we measured the total droplet volume via centrifugation of the samples after fuel addition and comparing the droplet phase to a set of size standards visually.

After the addition of EDC (total volume = 100 µL) into a mixture of peptide and RNA in 300 mM buffer (see general sample preparation), the coacervate solution was filtered using regenerated cellulose filters (0.45 µm, 13 mm, Whatman SPARTAN) at each time point. In all, 20 µL of the resulting filtrate (clear solution) was added into 20 µL of an aqueous solution of benzylamine (1 M), while the residual 20–40 µL were added into a separate vial for EDC quantification. The anhydride (see benzylamine quenching method) and EDC concentrations of the supernatant were then calculated for both samples via HPLC. All experiments were performed in triplicate (N = 3).

Fluorescence spectroscopy. Fluorescence spectroscopy was performed on a Jasco (Jasco FP-8300, SpectraManager software 2.13) spectrofluorimeter with an external temperature control (Jasco MCB-100).

Method to determine the RNA concentration in the supernatant. In order to quantify the RNA inside the droplets, we hybridized poly-U with a Cy3-A15 (100 nM) prior to the experiment. After the addition of EDC (total volume = 300 µL) into a mixture of peptide and RNA in buffer (see general sample preparation), the coacervate solution was centrifuged 2 min after fuel addition at 20,412×g for 2 min. In total, 200 µL of the supernatant were pipetted into a cuvette and the fluorescence of the sample was measured between 550 and 600 nm. The experiment was performed for different fuel concentrations and we calculated the RNA concentration in the supernatant.

Confocal fluorescence microscopy. Confocal fluorescence microscopy was performed on a TCS SP5 II confocal microscope (Leica LAS AF, v2.6.3.8173) using a ×63 oil immersion objective. Samples (total volume = 15–50 µL) were freshly prepared as described above, but with 0.1–0.5 µM Cy3-A15 or Cy5-A15 as dye. In all, 5 µL of the sample were deposited on PEG-coated glass slides and covered with a 12-mm diameter coverslip. After tracking the droplets on the microscope for 4–5 min, again 5 µL of the sample was deposited on the glass slide and imaged instead of the previous sample portion. This process was repeated for the first 25 min of the experiment. Samples were excited with 561 nm and 633 nm laser and imaged at 570–620 nm and at 665–730 nm. Measurements were performed at 24 °C. Coating of glass slides consisted of a silanizing step with dichlorodimethylsilane following a PEGylation step with 1% Pluronic acid. All experiments were performed in triplicate (N = 3).

Image analysis. ImageJ's (2.0.0) preinstalled "analyse particles" package was used to analyze the number, the circumference, and fluorescence intensity of droplets under the assumption that the particles were perfectly spherical. The acquired data were then binned in 5-min bins in Excel (v16.16.24). Thus, each data point corresponds to five images (e.g., 1–5 min).

Protocol for measuring the fluorescence intensity of the Broccoli-DFHB1T complex. After the addition of 10 mM EDC (total volume = 150 µL) into a cuvette containing a mixture of peptide, poly-U, 1.5 µM Broccoli aptamer, 20 µM DFHB1T, 2 mM MgCl₂, and 30 mM KCl in MES buffer at standard conditions, the fluorescence of the sample was measured between 500 and 600 nm.

Protocol for in vitro transcription of functional RNAs. DNA templates for in vitro transcription were created by fill-in PCR using Taq-Polymerase (Promega). Briefly, two partially complementary ssDNA oligonucleotides were annealed and extended resulting in double-stranded DNA templates, which contained a 5′-terminal T7 promoter and the downstream transcription templates of interest. Following fill-in PCR, all dsDNA products were purified using the Monarch PCR & DNA Cleanup Kit (NEB). RNAs were synthesized by run-off transcription using the MEGAshortscript T7 Transcription Kit (Thermo Scientific). After column purification (Monarch RNA Cleanup Kit, NEB), RNAs were tagged with Cy5 fluorophore by ligating a RNA-pentamer modified with a 5′ phosphate and 3′ Cy5 using T4 RNA ligase 2 in the presence complementary DNA splint to the 3′-terminal 15 nucleotides of the RNA product. The ligated RNAs were then gel-purified after PAGE. The resulting RNA pellet after ethanol precipitation was suspended in ddH₂O and quantified on a Nanodrop measuring absorbance at 260 nm using their specific extinction coefficient calculated using OligoCalc (v3.27) (http://biotools.nubic.northwestern.edu/OligoCalc.html).

Reporting summary. Further information on research design is available in the Nature Research Reporting Summary linked to this article.

Data availability

Source data are provided with this paper. Data is available upon request from the corresponding author. Source data are provided with this paper.

References

1. Gomes, E. & Shorter, J. The molecular language of membraneless organelles. *J. Biol. Chem.* **294**, 7115–7127 (2019).
2. Polymenidou, M. The RNA face of phase separation. *Science* **360**, 859–860 (2018).
3. Plys, A. J. & Kingston, R. E. Dynamic condensates activate transcription. *Science* **361**, 329–330 (2018).
4. Shin, Y. & Brangwynne, C. P. Liquid phase condensation in cell physiology and disease. *Science* **357**, eaaf4382 (2017).
5. Banani, S. F., Lee, H. O., Hyman, A. A. & Rosen, M. K. Biomolecular condensates: organizers of cellular biochemistry. *Nat. Rev. Mol. Cell Biol.* **18**, 285–298 (2017).
6. Maharana, S. et al. RNA buffers the phase separation behavior of prion-like RNA binding proteins. *Science* **360**, 918–921 (2018).
7. Uversky, V. N., Kuznetsova, I. M., Turoverov, K. K. & Zaslavsky, B. Intrinsically disordered proteins as crucial constituents of cellular aqueous two phase systems and coacervates. *FEBS Lett.* **589**, 15–22 (2015).
8. Brangwynne, C. P., Mitchison, T. J. & Hyman, A. A. Active liquid-like behavior of nucleoli determines their size and shape in Xenopus laevis oocytes. *Proc. Natl Acad. Sci. USA* **108**, 4334–4339 (2011).
9. Brangwynne, C. P. et al. Germline P granules are liquid droplets that localize by controlled dissolution/condensation. *Science* **324**, 1729–1732 (2009).
10. Rai, A. K., Chen, J.-X., Selbach, M. & Pelkmans, L. Kinase-controlled phase transition of membraneless organelles in mitosis. *Nature* **559**, 211–216 (2018).
11. Koga, S., Williams, D. S., Perriman, A. W. & Mann, S. Peptide–nucleotide microdroplets as a step towards a membrane-free protocell model. *Nat. Chem.* **3**, 720–724 (2011).
12. Drobot, B. et al. Compartmentalised RNA catalysis in membrane-free coacervate protocells. *Nat. Commun.* **9**, 3643 (2018).
13. Poudyal, R. R. et al. Template-directed RNA polymerization and enhanced ribozyme catalysis inside membraneless compartments formed by coacervates. *Nat. Commun.* **10**, 490 (2019).
14. Schmitt, C. & Turgeon, S. L. Protein/polysaccharide complexes and coacervates in food systems. *Adv. Colloid Interface Sci.* **167**, 63–70 (2011).
15. Gucht, J., van der, Spruijt, E., Lemmers, M. & Cohen Stuart, M. A. Polyelectrolyte complexes: bulk phases and colloidal systems. *J. Colloid Interface Sci.* **361**, 407–422 (2011).
16. Sing, C. E. Development of the modern theory of polymeric complex coacervation. *Adv. Colloid Interface Sci.* **239**, 2–16 (2017).
17. Vieregg, J. R. et al. Oligonucleotide–peptide complexes: phase control by hybridization. *J. Am. Chem. Soc.* **140**, 1632–1638 (2018).
18. Sing, C. E. & Perry, S. L. Recent progress in the science of complex coacervation. *Soft Matter* **16**, 2885–2914 (2020).
19. Aumiller, W. M., Pir Cakmak, F., Davis, B. W. & Keating, C. D. RNA-based coacervates as a model for membraneless organelles: formation, properties, and interfacial liposome assembly. *Langmuir* **32**, 10042–10053 (2016).
20. Nakashima, K. K., Vibhute, M. A. & Spruijt, E. Biomolecular chemistry in liquid phase separated compartments. *Front. Mol. Biosci.* **6**, 21 (2019).
21. Cingil, H. E., Meertens, N. C. H. & Voets, I. K. Temporally programmed disassembly and reassembly of C3Ms. *Small* **14**, 1802089 (2018).
22. Banerjee, P. R., Milin, A. N., Moosa, M. M., Onuchic, P. L. & Deniz, A. A. Reentrant phase transition drives dynamic substructure formation in ribonucleoprotein droplets. *Angew. Chem. Int. Ed.* **56**, 11354–11359 (2017).
23. Martin, N. et al. Photoswitchable phase separation and oligonucleotide trafficking in DNA coacervate microdroplets. *Angew. Chem. Int. Ed.* **58**, 14594–14598 (2019).
24. Nakashima, K. K., Baaij, J. F. & Spruijt, E. Reversible generation of coacervate droplets in an enzymatic network. *Soft Matter* **14**, 361–367 (2018).
25. Aumiller, W. M. & Keating, C. D. Phosphorylation-mediated RNA/peptide complex coacervation as a model for intracellular liquid organelles. *Nat. Chem.* **8**, 129–137 (2016).
26. Semenov, S. N. et al. Rational design of functional and tunable oscillating enzymatic networks. *Nat. Chem.* **7**, 160–165 (2015).
27. Epstein, I. R. & Xu, B. Reaction–diffusion processes at the nano- and microscales. *Nat. Nanotechnol.* **11**, 312–319 (2016).
28. Grzybowski, B. A. & Huck, W. T. S. The nanotechnology of life-inspired systems. *Nat. Nanotechnol.* **11**, 585–592 (2016).
29. Zwicker, D., Seyboldt, R., Weber, C. A., Hyman, A. A. & Jülicher, F. Growth and division of active droplets provides a model for protocells. *Nat. Phys.* **13**, 408–413 (2017).
30. Seyboldt, R. & Jülicher, F. Role of hydrodynamic flows in chemically driven droplet division. *New J. Phys.* **20**, 105010 (2018).
31. van Rossum, S. A. P., Tena-Solsona, M., van Esch, J. H., Eelkema, R. & Boekhoven, J. Dissipative out-of-equilibrium assembly of man-made supramolecular materials. *Chem. Soc. Rev.* **46**, 5519–5535 (2017).
32. Sorrenti, A., Leira-Iglesias, J., Markvoort, A. J., de Greef, T. F. A. & Hermans, T. M. Non-equilibrium supramolecular polymerization. *Chem. Soc. Rev.* **46**, 5476–5490 (2017).
33. De, S. & Klajn, R. Dissipative self-assembly driven by the consumption of chemical fuels. *Adv. Mater.* **30**, 1706750 (2018).
34. Ragazzon, G. & Prins, L. J. Energy consumption in chemical fuel-driven self-assembly. *Nat. Nanotechnol.* **13**, 882–889 (2018).
35. de Jong, J. J. D. et al. Light-driven dynamic pattern formation. *Angew. Chem. Int. Ed.* **44**, 2373–2376 (2005).
36. Boekhoven, J. et al. Dissipative self-assembly of a molecular gelator by using a chemical fuel. *Angew. Chem. Int. Ed.* **49**, 4825–4828 (2010).
37. Boekhoven, J., Hendriksen, W. E., Koper, G. J. M., Eelkema, R. & van Esch, J. H. Transient assembly of active materials fueled by a chemical reaction. *Science* **349**, 1075–1079 (2015).
38. Leira-Iglesias, J., Sorrenti, A., Sato, A., Dunne, P. A. & Hermans, T. M. Supramolecular pathway selection of perylenediimides mediated by chemical fuels. *Chem. Commun.* **52**, 9009–9012 (2016).
39. Sorrenti, A., Leira-Iglesias, J., Sato, A. & Hermans, T. M. Non-equilibrium steady states in supramolecular polymerization. *Nat. Commun.* **8**, 15899 (2017).
40. te Brinke, E. et al. Dissipative adaptation in driven self-assembly leading to self-dividing fibrils. *Nat. Nanotechnol.* **13**, 849–855 (2018).
41. Maiti, S., Fortunati, I., Ferrante, C., Scrimin, P. & Prins, L. J. Dissipative self-assembly of vesicular nanoreactors. *Nat. Chem.* **8**, 725–731 (2016).
42. Wanzke, C. et al. Dynamic vesicles formed by dissipative self-assembly. *ChemSystemsChem* **2**, e1900044 (2020).
43. Morrow, S. M., Colomer, I. & Fletcher, S. P. A chemically fuelled self-replicator. *Nat. Commun.* **10**, 1011 (2019).
44. Mascotti, D. P. & Lohman, T. M. Thermodynamics of oligoarginines binding to RNA and DNA †. *Biochemistry* **36**, 7272–7279 (1997).
45. Szer, W. Effect of poly amines on the secondary structure of synthetic polyribonucleotides. *Ann. N. Y. Acad. Sci.* **171**, 801–809 (1970).
46. Tena-Solsona, M. et al. Non-equilibrium dissipative supramolecular materials with a tunable lifetime. *Nat. Commun.* **8**, 15895 (2017).
47. Tena-Solsona, M., Wanzke, C., Riess, B., Bausch, A. R. & Boekhoven, J. Self-selection of dissipative assemblies driven by primitive chemical reaction networks. *Nat. Commun.* **9**, 2044 (2018).
48. Rieß, B. et al. Dissipative assemblies that inhibit their deactivation. *Soft Matter* **14**, 4852–4859 (2018).
49. Kariyawasam, L. S. & Hartley, C. S. Dissipative assembly of aqueous carboxylic acid anhydrides fueled by carbodiimides. *J. Am. Chem. Soc.* **139**, 11949–11955 (2017).
50. Thandapani, P., O'Connor, T. R., Bailey, T. L. & Richard, S. Defining the RGG/RG motif. *Mol. Cell* **50**, 613–623 (2013).
51. Updike, D. L., Hachey, S. J., Kreher, J. & Strome, S. P granules extend the nuclear pore complex environment in the *C. elegans* germ line. *J. Cell Biol.* **192**, 939–948 (2011).
52. Elbaum-Garfinkle, S. et al. The disordered P granule protein LAF-1 drives phase separation into droplets with tunable viscosity and dynamics. *Proc. Natl Acad. Sci. USA* **112**, 7189–7194 (2015).
53. Grötsch, R. K. et al. Pathway dependence in the fuel-driven dissipative self-assembly of nanoparticles. *J. Am. Chem. Soc.* **141**, 9872–9878 (2019).
54. Vieregg, J. R. & Tang, T.-Y. D. Polynucleotides in cellular mimics: coacervates and lipid vesicles. *Curr. Opin. Colloid Interface Sci.* **26**, 50–57 (2016).
55. Schmidt, H. B. & Rohatgi, R. In vivo formation of vacuolated multi-phase compartments lacking membranes. *Cell Rep.* **16**, 1228–1236 (2016).
56. Dzieciol, A. J. & Mann, S. Designs for life: protocell models in the laboratory. *Chem. Soc. Rev.* **41**, 79–85 (2012).
57. Doudna, J. A., Usman, N. & Szostak, J. W. Ribozyme-catalyzed primer extension by trinucleotides: a model for the RNA-catalyzed replication of RNA. *Biochemistry* **32**, 2111–2115 (1993).
58. Filonov, G. S., Kam, C. W., Song, W. & Jaffrey, S. R. In-gel imaging of rna processing using broccoli reveals optimal aptamer expression strategies. *Chem. Biol.* **22**, 649–660 (2015).
59. Schnitter, F. & Boekhoven, J. A method to quench carbodiimide-fueled self-assembly. *ChemSystemsChem* https://doi.org/10.1002/syst.202000037 (2020).

45

Author contributions
J.B. and C.D. conceived the research and wrote the manuscript. J.B., C.D., M.T.S., Mic.S.,
and H.M. designed the experiments. C.D., F.S., Mar.S., B.A.K.K., F.S., M.T.S., H-S.K., E.S.,
and J.B. performed experiments and analyzed the data.

Competing interests
The authors declare no competing interests.

Additional information
Supplementary information is available for this paper at https://doi.org/10.1038/s41467-
020-18815-9.

Correspondence and requests for materials should be addressed to J.B.

Peer review information *Nature Communications* thanks the anonymous reviewers for
their contribution to the peer review of this work. Peer review reports are available.

Reprints and permission information is available at http://www.nature.com/reprints

Publisher's note Springer Nature remains neutral with regard to jurisdictional claims in
published maps and institutional affiliations.

46

Supporting Information for:

Active coacervate droplets as a model for membraneless organelles and pro-tocells

Donau et al.

1

**Supplementary Note 1:** Determining anhydride formation.

The anhydride concentration could not be tracked via HPLC (intrinsic instability, peak overlap with precursor and low yield). Instead, an indirect quantification was used. Briefly, we reacted the anhydride with benzylamine at different time points (eg: 2, 4, … minutes) in the reaction cycle. Then, we measured the concentration of amide by HPLC. The addition of benzylamine is also stopping the formation of new anhydride because of the sudden raise in pH. A more detailed description of the quenching method will be published soon.
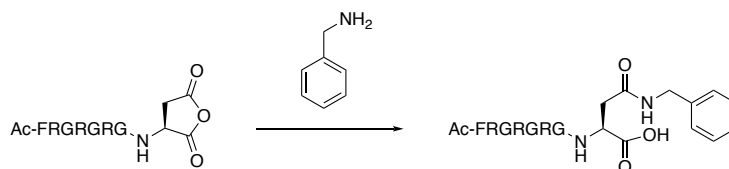
Supplementary Figure 1: Reaction scheme of the benzylamine quench.

To calculate the anhydride concentration from the benzylamine quenching method, it was approximated that abs_{220nm} (mono-amide) is the sum of abs_{220nm} (Ac-FRGRGRGD-OH) and abs_{220nm} (benzylamine). After calibration of benzylamine and Ac-FRGRGRGD-OH, we correlated the obtained integrals from the HPLC to [anhydride] and plotted the resulting concentration over time.

2

Supplementary Note 2: Full reaction scheme and all reaction described in the kinetic model.
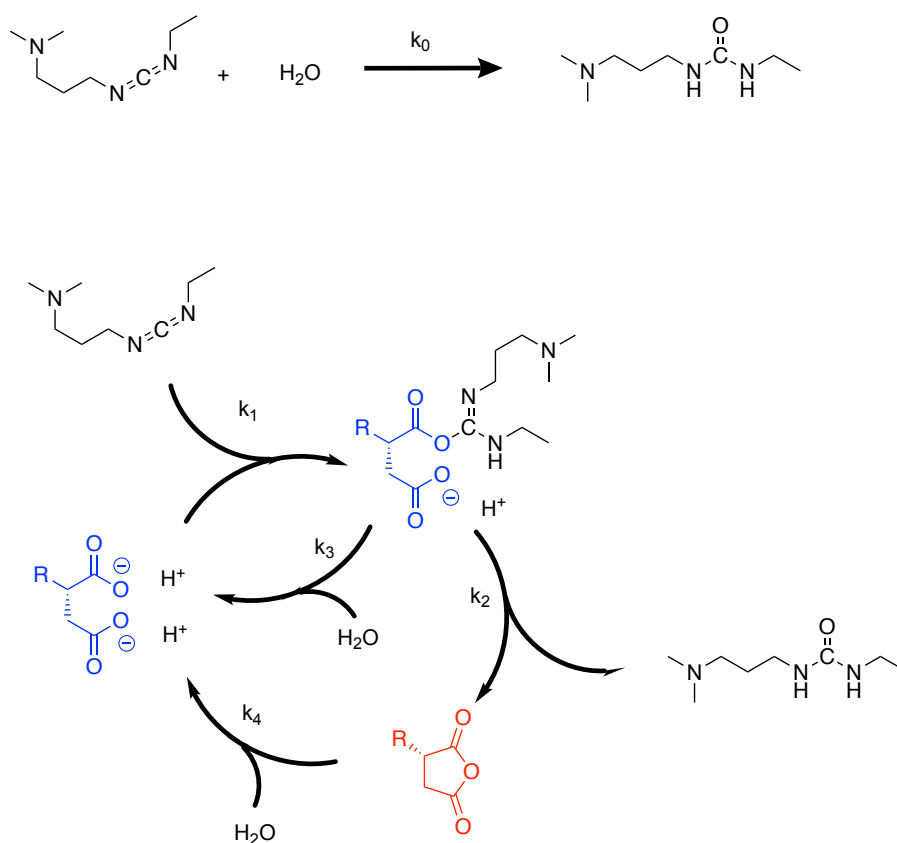
Supplementary Figure 2: All reactions taking place simultaneously in our reaction cycle.

The rate constants (k) refer to the rate constants used in our reaction model. kinetic model was written using Matlab in which the reactions below were described. The concentrations of each reactant were calculated for every second in the cycle.

Reaction 0 (k₀)

The direct hydrolysis of carbodiimide with a first order rate constant was set to 0. As this reaction is so slow in comparison to Reaction 1 (see below), it is irrelevant in the experiments. The consumption of EDC by poly(U) is neglectable.

Reaction 1 (k₁)

Formation of O-acylisourea by reaction with EDC. The rate constant was determined for the precursor by HPLC, by monitoring the EDC consumption.

Reaction 2 (k_2)

Formation of anhydride with a first order rate constant. This rate constant could not be determined because the O-acylisourea was never observed. It was set to be twice the rate of k_1.

Reaction 3 (k_3)

Direct hydrolysis of O-acylisourea (unwanted side reaction). This reaction rate could not be obtained because the O-acylisourea was not observed and so k_3 was set to zero times the rate of k_1.

Reaction 4 (k_4)

Hydrolysis of anhydride proceeded with a (pseudo)-first order rate as determined by HPLC.

4

Supplementary Table 1: Other peptide sequences synthesized for coacervation with poly-U.

Peptide sequence	Observation	Explanation
Fmoc-RGRGD-OH	EDC-induced turbidity, resulting in precipitation. No refueling possible.	*EDC-induced precipitation results in loss of peptide in solution.*
Fmoc-RGRGRGD-OH	Turbidity induced without EDC. Needed salt to inhibit turbidity. With additional salt, two EDC-induced cycles were possible, but precipitation occurred.	*Fmoc-group and three Rs interact too strongly with RNA. Additional salt weakens the electrostatic interactions. EDC-induced precipitation results in loss of peptide in solution.*
Ac-RRD-OH	No turbidity with low [peptide] and high [EDC].	*Two Rs interact too weakly with RNA.*
Ac-RRRD-OH	Precipitation for low [peptide] and high [EDC].	*Not trackable via HPLC since precursor peak overlaps with EDC.*
Ac-FRRRGD-OH	Due to precipitation only 2-3 reversible cycles possible.	*Three Rs interact too strongly with RNA.*
Ac-FRRGD-OH	Turbidity evolution very slow and not following our reaction kinetics.	*Two Rs interact too weakly with RNA, and only limited contribution of F.*
Ac-FRGRGD-OH	No turbidity with high [EDC] at high [peptide].	*Two spaced Rs interact too weakly with RNA.*
Ac-FHHHGD-OH	Due to precipitation no refueling with EDC possible.	*EDC-induced turbidity results in loss of peptide.*
Ac-FKGKGKGD-OH	In presence of EDC, irreversible consumption of precursor.	*Amino group of K reacts with EDC.*

5

52

Supplementary Table 2: Rate constants used to fit the HPLC data with the kinetic model (see methods).

k_1	k_2	k_3	k_4
O-acylurea formation	Anhydride formation	O-acylurea hydrolysis	Anhydride hydrolysis
0.075 (M^{-1} x s^{-1})	0.150 (s^{-1})	0.000 (s^{-1})	0.018 (s^{-1})

Supplementary Table 3: Partitioning coefficients of functional RNA in dynamic droplets, 5 minutes after fuel addition.

RNA	*Hammerhead*	*SunY*	*Broccoli*
Nucleotides (nr)	44	187	113
Structure	Folded	Folded	Folded
Partitioning	13	37	22

Standard conditions with 27 mM EDC and 0.1-0.2 µM of the respective fluorescently tagged (Cy-dyes) RNA.

6

Supplementary Table 4: DNA primers used in this work. The bold sequence in the T7 promoter and clamp primer is complementary to the underlined sequence in the rest of the primers.

Primer	Sequence (5' to 3')
T7 Promoter and Clamp	GATCGATCTCGCCCGC**GAAATTAATACGACTCACTATA**
F30 Broccoli	TTGCCATGAATGATCCCGAAGGATCATCAGAGTATGTGG- GAGCCCACACTCTACTCGACAGATACGAATATC TGGACCCGACCGTCTCCCACATACACATGGCAACCC <u>TATAGTGAGTCGTATTAATTTC</u>
Hammerhead	TGTGCCTTTCGTCCTCACGGACTCATCAGTTCAGCTCCC<u>TATAGTGAGTCG- TATTAATTTC</u>
SunY	GATCCTGCATGTCACCATGCAGTTCAGACTATATCTTCAACTCTTAGAG TTGTCTGCCGTTTCGGGTCGCTTGACCCTACTCCCTTACATTCATCAGGATAG TCGTTAGGCATTTACAGCTACTGCTGATTTAGCACGGGATTGACTCAGTGAGTGT TTCCCCGTTTAGGCAGATTTTCCC<u>TATAGTGAGTCGTATTAATTTC</u>

Supplementary Table 5: RNA sequences used in this work. The * indicates the ligation junction between the RNA and the Cy5-tagged pentamer.

| RNA	Sequence (5' to 3')
Hammerhead	GGGAGCUGAACUGAUGAGUCCGUGAGGACGAAAGGCACA*CACAU-Cy5
F30 Broccoli	GGGUUGCCAUGUGUAUGUGGGAGACGGUCGGGUCCAGAUAUUCGUAUCUGUCGA GUAGAGUGUGGGCUCCCACAUACUCUGAUGAUCCUUCGG- GAUCAUUCAUGGCAA*CACAU-Cy5
SunY	GGGAAAAUCUGCCUAAACGGGGAAACACUCACUGAGUCAAUCCCGUG CUAAAUCAGCAGUAGCUGUAAAUGCCUAACGACUAUCCCUGAUGAAUGUAAGGG AGUAGGGUCAAGCGACCCGAAACGGCAGACAACUCUAAGAGUUGAAGA UAUAGUCUGAACUGCAUGGUGACAUGCAGGAUC*CACAU-Cy5
Cy5-Tag	CACAU-Cy5

Supplementary Table 6: Splints used in this work.

Splint	Sequence (5' to 3')
Hammerhead	<u>ATGTG</u>TGTGCCTTTC
F30 Broccoli	<u>ATGTG</u>TTGCCATGAA
SunY	<u>ATGTG</u>GATCCTGCAT

$$\Delta G = -3.48 \pm 0.2 \text{ kcal/mol}$$
$$K_D = 2.9 \pm 0.8 \text{ mM}$$
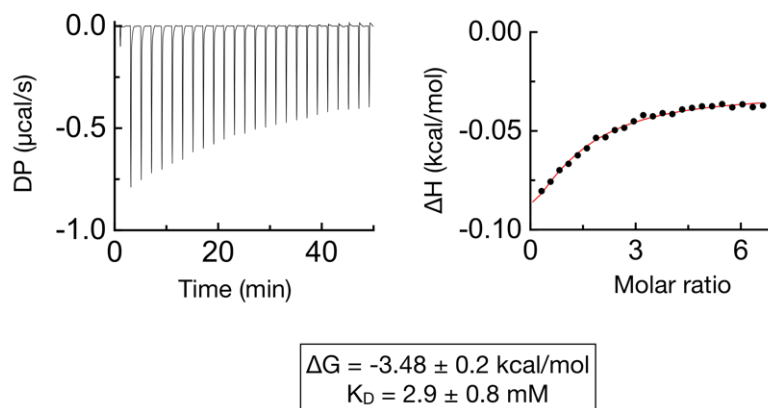
Supplementary Figure 3: Differential power and change in enthalpy measured by ITC for the interaction between precursor and RNA (poly-U). The resulting data (blank subtracted) were fitted assuming a 1:1 stoichiometry. Errors show the standard deviation from the average (N=3). For conditions, see methods.
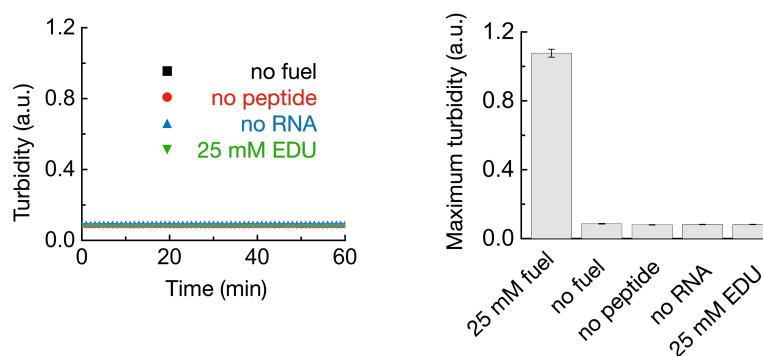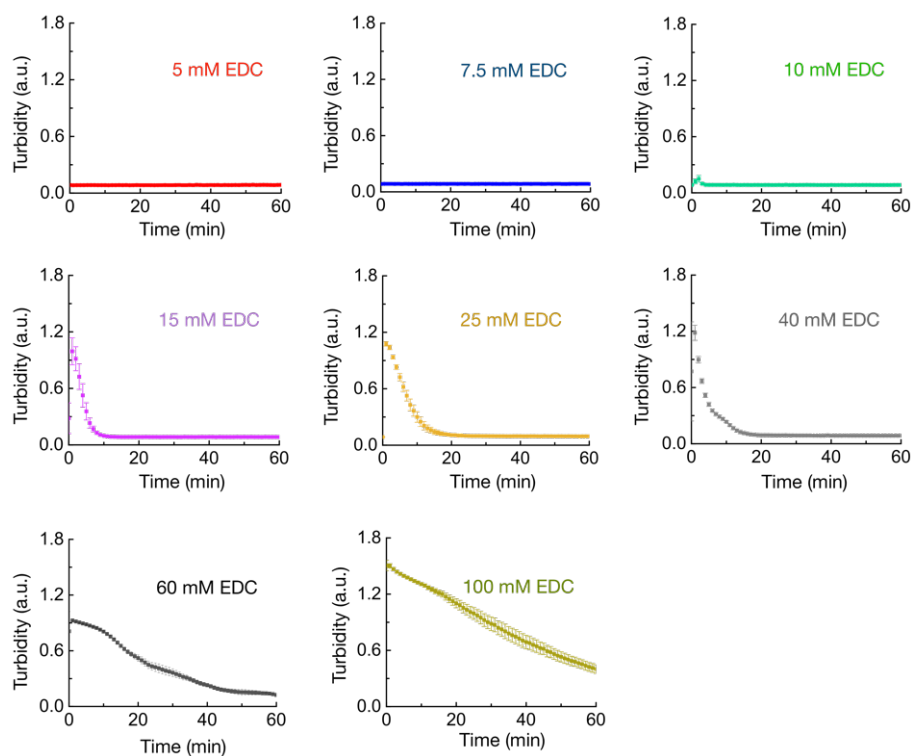

Supplementary Figure 4: Absorbance of 600 nm of light as a measure for turbidity of control experiments (not blank subtracted) at standard conditions. All error bars show the standard deviation from the average (N=3). We performed control experiments to demonstrate that our droplets are fuel-driven. When we added fuel to the same solution but either without RNA or without peptide, no turbidity was observed. Addition of a batch of waste as opposed to fuel also did not induce turbidity. The latter controls demonstrate that the droplets and their transient turbidity are a result of the fuel, RNA and peptide combined.

8
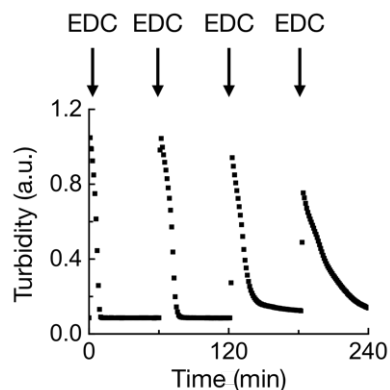
Supplementary Figure 5: Absorbance of 600 nm of light as a measure for the refueling of the chemical reaction network with additional batches of fuel (not blank subtracted). Standard conditions with 15 mM EDC. Re-addition of a batch of fuel triggers coacervation with similar turbidity and lifetime. However, after the second cycle, the system shows fatigue leading to lower turbidity and longer lifetimes. This observation can be attributed to the urea waste (EDU) which is accumulated during the cycle because of the consumption of EDC. EDU is known to screen charges of low molecular weight compounds and macromolecules which affects coacervation.
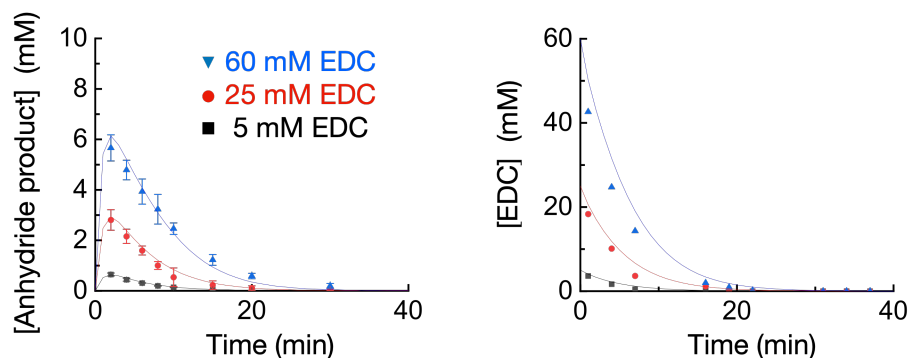
Supplementary Figure 6: Anhydride product and EDC concentrations from HPLC experiments. Standard conditions with 5 mM EDC (no droplets), 25 mM EDC (dynamic droplets) and 60 mM EDC (metastable droplets). All error bars show the standard deviation from the average (N=3). EDC traces are not in triplicates but from 3 different samples (1-16-31 min, 4-19-34 min, 7-22-37 min). Lines represent fitting plots from our kinetic model.

9

Supplementary Figure 7: Absorbance of 600 nm of light as a measure for turbidity for standard conditions with 4.1 mM poly-U and various fuel concentrations. Threshold value for dynamic droplets: absorbance < 0.1 a.u. (without blank subtraction) after 30 min. All error bars show the standard deviation from the average (N=3).

10
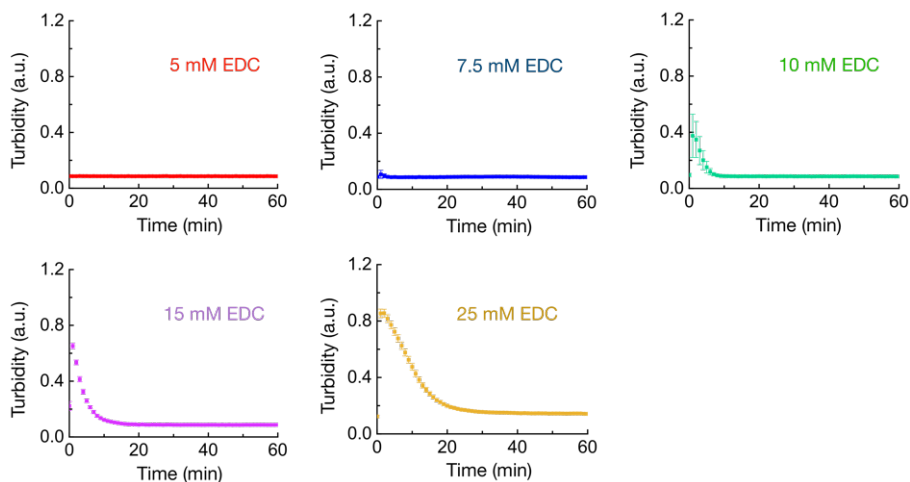
Supplementary Figure 8: Absorbance of 600 nm of light as a measure for turbidity for standard conditions with 1.4 mM poly-U and various fuel concentrations. Threshold value for dynamic droplets: absorbance < 0.1 a.u. (without blank subtraction) after 30 min. All error bars show the standard deviation from the average (N=3).
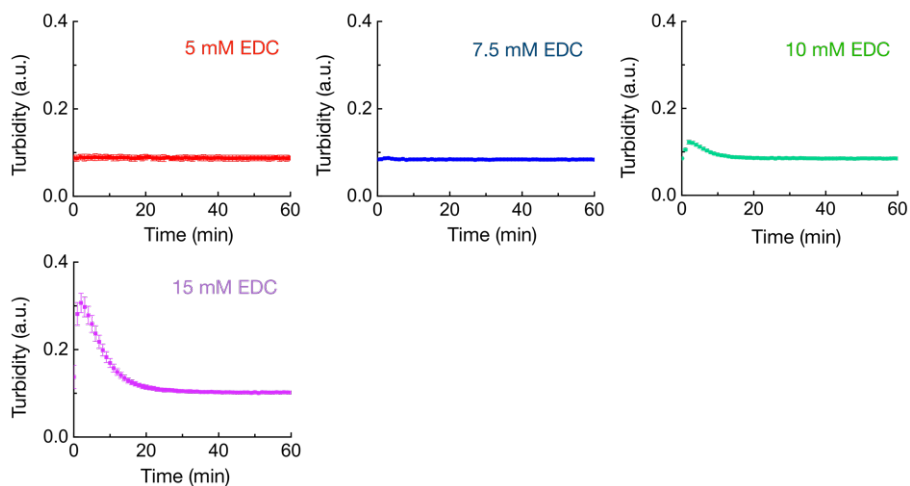
Supplementary Figure 9: Absorbance of 600 nm of light as a measure for turbidity for standard conditions with 0.3 mM poly-U and various fuel concentrations. Threshold value for dynamic droplets: absorbance < 0.1 a.u. (without blank subtraction) after 30 min. All error bars show the standard deviation from the average (N=3).

11
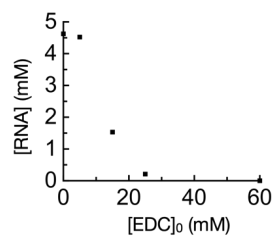
Supplementary Figure 10: Poly-U (RNA) concentration in the supernatant after centrifugation. 2 minutes after EDC addition. Standard conditions with various fuel concentrations.

12
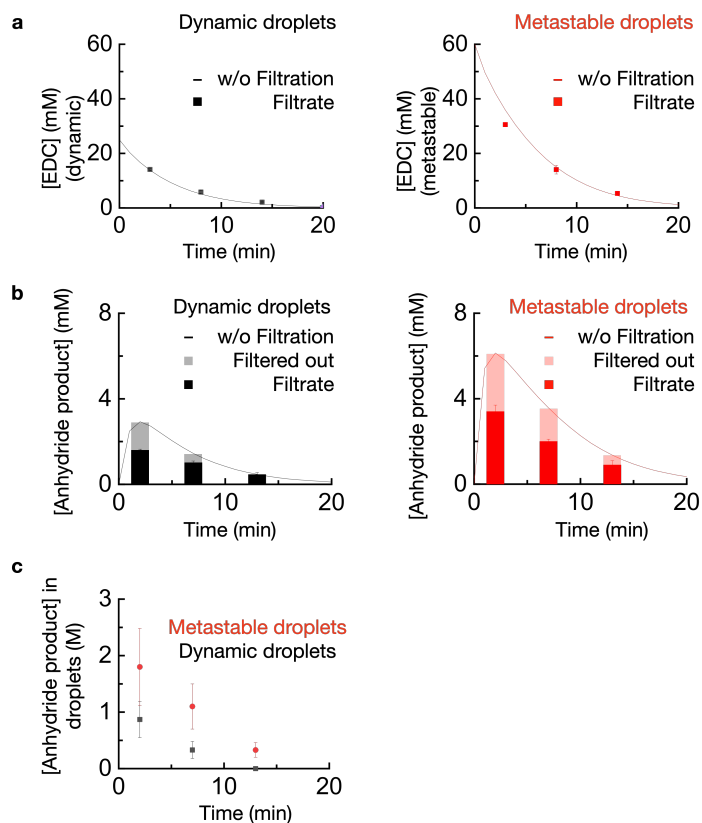
Supplementary Figure 11: EDC and anhydride product concentrations in the supernatant after filtration. **a-b**, EDC concentration (a) and anhydride product concentration (b) in the supernatant for dynamic (black) and metastable (red) droplets. **c**, Concentration of anhydride product in the droplet phase. Droplet volumes were estimated to be 0.3 ± 0.1 µL in a 200 µL sample (0.15 %). All error bars show the standard deviation from the average (N=3). Lines (w/o filtration) represent fitting plots from the kinetic model for the total amount of EDC and anhydride.
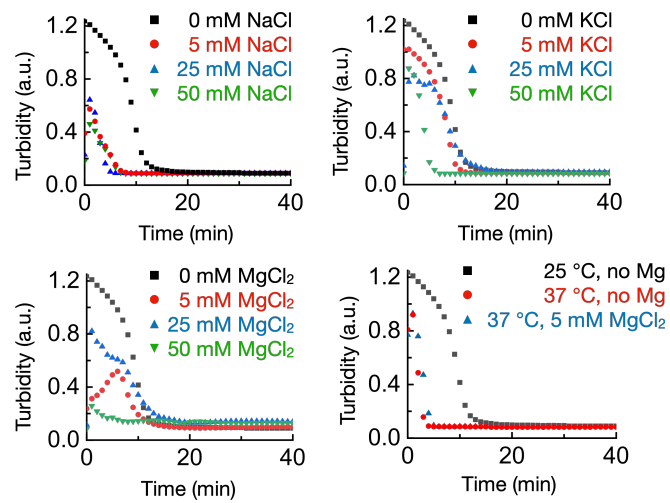
Supplementary Figure 12: Absorbance of 600 nm of light as a measure for turbidity for standard conditions and various salt concentrations or temperature.

14

Chapter 6

Phase transitions in chemically fueled, multiphase complex coacervate droplets

In this chapter, I wanted to study how chemical reactions can regulate the internal hierarchy of droplets. For that, I used the droplet model from chapter 5 in the presence of a second polyanion in solution, *i.e.*, a synthetic polymer. The two polyanions compete for the activated peptide, resulting in droplets with or without subcompartmentization leading to distinct regimes inside the phase diagram. I identify new transitions that can only occur under kinetic control. Finally, the liquidity of the droplets is controlled by the chemical reaction cycle, similar to active cellular processes regulating membraneless organelles. I demonstrate that not only thermodynamic properties but also kinetics should be considered in the organization of multiple phases in droplets.

This work has been published:

Title: Phase Transitions in Chemically Fueled, Multiphase Complex Coacervate Droplets

Authors: Carsten Donau, Fabian Späth, Michele Stasi, Alexander M. Bergmann and Job Boekhoven

First published: 6th of September 2022

Journal: *Angewandte Chemie International Edition* **2022**, e202211905

Publisher: Wiley-VCH GmbH

DOI: https://doi.org/10.1002/anie.202211905

Reprinted with permission from Wiley-VCH GmbH.

Contribution of the authors: C. Donau and J. Boekhoven conceived the research, designed the experiments, and wrote the manuscript. C. Donau, F. Späth, M. Stasi, A. M. Bergmann, and J. Boekhoven performed experiments and analyzed the data.

GDCh

Research Articles

Angewandte
Chemie
International Edition
www.angewandte.org

Self-Assembly | Hot Paper

Phase Transitions in Chemically Fueled, Multiphase Complex Coacervate Droplets

Carsten Donau, Fabian Späth, Michele Stasi, Alexander M. Bergmann, and Job Boekhoven*

Abstract: Membraneless organelles are droplets in the cytosol that are regulated by chemical reactions. Increasing studies suggest that they are internally organized. However, how these subcompartments are regulated remains elusive. Herein, we describe a complex coacervate-based model composed of two polyanions and a short peptide. With a chemical reaction cycle, we control the affinity of the peptide for the polyelectrolytes leading to distinct regimes inside the phase diagram. We study the transitions from one regime to another and identify new transitions that can only occur under kinetic control. Finally, we show that the chemical reaction cycle controls the liquidity of the droplets offering insights into how active processes inside cells play an important role in tuning the liquid state of membraneless organelles. Our work demonstrates that not only thermodynamic properties but also kinetics should be considered in the organization of multiple phases in droplets.

Introduction

Membraneless organelles have emerged as a major part of the intracellular organization.[1–3] They assemble through liquid-liquid phase separation of a dense protein and RNA-rich phase in the cytosol where they perform a plethora of cellular functions like modulating enzymatic activity, buffering noise in protein concentrations, or influencing signaling pathways.[4,5] Increasing evidence suggests that some membraneless organelles are not homogeneous but instead have subcompartments that further separate components through different partitioning between the phases.[6–11] Furthermore, many membraneless organelles are active compartments that are regulated by chemical reactions, i.e., they are kinetically controlled under conditions away from equilibrium.[5,12–22] Chemical reactions may change their

liquid-like property[3,5,15,23,24] and malfunction has been linked to disease.[25–28] However, how exactly chemical reactions regulate membraneless organelles, and the connection between molecular design and their emergent properties remains elusive.[2,13,17,25]

Synthetic coacervate droplets have proven to be a powerful model for membraneless organelles.[29–34] These droplets form through attractive interactions between polymers via ion-pairing and other supramolecular effects to give membraneless droplets with liquid-like properties.[33,35] Recently, it was shown that coacervate droplets with subcompartments can also be formed[36–41] which rely on differences in surface tension between the respective phases,[37] similar to membraneless organelles.[6] However, kinetically controlled multiphase droplets are rare.[42] Such models are powerful to explore mechanisms by which chemical reactions regulate phase transitions, internal droplet hierarchy, and droplet properties. In this work, we thus set out to understand the mechanisms by which chemical reactions can regulate the internal hierarchy of multiphase coacervate droplets. We use a chemical reaction cycle that regulates the affinity of a peptide for polyelectrolytes as a model for post-translational modifications, e.g., protein phosphorylation, acetylation, or methylation, to regulate their ability to phase separate. By combining the peptide with two polyelectrolytes we create a system without droplets at equilibrium, or where droplets are formed with or without sub-compartmentalization depending on how far the system is brought out of equilibrium. We study in detail the transitions from one regime to another and identify new transition states that are not observed under thermodynamic control. Finally, we show that the chemical reaction cycle controls the liquidity of the droplets yielding insights into how active processes inside cells play an important role in tuning the liquid state of membraneless organelles. Our work demonstrates that not only thermodynamic properties but also kinetics should be considered in the organization of multiple phases in droplets.

[*] C. Donau, F. Späth, M. Stasi, A. M. Bergmann, Prof. J. Boekhoven
Department of Chemistry,
Technical University of Munich
Lichtenbergstrasse 4, 85748 Garching (Germany)
E-mail: job.boekhoven@tum.de

Results and Discussion

To design droplets with subcompartments (multiphase droplets) regulated by chemical reactions, we first screened for the conditions that resulted in multiphase droplets close to equilibrium, i.e., droplets that are not actively maintained by chemical reactions. We refer to these as passive droplets (Figure 1a). We used a small cationic peptide (peptide 1) and combined it with two polyanions, i.e., poly-U (pU, 600–

Research Articles

Angewandte
International Edition Chemie
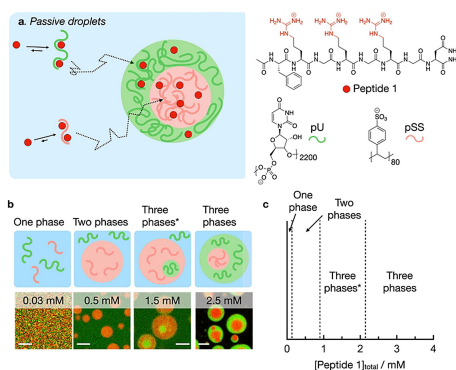
Figure 1. Multiphase droplets under thermodynamic control. a) Schematic representation of the phase separation of pU, pSS, and peptide 1. b) Schemes and respective confocal micrographs of droplets from solutions containing various concentrations of peptide 1 and 5 mM pU (expressed as monomer units), 5 mM pSS (expressed as monomer units) in 200 mM MES at pH 5.3 with 0.15 µM Cy3-A_{15}-pU (green) and 0.15 µM Cy5-pSS (red), 10 minutes after droplet formation. Scale bar: 3 µm. c) Phase diagram as a function of the total concentration of peptide 1 of solutions from (b).

1000 kDa) and polystyrene sulfonate (pSS, 17 kDa). Peptide 1 has the following structure: Ac-FRGRGRGN-NH$_2$ and it contains 1) F, i.e., phenylalanine important for aromatic interaction with the polyanions, 2) the RG repeat, i.e., arginine-glycine repeat that is known to bind polyanions and 3) an amidated N, i.e., asparagine. We chose the asparagine for this peptide, because, when mutated for aspartic acid, it makes the peptide responsive to a chemical reaction cycle which we explain below.[32,43,44]

We established the interaction strength of peptide 1 with pSS and pU individually in 200 mM MES buffer at pH 5.3 which are the conditions used throughout his work. At this pH, peptide 1 has an overall charge of +3. Isothermal titration calorimetry (ITC) showed that peptide 1 has a higher affinity for pSS compared to pU (K_D of 3.2 µM vs 130 µM, Figure S1). This result was further corroborated by turbidity measurements that we carried out using a UV/Vis spectrophotometer at 600 nm (Table S1) which showed the appearance of turbidity above a critical coacervation concentration (CCC) of 0.8 mM of peptide 1 combined with pSS (10 mM), and 1.85 mM with pU (10 mM). We also used turbidity measurements to determine the critical salt concentration, i.e., the amount of salt added required to dissolve the droplets. 1.5 M NaCl was not enough to revert to a clear solution for pSS (10 mM pSS, 2.5 mM peptide 1), while 63 mM NaCl was sufficient in the case of pU under similar conditions (Table S1). This critical salt concentration is an indirect measure of the interfacial surface tension between the droplet phase and buffer,[37] and a large difference in this value is the driving force for multiphase droplets to form. It

is therefore likely that peptide 1 will form multiphase droplets when combined with both pSS and pU.

We confirmed the presence of multiphase droplets by confocal microscopy. We used a solution of pU, pSS, peptide 1, and peptide 2. Peptide 2 is structurally very similar to peptide 1 with the amino acid sequence: Ac-FRGRGRGD-OH. The aspartic acid at the C-terminus is negatively charged, resulting in a zwitterionic peptide with an overall charge of +1. ITC experiments showed that peptide 2 has two orders of magnitude lower affinity for the two polyanions than peptide 1 (Figure S1). Thus, peptide 2 serves mostly as a molecular crowder, but we used it in later experiments to compare passive droplets with fuel-driven droplets. We ensured that the total peptide concentration was always 15 mM, i.e., [peptide 1]+[peptide 2]=15 mM. More than 0.05 mM of peptide 1 was needed to form droplets (Figure 1b and c). The addition of 0.5 mM of peptide 1 led to the formation of droplets with a diameter of a couple of micrometers that contained pSS (red color) but did not up-concentrate pU (green). Above 0.9 mM peptide 1, pU droplets started to form which settled inside the larger pSS droplets. With the addition of more peptide 1, the pU droplets grew larger and we observed multiphase droplets with a pSS core surrounded by a pU shell (2.2 mM peptide 1 or higher). This result is in line with the CSC experiments where we showed that the pSS-buffer interface has a higher surface tension compared to the pU-buffer interface. Energetically speaking, it is thus favorable to settle the pSS droplets into the core of the multiphase droplets. Between 0.9 mM and 2.2 mM peptide 1, pU droplets are not sufficiently large to surround the pSS droplets. In this case, multiphase droplets are energetically favorable where the shell is composed of the phase that has the highest interfacial surface energy with the buffer phase (Three phases*, Figure 1c).[37] Confocal micrographs with the fluorescent analog of peptide 1 showed that peptide 1 preferentially partitions into the pSS core (Figure S2) in accordance with the ITC measurements. Control experiments showed that peptide 1 partitions similarly to its fluorescent analog (Figure S3). Taken together, the peptide 1 concentration regulates whether one, two, or three phases are obtained.

To test how chemical reactions can regulate these multiphase droplets, we converted the passive, multiphase droplets into active ones. Thus, we used peptide 2 as a precursor in our previously described fuel-driven reaction cycle.[32,43,45] Peptide 2 alone cannot form droplets with pSS or pU under the employed conditions. However, the chemical reaction cycle can temporarily activate the peptide for droplet formation at the expense of a chemical fuel (Figure 2a, Figure S4). Peptide 2 (Ac-FRGRGRGD-OH) can react with 1-ethyl-3-(3-dimethylaminopropyl) carbodiimide (fuel) to convert its C-terminal aspartic acid into its cyclic anhydride state. That activated state, which we refer to as activated peptide 2, has a short half-life time of about 45 seconds before it is hydrolyzed to revert to the original peptide 2, i.e., the deactivation reaction in the cycle. Activated peptide 2, due to the loss of its two anionic carboxylates has an overall charge of +3 and is therefore
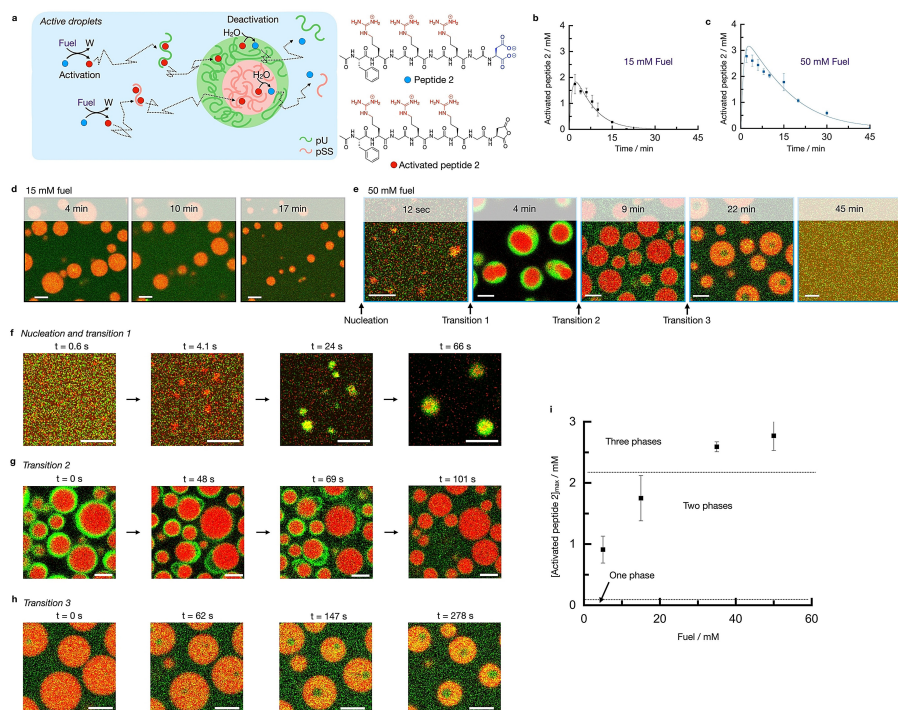
Figure 2. Phase transitions in active multiphase droplets under kinetic control. a) Schematic representation of the kinetically controlled phase separation of pU, pSS, and peptide 2. The conversion of fuel into a waste product (W) activates peptide 2 for phase separation. Activated peptide spontaneously deactivates upon reaction with water. In its finite lifetime, it complexes pU or pSS and phase separates into multiphase droplets. b–c) Concentration of activated peptide 2 as a function of time for 15 mM (b) and 50 mM (c) fuel. Solutions containing 15 mM peptide 2, 5 mM pU, 5 mM pSS, 200 mM MES at pH 5.3. The solid lines represent calculated trends by our kinetic model. d–e) Confocal micrograph time series of solutions from (b) or (c) with 0.15 μM Cy3-A_{15}-pU (green) and 0.15 μM Cy5-pSS (red). f) Confocal micrographs of the nucleation and transition 1 of solutions from (c), right after fuel addition. g–h) Confocal micrographs of transitions 2 (g) and 3 (h) of solutions from (c). i) Maximum concentration of activated peptide 2 after 2 minutes as a function of fuel concentration. Dotted lines indicate at which activated peptide 2 concentrations two or three phases are obtained. All error bars show the standard deviation from the average (N=3). Scale bar for all micrographs: 3 μm.

expected to behave like peptide 1 in the above-described passive droplets, i.e., have a high affinity for the polyanions and form multiphase droplets.

The amount of activated peptide 2 generated and for how long it remains present can be controlled by the amount of fuel added. We measured the concentrations of activated peptide 2 and fuel over time by HPLC (Figure 2b and c, Figure S5) and used that data to adjust a previously written kinetic model.[32,46] The kinetic model predicts the concentrations of all reactants and products every second after fuel is added and can be used to predict the maximum concentration of activated peptide 2 reached. For example, when 15 mM of fuel was added, the concentration of activated peptide 2 rapidly increased to just below 2 mM

after which it decayed back to 0 mM within 20 minutes (Figure 2b). In contrast, when 50 mM fuel was added, the concentration of activated peptide 2 rapidly increased to just below 3 mM and decayed over the next 40 minutes (Figure 2c). Turbidity measurements showed that the droplet formation is following the evolution of activated peptide 2 (Figure S6).

Using confocal microscopy, we found droplets that contained pSS in the case of 15 mM fuel (Figure 2d). These droplets emerged almost immediately, grew via fusion, and dissolved after 20 minutes (Movie S1). Under those conditions, no evidence of multiphase droplets was found. In contrast, in the case of 50 mM fuel, multilayered droplets were obtained with a pSS core and a pU shell in the first

© 2022 The Authors. Angewandte Chemie International Edition published by Wiley-VCH GmbH

Research Articles

minutes (Figure 2e). Strikingly, we were able to resolve the nucleation of the pSS core and the pU shell by employing a microfluidic setup that mixes and entraps all ingredients for the complex coacervate droplets in a 40 µm-sized water droplet (Movie S2). While the pSS phase formed within a second after fuel addition, the pU shell (droplet transition 1) formed after just over 20 seconds (Figure 2f, Movie S3). We also used confocal fluorescence microscopy in the bulk solution for 50 mM fuel. After 9 minutes, we observed a droplet transition in which multiphase droplets lost their pU shell (droplet transition 2, Figure 2e). The time of the transition coincides with the concentration activated peptide 2 falling below 2 mM. The transition does not occur smoothly through the dissolution of the shell but instead, the pU phase swells and detaches from the pSS phase followed by the division of the pU phase into fragments of pU (Figure 2g, Movie S4). The fragments of the pU-based shell survive for several seconds before they eventually also dissolve.

We explain the swelling and the detaching of the pU phase by the increase in negative charges due to the continuous hydrolysis of activated peptide 2. This observation is in line with our previous work.[32] We captured the bursting of the pU shell in microfluidics as well (Movie S5).

Surprisingly, between 9 and 20 minutes, we found evidence of another unexpected transition. Where we expected the pSS droplets to dissolve, we found that the pSS droplets had suddenly obtained a pU core (droplet transition 3, Figure 2e). The pU that previously made up the shell had dissolved and reenters the droplet to form a new droplet core (Figure 2h, Movie S6). Noteworthy, we excluded that this transition is a consequence of the dehybridization of Cy3-A$_{15}$ from pU (Figure S7) (see supplementary discussion 1). This process was accompanied by droplet shrinkage until the droplets finally dissolved after more than 40 minutes. We also observed this transition in the microfluidic setup (Figure S8). This transition is surprising because the pU phase should not be stable under these concentrations of activated peptide 2 below 1 mM (see passive droplets). The observation suggests that pU plays a dual role, both as the shell and the core and its location can be regulated kinetically by the balance between activation and deactivation.

Based on the confocal microscopy data and the kinetic model, we establish a phase diagram to explain the three phase transitions (Figure 2i). We found that 0.7 mM of fuel was needed to observe pSS droplets. According to the kinetic model, that amount of fuel results in a maximum concentration of activated peptide 2 of 0.1 mM, i.e., activated peptide 2 has a CCC of 0.1 mM to form droplets with pSS, similarly to peptide 1 in passive droplets. When the concentration of activated peptide 2 was above 2.0 mM, we found multiphase droplets with a pU shell. Thus around 2.0 mM, there is a CCC for the formation of the pU shell, similarly to peptide 1 in the passive droplets. These results indicate that active droplets behave similarly to the passive droplets formed by peptide 1 in terms of their phase diagram. However, the surprising formation of a pU core at

the end of the reaction cycle (transition 3) is not explained by the phase diagram of passive or active droplets.

To explain transition 3, we propose that individual pU molecules diffuse into the core of the pSS droplet (Figure 3a). Indeed, we found pU in the pSS phase (Figure 3c) which shows fast recovery after photobleaching (FRAP, Figure S9). We propose that the driving force for pU to enter and form the multiphase core is vacuole formation. Vacuole formation in coacervate droplets is the process in which a droplet transitions into an aqueous phase surrounded by phase-separated material. Vacuolization has been linked to the build-up of osmotic pressure within the droplet and is frequently observed in droplet dissolution.[32,47–50] Thus the aqueous environment of the vacuole has a higher concentration of charges compared to the dilute phase. The increased charge serves as a driving force for the up-concentration of pU.

In our active droplets, activated peptide 2 is constantly deactivated within the droplets (Figure 3a). As the system is running low on chemical fuel, the activation that supplies the droplet with activated peptide 2 is outcompeted by the deactivation leading to droplet dissolution. As a result, a vacuole forms. We confirmed that the vacuole contains a higher concentration of peptide than the dilute phase (Figure 3b). That increased concentration of peptide attracts pU into the core of the droplet. Indeed, pU was also up-concentrated in the core compared to the phase outside of
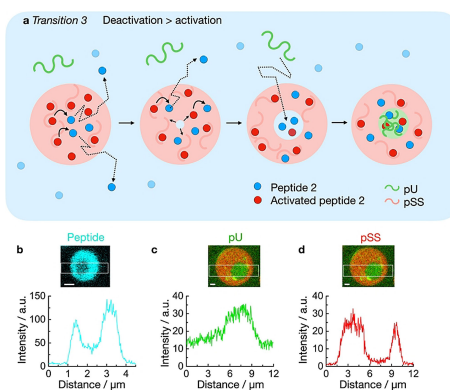

Figure 3. Mechanism of transition 3 in active droplets. a) Schematic representation of the vacuole formation of an active droplet containing pSS in presence of pU. Peptide deactivation leads to the build-up of osmotic pressure and the nucleation of a dilute phase inside the droplet which harbors elevated peptide concentrations compared to the surrounding dilute phase. The influx of pU leads to the formation of a new coacervate phase. b) Plot profile of peptide in a droplet, 20 minutes after addition of 50 mM fuel. Solutions containing 15 mM peptide 2, 5 mM pU, 5 mM pSS, 200 mM MES, pH 5.3, 1 µM NBD-GRGRGRGD-OH (blue). c–d) Plot profile of pU (c) and pSS (d) in a droplet, 20 minutes after addition of 50 mM fuel. Solutions from (b) but with 0.15 µM Cy3-A$_{15}$-pU and 0.15 µM Cy5-pSS (red) instead of NBD-peptide. Scale bar: 1 µm.

the droplets (K=3, Figure 3c) whereas the concentration of pSS was the highest in the droplet phase surrounding the vacuole (Figure 3d). Specifically, the concentration of peptide was about 89 mM in the vacuole (see methods, Table S2). We validated that 89 mM peptide 2 can create multiphase droplets even without fuel which further indicates that the vacuole is a new phase vastly different from the dilute phase outside of the droplets (Figure S10).

Noteworthy, experiments without pU showed that vacuolization is still part of the dissolution process of pSS droplets with 50 mM fuel (Movie S7). In other words, pU is not required for vacuolization. In contrast, the same experiment with only 15 mM fuel did not show the formation of vacuoles (Movie S8). In line with that, 15 mM fuel with pU did not show the formation of a pU core (see Figure 2d), which strongly indicates that vacuolization is required for transition 3.

Taken together, vacuolization is part of the dissolution process of our droplets when the system is running low on fuel. The concentration of peptide in the vacuole is vastly higher compared to the dilute phase which attracts pU (transition 3). This new phase is kinetically stabilized by the surrounding shell which is not observed for passive droplets due to the absence of a deactivation reaction. Coupling the droplet properties to a chemical reaction cycle thus allows for access to regimes in the phase diagram not possible under thermodynamic control. Excitingly, increasing studies suggest that vacuole formation occurs in membraneless organelles and related protein droplets, too.[51–57]

Membraneless organelles' subcompartments vary in chemical composition, but also vary in viscosity, diffusivity, and reactivity.[58] We performed FRAP experiments to investigate the liquidity of the phases in our kinetically regulated multiphase droplets. We used spot bleaching (r= 0.8 μm) to measure the diffusivity of peptide 2, pSS, and pU in multiphase droplets with 50 mM fuel (Figure 4a and b). We spot-bleached the pSS core and found that the diffusion of peptide 2 (0.007±0.003 μm²s⁻¹) is three to five times higher than the one of pSS which is expected based on the differences in molecular weight (Figure S11 and S12). Early in the cycle, the diffusion coefficient for both the peptide and pSS is low (Figure 4b) which implies that the droplet core is very dense right after fuel addition corresponding to a viscosity of 14.6 Pa·s; a value typical for dense coacervate droplets (see methods for calculation).[33] Since the pU shell in multiphase droplets with 50 mM fuel is too thin for FRAP experiments, we performed spot bleaching on single-phase pU droplets and assumed that their diffusivity is like the shell of the multiphase droplet (see supplementary discussion 2, Figure S13). The diffusion coefficient of peptide 2 in the pU phase is more than two orders of magnitude higher (4.0±2.5 μm²s⁻¹) compared to its diffusion in the pSS phase. Similarly, the pU diffuses four times faster in the shell compared to pSS in the core which is notable considering pU's much higher molecular weight (800 kDa vs 17 kDa). These differences in the diffusion coefficients imply that the core has a high viscosity, whereas the shell is more liquid. These findings were further corroborated by the fast fusion
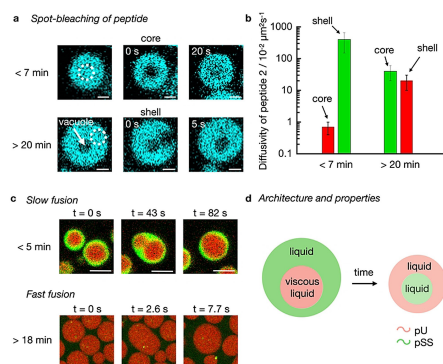
Figure 4. Diffusivity of molecules in active droplets. a) Confocal micrographs from FRAP spot bleaching experiments less than 7 or more than 20 minutes after the addition of fuel. The solutions contain 15 mM peptide 2, 5 mM pU, 5 mM pSS, 200 mM MES, pH 5.3, 1 μM NBD-GRGRGRGD-OH (cyan) with 50 mM fuel. Scale bar: 1 μm. b) Diffusivity of peptide 2 (and activated peptide 2) in the core and the shell of active multiphase droplets from (a) as a function of time. The colors indicate the pU (green) and pSS (red) phases. Error bars show the standard deviation of 6 droplets from 2 experiments (N=6). c) Confocal micrographs of fusion events from solutions of (a) with 0.15 μM Cy3-A₁₅-pU (green) and 0.15 μM Cy5-pSS (red). Scale bar: 2 μm. d) Schematic representation of active droplets with inner hierarchy. Properties of inner and outer layers change over time.

of the shell of the droplet (Movie S9 and S10), but the slow fusion of the core of the droplet (Figure 4c, Movie S10).

As the reaction cycle progressed, the diffusivity of the peptide and pSS increased drastically (Figure 4b, Figure S11 and S12) which was corroborated by fast fusion events of the pSS droplets (Figure 4c, Movie S11). At the time when the pU shell had dissolved and a vacuole has formed, the diffusivity of the peptide in the pSS phase, i.e., now the shell of the droplet, is almost two orders of magnitude higher compared to the diffusivity at the beginning of the cycle. We reason that as the levels of activated peptide 2 decrease, the droplets start to decay which leads to the efflux of molecules to give a more liquid compartment. Excitingly, we could also measure the diffusivity of the peptide in the vacuole, i.e., the newly formed pU core, and found it to be comparable to the diffusivity of the peptide in the pSS shell (Figure S14). Combined with the calculated concentrations inside the vacuole phase, we conclude that the vacuole phase is a liquid microenvironment, similar to the surrounding shell. In other words, the cycle starts with droplets with a very viscous pSS core surrounded by a liquid pU shell when fuel is abundant. These droplets transition to droplets with a liquid pU core surrounded by a liquid pSS shell when fuel is scarce (Figure 4d).

Conclusion

Our work shows that active liquid droplets can display an inner hierarchy that is regulated through chemical reactions. The employed chemical reaction cycle controls the stability, liquidity, and location of the droplet multiphases. We show that phase transitions between phase-separated states are unique to the active droplets and cannot be obtained in passive droplets under thermodynamic equilibrium. These active multiphase droplets bear similarities to their biological counterparts which often display complex architectures with liquid to solid-like cores and shells. Our droplets also transition from multilayers with an RNA shell to multilayers with an RNA core[58] which makes them a great model to elucidate mechanisms of organelle organization. Coacervate droplets have also been proposed as protocell models[59–61] and their regulation through chemical reactions might be thus relevant for the design of more complex compartments with metabolic networks.

Experimental Section

Materials and methods description and additional data are available in the Supporting Information. The methods include: Synthetic protocols; Sample preparation; Isothermal titration calorimetry; UV/Vis spectroscopy; Fluorescence spectroscopy; Confocal fluorescence microscopy; FRAP procedures; Microfluidic procedures; HPLC procedures; Kinetic model and Calculations.

Acknowledgements

Conflict of Interest

The authors declare no conflict of interest.

Data Availability Statement

The data that support the findings of this study are available from the corresponding author upon reasonable request.

[1] A. A. Hyman, C. A. Weber, F. Julicher, *Annu. Rev. Cell Dev. Biol.* **2014**, *30*, 39–58.
[2] Y. Shin, C. P. Brangwynne, *Science* **2017**, *357*, 6357.
[3] S. F. Banani, H. O. Lee, A. A. Hyman, M. K. Rosen, *Nat. Rev. Mol. Cell Biol.* **2017**, *18*, 285–298.
[4] A. S. Lyon, W. B. Peeples, M. K. Rosen, *Nat. Rev. Mol. Cell Biol.* **2021**, *22*, 215–235.
[5] M. Hondele, S. Heinrich, P. De Los Rios, K. Weis, *Emerging Top. Life Sci.* **2020**, *4*, 343–354.
[6] M. Feric, N. Vaidya, T. S. Harmon, D. M. Mitrea, L. Zhu, T. M. Richardson, R. W. Kriwacki, R. V. Pappu, C. P. Brangwynne, *Cell* **2016**, *165*, 1686–1697.
[7] S. Jain, J. R. Wheeler, R. W. Walters, A. Agrawal, A. Barsic, R. Parker, *Cell* **2016**, *164*, 487–498.
[8] J. R. Wheeler, T. Matheny, S. Jain, R. Abrisch, R. Parker, *eLife* **2016**, *5*, e18413.
[9] T. H. Kim, B. Tsang, R. M. Vernon, N. Sonenberg, L. E. Kay, J. D. Forman-Kay, *Science* **2019**, *365*, 825–829.
[10] D. W. Sanders, N. Kedersha, D. S. W. Lee, A. R. Strom, V. Drake, J. A. Riback, D. Bracha, J. M. Eeftens, A. Iwanicki, A. Wang, M. T. Wei, G. Whitney, S. M. Lyons, P. Anderson, W. M. Jacobs, P. Ivanov, C. P. Brangwynne, *Cell* **2020**, *181*, 306–324.
[11] J. R. Simon, N. J. Carroll, M. Rubinstein, A. Chilkoti, G. P. Lopez, *Nat. Chem.* **2017**, *9*, 509–515.
[12] C. P. Brangwynne, T. J. Mitchison, A. A. Hyman, *Proc. Natl. Acad. Sci. USA* **2011**, *108*, 4334–4339.
[13] C. P. Brangwynne, P. Tompa, R. V. Pappu, *Nat. Phys.* **2015**, *11*, 899–904.
[14] S. C. Weber, *Curr. Opin. Cell Biol.* **2017**, *46*, 62–71.
[15] E. Gomes, J. Shorter, *J. Biol. Chem.* **2019**, *294*, 7115–7127.
[16] T. J. Nott, E. Petsalaki, P. Farber, D. Jervis, E. Fussner, A. Plochowietz, T. D. Craggs, D. P. Bazett-Jones, T. Pawson, J. D. Forman-Kay, A. J. Baldwin, *Mol. Cell* **2015**, *57*, 936–947.
[17] J. Berry, S. C. Weber, N. Vaidya, M. Haataja, C. P. Brangwynne, *Proc. Natl. Acad. Sci. USA* **2015**, *112*, E5237–E5245.
[18] E. E. Griffin, D. J. Odde, G. Seydoux, *Cell* **2011**, *146*, 955–968.
[19] L. C. Reineke, W. C. Tsai, A. Jain, J. T. Kaelber, S. Y. Jung, R. E. Lloyd, *Mol. Cell. Biol.* **2017**, *37*, e00596-16.
[20] H. Falahati, E. Wieschaus, *Proc. Natl. Acad. Sci. USA* **2017**, *114*, 1335–1340.
[21] M. Saito, D. Hess, J. Eglinger, A. W. Fritsch, M. Kreysing, B. T. Weinert, C. Choudhary, P. Matthias, *Nat. Chem. Biol.* **2019**, *15*, 51–61.
[22] J. Smith, D. Calidas, H. Schmidt, T. Lu, D. Rasoloson, G. Seydoux, *eLife* **2016**, *5*, e21337.
[23] E. A. Sweeny, M. E. Jackrel, M. S. Go, M. A. Sochor, B. M. Razzo, M. E. DeSantis, K. Gupta, J. Shorter, *Mol. Cell* **2015**, *57*, 836–849.
[24] A. Patel, H. O. Lee, L. Jawerth, S. Maharana, M. Jahnel, M. Y. Hein, S. Stoynov, J. Mahamid, S. Saha, T. M. Franzmann, A. Pozniakovski, I. Poser, N. Maghelli, L. A. Royer, M. Weigert, E. W. Myers, S. Grill, D. Drechsel, A. A. Hyman, S. Alberti, *Cell* **2015**, *162*, 1066–1077.
[25] S. Alberti, A. Gladfelter, T. Mittag, *Cell* **2019**, *176*, 419–434.
[26] S. Elbaum-Garfinkle, *J. Biol. Chem.* **2019**, *294*, 7160–7168.
[27] S. Spannl, M. Tereshchenko, G. J. Mastromarco, S. J. Ihn, H. O. Lee, *Traffic* **2019**, *20*, 890–911.
[28] S. Alberti, A. A. Hyman, *Nat. Rev. Mol. Cell Biol.* **2021**, *22*, 196–213.
[29] W. M. Aumiller Jr., C. D. Keating, *Nat. Chem.* **2016**, *8*, 129–137.

[30] W. M. Aumiller Jr., F. Pir Cakmak, B. W. Davis, C. D. Keating, *Langmuir* **2016**, *32*, 10042–10053.

[31] K. K. Nakashima, M. A. Vibhute, E. Spruijt, *Front. Mol. Biosci.* **2019**, *6*, 21.

[32] C. Donau, F. Spath, M. Sosson, B. A. K. Kriebisch, F. Schnitter, M. Tena-Solsona, H. S. Kang, E. Salibi, M. Sattler, H. Mutschler, J. Boekhoven, *Nat. Commun.* **2020**, *11*, 5167.

[33] N. A. Yewdall, A. A. M. André, T. Lu, E. Spruijt, *Curr. Opin. Colloid Interface Sci.* **2021**, *52*, 101416.

[34] S. L. Perry, *Curr. Opin. Colloid Interface Sci.* **2019**, *39*, 86–97.

[35] C. E. Sing, S. L. Perry, *Soft Matter* **2020**, *16*, 2885–2914.

[36] G. A. Mountain, C. D. Keating, *Biomacromolecules* **2020**, *21*, 630–640.

[37] T. Lu, E. Spruijt, *J. Am. Chem. Soc.* **2020**, *142*, 2905–2914.

[38] R. S. Fisher, S. Elbaum-Garfinkle, *Nat. Commun.* **2020**, *11*, 4628.

[39] T. Kaur, M. Raju, I. Alshareedah, R. B. Davis, D. A. Potoyan, P. R. Banerjee, *Nat. Commun.* **2021**, *12*, 872.

[40] N. G. Moreau, N. Martin, P. Gobbo, T. D. Tang, S. Mann, *Chem. Commun.* **2020**, *56*, 12717–12720.

[41] Y. Chen, M. Yuan, Y. Zhang, S. Liu, X. Yang, K. Wang, J. Liu, *Chem. Sci.* **2020**, *11*, 8617–8625.

[42] H. Karoui, M. J. Seck, N. Martin, *Chem. Sci.* **2021**, *12*, 2794–2802.

[43] F. Späth, C. Donau, A. M. Bergmann, M. Kranzlein, C. V. Synatschke, B. Rieger, J. Boekhoven, *J. Am. Chem. Soc.* **2021**, *143*, 4782–4789.

[44] A. M. Bergmann, C. Donau, F. Spath, K. Jahnke, K. Gopfrich, J. Boekhoven, *Angew. Chem. Int. Ed.* **2022**, *61*, e202203928; *Angew. Chem.* **2022**, *134*, e202203928.

[45] M. Tena-Solsona, B. Riess, R. K. Grotsch, F. C. Lohrer, C. Wanzke, B. Kasdorf, A. R. Bausch, P. Muller-Buschbaum, O. Lieleg, J. Boekhoven, *Nat. Commun.* **2017**, *8*, 15895.

[46] F. Schnitter, A. M. Bergmann, B. Winkeljann, J. Rodon Fores, O. Lieleg, J. Boekhoven, *Nat. Protoc.* **2021**, *16*, 3901–3932.

[47] P. R. Banerjee, A. N. Milin, M. M. Moosa, P. L. Onuchic, A. A. Deniz, *Angew. Chem. Int. Ed.* **2017**, *56*, 11354–11359; *Angew. Chem.* **2017**, *129*, 11512–11517.

[48] I. Alshareedah, M. M. Moosa, M. Raju, D. A. Potoyan, P. R. Banerjee, *Proc. Natl. Acad. Sci. USA* **2020**, *117*, 15650–15658.

[49] O. A. Saleh, B. J. Jeon, T. Liedl, *Proc. Natl. Acad. Sci. USA* **2020**, *117*, 16160–16166.

[50] Y. Yin, L. Niu, X. Zhu, M. Zhao, Z. Zhang, S. Mann, D. Liang, *Nat. Commun.* **2016**, *7*, 10658.

[51] A. P. Mahowald, *J. Exp. Zool.* **1962**, *151*, 201–215.

[52] J. M. Johnson, *J. Cell Biol.* **1969**, *43*, 197–206.

[53] A. L. Arkov, J. Y. Wang, A. Ramos, R. Lehmann, *Development* **2006**, *133*, 4053–4062.

[54] K. E. Kistler, T. Trcek, T. R. Hurd, R. Chen, F. X. Liang, J. Sall, M. Kato, R. Lehmann, *eLife* **2018**, *7*, e37949.

[55] J. I. Ahn, J. E. Park, L. Meng, L. Zhang, T. S. Kim, M. J. Kruhlak, B. Y. Kim, K. S. Lee, *Cell Cycle* **2020**, *19*, 3437–3457.

[56] C. Wu, J. Zhao, Q. Wu, Q. Tan, Q. Liu, S. Xiao, *Int. J. Mol. Sci.* **2021**, *22*, 9728.

[57] H. B. Schmidt, R. Rohatgi, *Cell Rep.* **2016**, *16*, 1228–1236.

[58] C. M. Fare, A. Villani, L. E. Drake, J. Shorter, *Open Biol.* **2021**, *11*, 210137.

[59] S. Koga, D. S. Williams, A. W. Perriman, S. Mann, *Nat. Chem.* **2011**, *3*, 720–724.

[60] B. Drobot, J. M. Iglesias-Artola, K. Le Vay, V. Mayr, M. Kar, M. Kreysing, H. Mutschler, T. D. Tang, *Nat. Commun.* **2018**, *9*, 3643.

[61] R. R. Poudyal, R. M. Guth-Metzler, A. J. Veenis, E. A. Frankel, C. D. Keating, P. C. Bevilacqua, *Nat. Commun.* **2019**, *10*, 490.

Research Articles
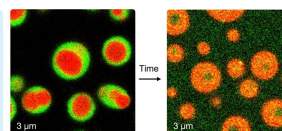
Research Articles

Self-Assembly

C. Donau, F. Späth, M. Stasi,
A. M. Bergmann,
J. Boekhoven* ———————— **e202211905**

Phase Transitions in Chemically Fueled,
Multiphase Complex Coacervate Droplets
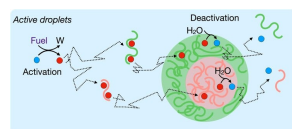
Coupling multiphase coacervate droplets to a chemical reaction cycle allows access to regimes inside the phase diagram not possible under thermodynamic control. Control over the stability, liquidity, and localization of the multiphases makes it a great synthetic platform to study the organization of membraneless organelles.

Supporting Information for:

Phase Transitions in Chemically Fueled, Multiphase Complex Coacervate Droplets

Carsten Donau[1], Fabian Späth[1], Michele Stasi[1], Alexander M. Bergmann[1], Job Boekhoven[1]

[1] Department of Chemistry, Technical University of Munich, Lichtenbergstrasse 4, 85748 Garching, Germany.

Materials and methods

Materials. We purchased 1-ethyl-3-(3-dimethylaminopropyl) carbodiimide (EDC), 2-(N-morpholino)ethanesulfonic acid (MES) buffer, trifluoroacetic acid (TFA), *N,N'*-diisopropylcarbodiimide (DIC), ethyl (hydroxyimino)cyanoacetate (Oxyma), 4-(dimethylamino)-pyridine (DMAP), Wang resin, Rinkamide resin, protected amino acids (Fmoc-N(Trt)-OH, Fmoc-D(OtBu)-OH, Fmoc-G-OH, Fmoc-R(Pbf)-OH, Ac-F-OH), Wang resin, piperidine (99%), triisopropylsilane (TIPS), chloro-7-nitrobenzofurazan (NBD-Cl, 98%), polyuridylic acid potassium salt (pU), poly(styrene sulfonate) sodium salt (pSS), 2-(Dodecylthiocarbonothioylthio)-2-methylpropionic acid (98%), 4,4'-Azobis(4-cyanovaleric acid (ACPA, ≥98%), sodium borohydride, tris(2-carboxyethyl) phosphine (TCEP), ethylenediamine, sodium 4-vinylbenzenesulfonate (SVBS), sulforhodamine 101 and solvents (*N,N*-dimethylformamide (DMF), dichloromethane, diethyl ether) were purchased from Sigma-Aldrich and used without any further purification unless otherwise indicated. Sulfo-cyanine5-maleimide(1-(6-((2-(2,5-dioxo-2,5-dihydro-1H-pyrrol-1-yl)ethyl)amino)-6-oxohexyl)-3,3-dimethyl-2-((1E,3E)-5-((E)-1,3,3-trimethyl-5-sulfonatoindolin-2-yldene)-penta-1,3-dien-1-yl)-3H-indol-1-ium-5-sulfonate) was purchased from Lumiprobe. Nuclease-free water was freshly prepared by filtration (DURAN) of MQ-water. HPLC grade acetonitrile (ACN) was purchased from VWR. Cy3-A$_{15}$, Cy5-A$_{15,}$ and Cy5-U$_{15}$ were purchased from biomers.net GmbH. Ac-FRGRGRGD-OH (tri-trifluoroacetic acid salt) was purchased from CASLO Aps. Ac-FRGRGRGN-NH$_2$ (tri-trifluoroacetic acid salt) was manually synthesized (see below) and purchased from CASLO Aps. NBD-GRGRGRGN-NH$_2$ and NBD-GRGRGRGD-OH (both as tri-trifluoroacetic acid salt) were synthesized following a published procedure[2]. Cy5-pSS was synthesized using RAFT polymerization (see below).

Methods

Synthesis of Ac-FRGRGRGN-NH$_2$. The peptide was synthesized using standard fluoren-9-ylmethoxycarbonyl (Fmoc) solid-phase peptide synthesis on Rinkamide resin on a CEM Liberty microwave-assisted peptide synthesizer. The purity of the peptide was analyzed by electrospray ionization mass spectrometry in positive mode (ESI-MS) and analytical HPLC.

Synthesis of Cy5-pSS. Poly(styrene sulfonate) homopolymer was synthesized via RAFT polymerization. For this purpose, styrene sulfonate sodium salt (SVBS) was polymerized in MQ-water at 75°C with 0.01 eq. 2-(Dodecylthiocarbonothioylthio)-2-methylpropionic acid (98%) and 0.002 eq. of 4,4'-Azobis(4-cyanovaleric acid (ACPA, ≥98%) for 5 hours. The solution was purged before with Argon for 20 minutes to remove air. The crude solution was purified by dialysis against MQ-water in 12-14 kDa MWCO dialysis tubings (Spectra/Por© 4, 29 mm diameter) for 2 days. The product was dried by lyophilization. The CTA-terminated poly(styrene sulfonate) (440 mg) was solubilized in 15 mL MQ-water, 15 mL of a freshly prepared 1M NaBH$_4$ solution were added dropwise and the mixture was then

2

stirred for 3.5 hours at room temperature. The crude solution was dialyzed against MQ-water for 2 days in 12-14 kDa MWCO dialysis tubings (Spectra/Por© 4, 29 mm diameter) and lyophilized. The resulting product was then reacted with 150 eq. of tris(2-carboxyethyl) phosphine (TCEP) at room temperature in DMF for 24 hours. 20 eq. of Sulfo-Cyanine5-maleimide(1-(6-((2-(2,5-dioxo-2,5-dihydro-1H-pyrrol-1-yl)ethyl)amino)-6-oxohexyl)-3,3-dimethyl-2-((1E,3E)-5-((E)-1,3,3-trimethyl-5-sulfonatoindolin-2-ylidene)penta-1,3-dien-1-yl)-3H-indol-1-ium-5-sulfonate) were added to an aliquot of this solution together with a catalytic amount of ethylenediamine and stirred at 50 °C for 24 hours. The crude product was purified by dialysis in a 2000 MWCO Slide-A-Lyzer Dialysis Cassette© (ThermoFisher Scientific) against MQ-water for 2 days and finally lyophilized. Analysis from SEC (Figure S16): Mw = 710 kDa, PDI = 1.4.

Sample preparation. Stock solutions of peptide 2 (Ac-FRGRGRGD-OH, 100-150 mM), MES buffer (500 mM), pU (600-1000 kDa, 15 µg/µL), pSS (17 kDa, 166 mg/mL), fluorescent dyes (1-25 µM), peptide 1 (Ac-FRGRGRGN-NH$_2$, 1-75 mM) and fuel (EDC, 0.5-2 M) were prepared in nuclease-free water. The pH of the peptide and MES stock were adjusted to 5.3. Typically, stock solutions of EDC, as well as the resulting peptide-polymer solution in MES, were prepared freshly for each experiment. For most experiments, we used these standard conditions for active droplets: 15 mM peptide 2, 5 mM pU (monomer units), 5 mM pSS (monomer units), 200 mM MES, pH 5.3, and 50 mM fuel. Reaction networks were started by the addition of fuel to the peptide-polymer solution in MES. For passive droplets, we used these standard conditions: x mM peptide 1, 15-x mM peptide 2, 5 mM pU, 5 mM pSS, 200 mM MES, pH 5.3. Droplet formation was initiated by the addition of a mixture of pSS and pU (with dyes) to a solution in MES containing both peptide 1 and peptide 2.

Hybridization of pU. To track pU fluorescently, we hybridized pU with Cy3-A$_{15}$ or Cy5-A$_{15}$. For that, pU and the fluorescent A$_{15}$ were added into an Eppendorf tube (5 µL). The mixture was incubated at 80 °C for 5 minutes following 0 °C for 5 minutes. The resulting solution was then stored at 25 °C and consumed within an hour.

Isothermal titration calorimetry (ITC). ITC Experiments were performed with a MicroCal PEAQ-ITC from Malvern Pananalytical. All experiments were performed at 25°C. The following conditions were used: pU (1.1 mM uridine units in MES 200 mM, pH 5.3) was titrated with peptide 2 (38 mM in 200mM MES, pH 5.3): 25 injections, 1.5 uL/inj. pU (0.5 mM in 200 mM MES, pH 5.3) was titrated with peptide 1 (5 mM as charged units, 1.67 mM as peptide concentrations in 200 mM MES, pH 5.3): 19 injections, 2uL/inj. pSS (1 mM sulfonate unit in 200 mM MES, pH 5.3) was titrated with peptide 2 (15 mM in 200 mM MES, pH 5.3): 25 injections, 1 uL/inj. pSS (0.025 mM sulfonate unit in 200 mM MES, pH 5.3) was titrated with peptide 1 (0.375 mM as charged units, 0.125 mM as peptide concentrations in 200 mM MES, pH 5.3): 16 injections, 2uL/inj. All experiments were performed in triplicate (N=3). For each

3

experiment, a control was performed by titrating the corresponding amount of peptide in 200 mM MES buffer (pH 5.3) in absence of polyanions. Data were fitted using a non-linear least squares algorithm provided with the PEAQ-ITC Analysis software. All titrations were performed in a regime of concentrations where no phase-separation behavior could be observed.

UV/Vis Spectroscopy. The UV/Vis measurements were carried out using a Microplate Spectrophotometer (Thermo Scientific Multiskan GO). Samples (100 μL) were directly prepared into a 96 well-plate (tissue culture plate non-treated) and the absorbance as a measure for turbidity was monitored at 600 nm every minute. Measurements were performed at 25 °C. Each experiment was performed in triplicate.

Fluorescence Spectroscopy. Fluorescence spectroscopy was performed on a Jasco (Jasco FP-8300) spectrofluorimeter. Samples (100 μL) were added to a cuvette and the fluorescence was measured at specific wavelengths depending on the dye (see confocal settings). Measurements were performed at 24°C. Each experiment was performed in triplicate.

Confocal Fluorescence Microscopy. Confocal fluorescence microscopy was performed on a Leica TCS SP8 confocal microscope using a 63x water immersion objective (1.2 NA). Samples (V = 30 μL) were prepared as described above in PVA-coated[2] micro-well plates (ibidi, μ-Slide Angiogenesis Glass Bottom), but with 0.15 μM Cy3-RNA, 0.15 μM Cy5-RNA, 0.15 μM Cy5-pSS and/or 1 μM NBD-peptide as the fluorescent dye. Samples were excited with 488 nm (NBD), 552 nm (Cy3), and 638 nm (Cy5) and imaged at 498-550 nm, 560-630 nm, and 650-710 nm, respectively. A sequential scan was employed when more than one dye was present in the sample. Images of passive droplets were typically obtained 10 minutes after droplet formation. Measurements were performed at 24 °C.

Fluorescent recovery after photobleaching (FRAP). The diffusivity of the molecules inside active droplets was measured via spot bleaching. The region of interest (ROI) was set to a radius of 0.8 μm inside droplets with a diameter of a couple of micrometers. For peptide 2, samples containing 1 μM NBD-GRGRGRGD-OH (fluorescent peptide 2) at standard conditions were bleached and excited with a 488 nm laser and imaged at 498-550 nm with an image size of 144x80 pixels. 5 pre-bleaches (every 53 ms) were acquired followed by 3 bleaching pulses (every 53 ms). After that, fluorescence recovery was tracked every 53-500 milliseconds with a total of up to 107 images. For pSS, samples containing 0.15 μM Cy5-pSS at standard conditions were bleached and exited at 638 nm and imaged at 650-710 nm with an image size of 256x100 pixels. 5 pre-bleaches (every 0.19 s) were acquired followed by 10 bleaching pulses (every 0.19 s). After that, fluorescence recovery was tracked every 0.19-1.0 seconds with a total of up to 163 images. To measure the diffusivity of pSS and pU in samples with either 10

4

mM pSS or pU at standard conditions with 0.15 µM dye, samples were bleached and exited at either 552 nm or 638 nm and imaged at 560-630 or 650-710 nm with an image size of 512x64 pixels. The raw data was then grouped into time regimes after fuel addition (*e.g.* 0-7 min, 10-15 min,..). After double normalization[3], the data were fitted to a first-order exponential equation[4] with the spot size and the diffusion coefficient to obtain the diffusion coefficient and half-time recovery, as previously described.[2] For the vacuole phase, it was only possible to immobilize the vacuole for a couple of seconds. As a result, we could only accurately determine the diffusion of the peptide in the vacuole since it is a small molecule, and its fluorescent intensity recovers much faster than pU and pSS. Here, the image size was 80x40 pixels and the raw data was only subtracted from the background without normalization of neighboring droplets. To measure the diffusivity of pU in the pSS phase of active multiphase droplets, we hybridized pU with Cy5-A$_{15}$-pU in presence of sulforhodamine (to better visualize the droplets). Samples were then bleached and excited with a 638 nm laser and imaged at 650-710 nm with an image size of 144x80 pixels. 5 pre-bleaches (every 53 ms) were acquired followed by 10 bleaching pulses (every 53 ms). After that, fluorescence recovery was tracked every 53-500 milliseconds with a total of up to 107 images. Since the partitioning of pU in the pSS phase is close to 1, we did not subtract the background but only corrected it for photobleaching by a neighboring droplet. Error bars for all experiments show the standard deviation from two experiments with three droplets each (*N=6*) per time point.

Microfluidic chip production:
Microfluidic PDMS (Polydimethylsiloxane, Sylgard 184, Dow Corining)-based devices were designed with QCAD-pro (RibbonSoft GmbH) and fabricated using photo- and soft-lithography[5] as previously described.[6]

Microfluidic droplet formation:
Surfactant-stabilized water in oil droplets was produced using 2% 008-FluoroSurfactant in 3M Novec7500 as the oil phase, fuel in MQ water as one of the water phases and peptide 2, polyanions and dyes in MES buffer at pH 5.3 as the second water phase. Both water phases contained the doubled concentrations of the respective components with respect to the standard conditions and were mixed in a 1-to-1 ratio to yield the standard concentrations inside the microfluidic droplets. Both aqueous phases and the oil phase were injected into the microfluidic PDMS-based device through polytetrafluoroethylene (PTFE) tubes (0.4-0.9 mm, Bola, Germany) using a flow control system (ELVEFLOW Pressure Controller OB1 MK3). Typically, pressures of 610 mbar for the water phases and 810 mbar for the oil phase were used to produce stable water in oil droplets with a diameter of 40 µm.

HPLC. The concentration profiles of the fuel, peptide 2, and activated peptide 2 during the chemical reaction cycle were monitored over time using analytical HPLC (ThermoFisher,

5

Vanquish Duo UHPLC, HPLC) with a Hypersil Gold 100 2.1 mm C18 column (3 mm pore size). To determine the EDC concentration over time, a turbid sample (V = 10 μL) of active droplets in an HPLC vial with an inlet at standard conditions was diluted with 10 μL of an aqueous NaCl solution (4M) at a given time point and directly injected into the HPLC. Separation was performed using a linear gradient of ACN (2 to 98%) and water with 0.1% TFA and the chromatogram was analyzed using detectors at 220 nm and 254 nm. To determine the activated peptide 2 concentration, a benzylamine quench was used.[1b, 7] Briefly, at each time point, 10 μL from a sample containing active droplets (V = 120 μL) in a 96 well plate were added into 20 μL of an aqueous solution of benzylamine (300 mM) in an HPLC vial. After the addition of 10 μL of an aqueous NaCl solution (4M), the samples were directly injected into the HPLC with the settings from above. All measurements were performed at 25 °C. Each experiment was performed in triplicate.

Kinetic model. A kinetic model written in MATLAB was used to predict the evolution of fuel, peptide 2, and activated peptide 2 over time. The model is described in detail in our previous work.[1] The MATLAB code is available at https://github.com/BoekhovenLab/Dynamic-droplets.

Measuring the concentrations in the phase outside of the droplets ($c_{outside}$). Passive droplets: a solution of passive droplets (V = 150 μL) prepared at standard conditions with 1 μM NBD-GRGRGRGN-NH_2 (fluorescent peptide 1) and 0.15 μM Cy5-pSS in an Eppendorf tube was vortexed for 10 seconds and then centrifuged for 10 minutes at 20,412×g. The supernatant (V = 100 μL) was removed and added to an Eppendorf tube containing 1 μL of an aqueous solution of NaCl (4 M) to dissolve residual turbidity. The fluorescence of the sample was then measured on the fluorimeter. To account for the dependence of the fluorescence of dyes on their environment,[8] we prepared an identical sample w/o dye and added the supernatant (85-95 μL) to an Eppendorf tube containing 1 μL of an aqueous solution of NaCl (4 M). To the clear solution, we then added the same amount of dye (5-15 μL) as in the previous sample and measured its fluorescence intensity. The intensity ratio between these 2 samples was therefore the fraction of the fluorescent molecules that remained in the supernatant. Error bars show the standard deviation from the average (*N=3*).
Active droplets: to a solution of active droplets (V = 150 μL) prepared at standard conditions with 1 μM NBD-GRGRGRGD-OH (fluorescent peptide 2), 0.15 μM Cy3-A_{15} or 0.15 μM Cy5-pSS, 50 mM EDC was added. At a given timepoint, the sample was centrifuged for 1 min at 20,412×g. The fraction of fluorescent molecules that remained in the supernatant was then measured and quantified as for passive droplets. Since fluorescent peptide 2 can also be activated by the fuel, the measured intensity is reflecting the partitioning of peptide 2 and activated peptide 2 combined. Error bars show the standard deviation from the average (*N=3*).

6

Calculating the concentrations inside the droplets and the resulting partitioning coefficient.
We determined the droplet volumes of passive droplets at standard conditions after centrifugation of the turbid suspensions (V = 150 μL) for 10 minutes at 20,412×g. The resulting droplet pellet (0.2 – 1.5 μL) was then compared to size standards visually. We then calculated the concentration in the droplet phase by subtracting the number of molecules in the phase outside of the droplets from the total amount in the solution. Partitioning coefficients K were obtained by the ratio of the concentration in the droplets and the concentration outside of the droplets.

Calculating concentrations inside the vacuole phase. We measured the fluorescence intensity profiles of active droplets via confocal fluorescence microscopy, 22 minutes after the addition of 50 mM fuel under standard conditions. The resulting partitioning coefficients $K_{vacuole}$ were then multiplied with the concentration in the phase outside of the droplets $c_{outside}$ obtained from the fluorimeter (see method above) to give the concentrations inside the vacuole $c_{vacuole}$ (Table S2). We performed control experiments to verify that the dye's fluorescence hardly varies with the pSS concentration. Specifically, we prepared individual samples with identical dye concentrations in 200 mM MES at pH 5.3 and varied the pSS concentration up to 30 mM. In the regime between 4 mM and 30 mM pSS, the increase of the dyes' fluorescence was negligible. Error bars of $K_{vacuole}$ show the standard deviation from 5 droplets containing vacuoles ($N = 5$). Error bars of $c_{vacuole}$ were derived from error bars of $c_{outside}$ and $K_{vacuole}$.

Estimating the viscosity of the pSS phase. To estimate the viscosities of the pSS phase during the reaction cycle, we used the Stokes-Einstein relationship: $D = \frac{k_B T}{6\pi\eta R_h}$, where D is the diffusion coefficient, k_B is the Boltzmann constant, T is the temperature, η is the viscosity and R_h is the hydrodynamic radius. Under the assumption of the droplets behaving as equilibrium Newtonian liquids, the droplets' viscosity can be estimated as a first approximation.[9] D values of pSS were used from FRAP experiments. R_h of pSS was assumed to be approximately 10 nm based on the literature.[10]

Determining the critical coacervation concentration (CCC) and critical salt concentration (CSC) of passive droplets. The CCC concentrations of passive droplets were determined by increasing the amount of peptide 1 gradually by pipetting increasing amounts of a 100 mM stock solution into a sample containing either 10 mM pSS or 10 mM pU in 200 mM MES at pH 5.3. Turbidity was measured by UV/vis spectrometry at 600 nm. Turbidity values above the blank value (0.085 absorbance) were taken as the indicator for phase separation.
Critical salt concentrations were determined accordingly, but different amounts of a 4M NaCl stock solution were added to samples containing 2.5 mM of peptide 1, 10 mM of pSS or 10 mM pU in 200 mM MES at pH 5.3.

7

Supplementary discussion 1:

We performed a control experiment to indirectly demonstrate that A_{15} must be mostly hybridized even in the droplet environment. For that, we used our conditions for active multiphase droplets based on pU and pSS. As dyes, we used Cy3-A_{15}-pU and Cy5-U_{15} instead of Cy5-pSS. Cy5-U_{15} cannot base-pair with pU. Indeed, we observed that U15 localized into the pSS phase during vacuole formation (Figure S7). Thus, there is a significant difference in the partitioning of non-hybridized U_{15} compared to hybridized A_{15}. A_{15} and U_{15} should only show disparate partitioning in multiphase droplets if base-pairing is present,[11] i.e., the pU-phase selects for one of the two nucleic acids via hybridization. Thus, we conclude that the Cy3-emission from A_{15} indicates pU's location.

Supplementary discussion 2:

The pU shell in active multiphase droplets was too thin for FRAP spot bleaching experiments. Instead, we performed FRAP on pU-only droplets (10 mM) as an indirect measure for the pU shell (Figure S13). To verify whether this assumption was true, we performed control experiments on pSS-only droplets (Figure S15). Here, the diffusivities obtained for the peptide and pSS were in the same range as for the pSS core in multiphase droplets, indicating that the measured diffusivities in pU-only droplets can be used as an estimate for the pU shell in multiphase droplets.

Table S1. *Critical coacervation concentration (CCC) and critical salt concentration (CSC) of passive pSS and pU droplets with peptide 1.*

	pSS	pU
CCC	0.8 ± 0.1 mM	1.85 ± 0.05 mM
CSC	>1.5 M	63 ± 12 mM

Values derived from UV-vis spectroscopy. Conditions for CCC of peptide 1: 10 mM pSS or 10 mM pU, 200 mM MES, pH5.3. Conditions for CSC of NaCl: 2.5 mM peptide 1, 10 mM pSS or 10 mM pU, 200 mM MES, pH5.3. Error bars show the standard deviation from the average (N=3).

8

Table S2. *Concentrations of molecules in the vacuole phase of active droplets*.

	pSS	pU	Peptide 2*
$c_{outside}$	4.0 ± 0.2 mM	5.1 ± 0.1 mM	8.4 ± 0.4 mM
$K_{vacuole}$	4.7 ± 1.3	2.2 ± 0.1	10.6 ± 0.3
$c_{vacuole}$	18.8 ± 6.2 mM	11.2 ± 0.7 mM	89.0 ± 6.3 mM

Concentrations represent peptide 2 and activated peptide 2 combined.

K_D	pSS	pU
Peptide 1	3.2 ± 1.5 μM	130 ± 50 μM
Peptide 2	110 ± 1.0 μM	14 ± 4.5 mM

ΔG / kcal mol^{-1}	pSS	pU
Peptide 1	-7.55 ± 0.3	-5.33 ± 0.3
Peptide 2	-5.42 ± 0.0	-2.60 ± 0.3
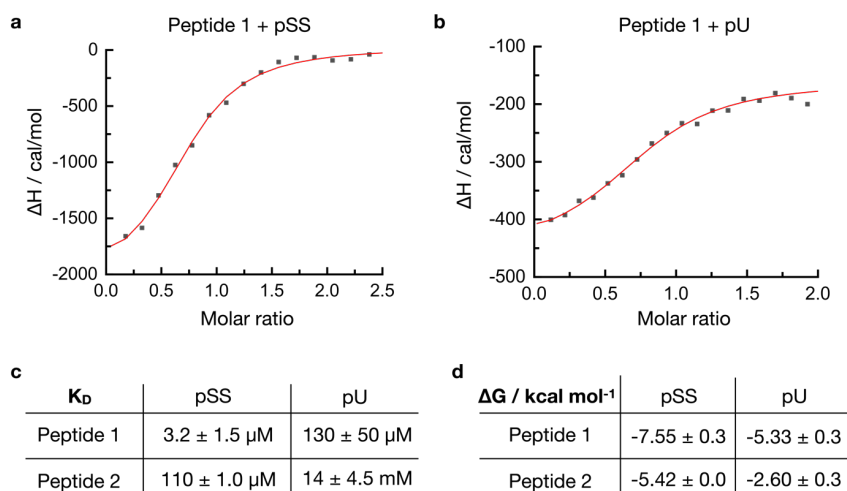
Figure S1: *Binding affinity between the peptides and polyanions. (**a-b**) Change in enthalpy measured by ITC for the interaction between peptide 1 and pSS (a) and pU (b). (**c-d**) Dissociation constant (c) and free energy (d) of the interaction between peptide 1 and 2 with the two polyanions. Errors show the standard deviation from the average (N=3). For conditions, see methods.*
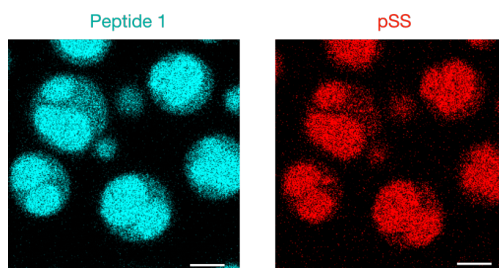
Figure S2: *Localization of peptide 1 in passive multiphase droplets. Confocal micrographs of fluorescent peptide 1 (left) and pSS (right) of passive droplets. Conditions: 2.5 mM peptide 1, 12.5 mM peptide 2, 5 mM pU, 5 mM pSS, 200 mM MES, pH5.3, 1 μM NBD-GRGRGRGN-NH$_2$ (cyan) and 0.15 μM Cy5-pSS (red). Scale bar: 3 μm.*

10
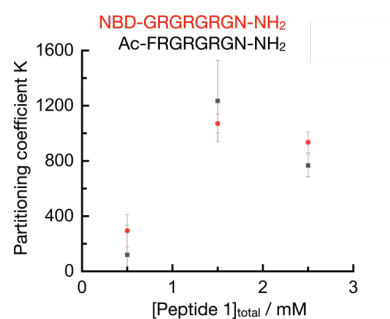
Figure S3: *Partitioning of peptide 1 in passive droplets. Partitioning coefficient of NBD-GRGRGRGN-NH₂ (fluorescent peptide 1, red) and Ac-FRGRGRGN-NH₂ (peptide 1, black) in the droplet phase as a function of the total concentration of peptide 1 for passive droplets at standard conditions. Values of the unlabeled peptide were determined by centrifugation and HPLC. Error bars show the standard deviation from the average (N=3).*

11
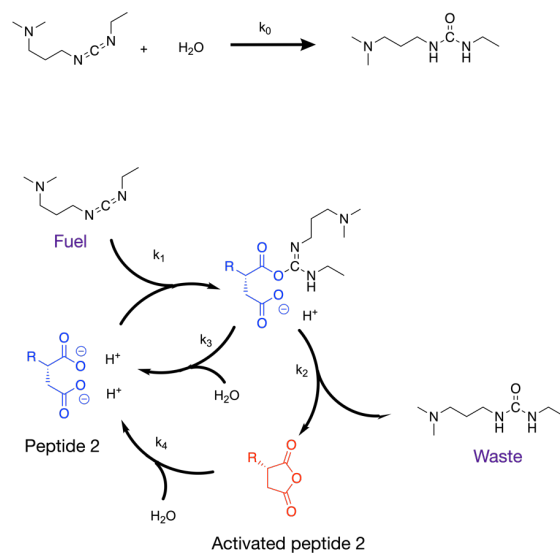
Figure S4: *Chemical reaction cycle in active droplets. All reactions taking place simultaneously. This reaction cycle has been described in detail in our previous work.[1] The rate constants (k) refer to the rate constants used in our kinetic model.*

12
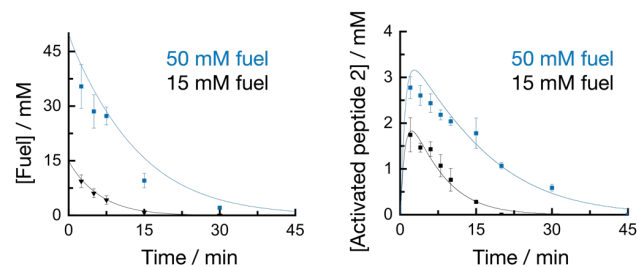
Figure S5: *Evolution of fuel and peptide concentrations over time. Fuel and peptide concentrations over time measured by HPLC for 15 mM (black) and 50 mM (blue) fuel at standard conditions for active droplets. Error bars show the standard deviation from the average (N=3). Lines represent fitting plots from our kinetic model. Fitting parameters: $k_1(15mM) = 0.1\ M^{-1}s^{-1}$, $k_1(50mM) = 0.05\ M^{-1}s^{-1}$, $k_2 = 0.2\ s^{-1}$, $k_3 = 0\ s^{-1}$, $k_4 = 0.015\ s^{-1}$.*
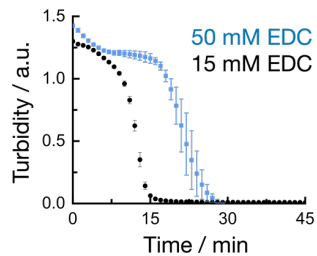
Figure S6: *Evolution of turbidity in active droplets over time. Absorbance of 600 nm of light as a measure for turbidity for standard conditions of active droplets with 15 mM (black) or 50 mM (blue) fuel. Error bars show the standard deviation from the average (N=3).*

13
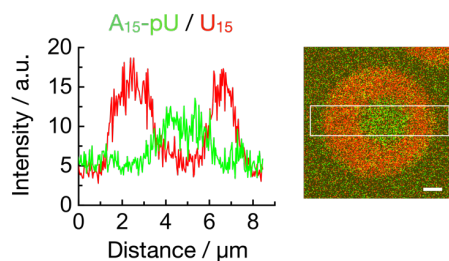
Figure S7: *Comparing the partitioning of A_{15} and U_{15} in active droplets at transition 3. Confocal micrographs of a sample containing active droplets at standard conditions, 22 minutes after the addition of 50 mM fuel but with Cy3-A_{15}-pU (green) and Cy5-U_{15} (red) instead of Cy5-pSS. Scale bar: 1 µm.*
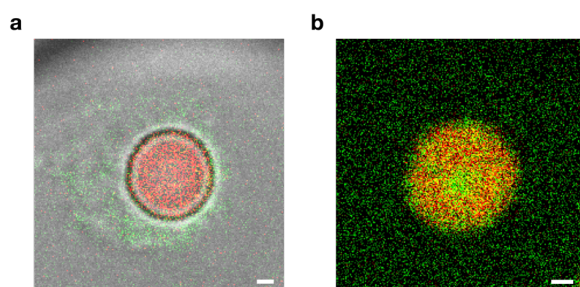
Figure S8: *Transition 2 and 3 in the microfluidic set-up. (a) Dissolution of pU at standard conditions of active droplets with 50 mM fuel, 0.15 µM Cy3-A15-pU (green) and 0.15 µM Cy5-pSS (red). (b) Re-partitioning of pU into the pSS phase. Scale bar: 1 µm.*

14
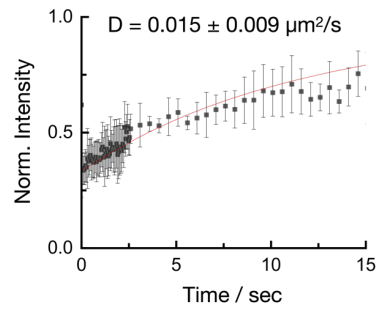
Figure S9: *Diffusivity of pU in the pSS phase in active multiphase droplets. FRAP spot bleaching experiments of active droplets with 50 mM fuel at standard conditions with 0.15 µM Cy5-A$_{15}$-pU and 0.15 µM sulforhodamine at various time points. Red lines indicate fitting functions with corresponding diffusion coefficient D. Errors bars show the standard deviation of 6 droplets from 2 experiments (N=6).*
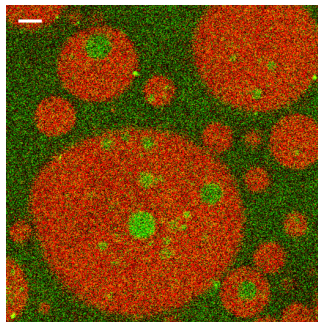

Figure S10: *Vacuole conditions in the bulk phase. Confocal micrographs of fluorescent pU (green) and pSS (red) of a sample containing similar concentrations of molecules as the vacuole phase in active droplets. Conditions: 89 mM peptide 2, 11 mM pU, 19 mM pSS, 200 mM MES, pH5.3, 0.15 µM Cy3-A$_{15}$-pU (green) and 0.15 µM Cy5-pSS (red). Scale bar: 5 µm.*

15
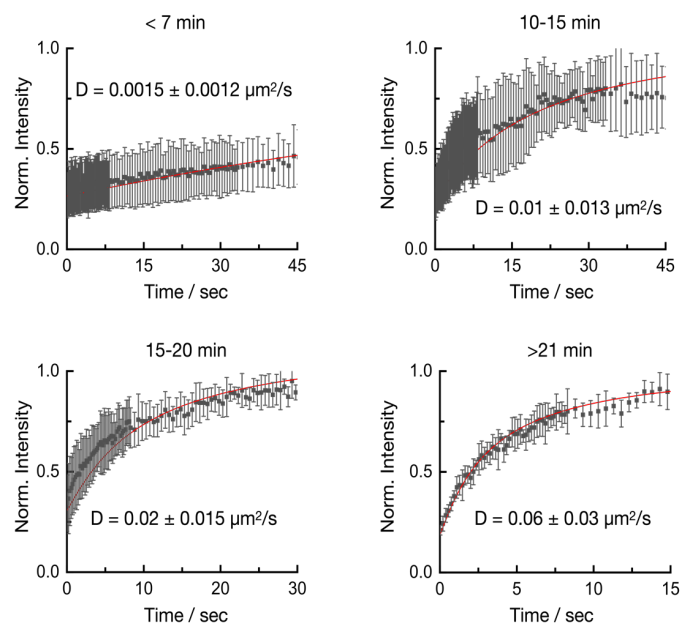
Figure S11: *Diffusivity of pSS in the pSS phase in active multiphase droplets. FRAP spot bleaching experiments of active droplets with 50 mM fuel at standard conditions with 0.15 µM Cy5-pSS at various time points. Red lines indicate fitting functions with corresponding diffusion coefficient D. Errors bars show the standard deviation of 6 droplets from 2 experiments (N=6).*
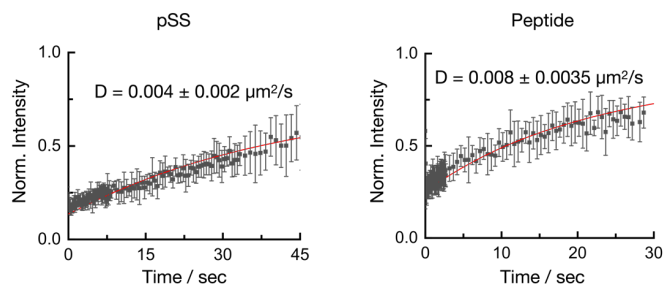
16
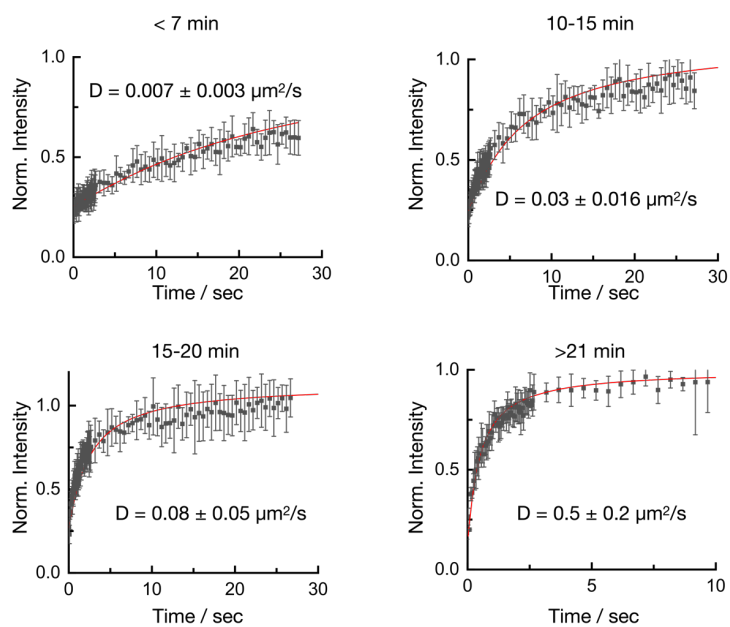
Figure S12: *Diffusivity of the peptide in the pSS phase in active multiphase droplets. FRAP spot bleaching experiments of active droplets with 50 mM fuel at standard conditions with 1 μM NBD-GRGRGRGD-OH at various time points. Red lines indicate fitting functions with corresponding diffusion coefficient D. Errors bars show the standard deviation of 6 droplets from 2 experiments (N=6). Since the fluorescent peptide can react with the fuel, the measured recovery represents both peptide 2 and activated peptide 2.*
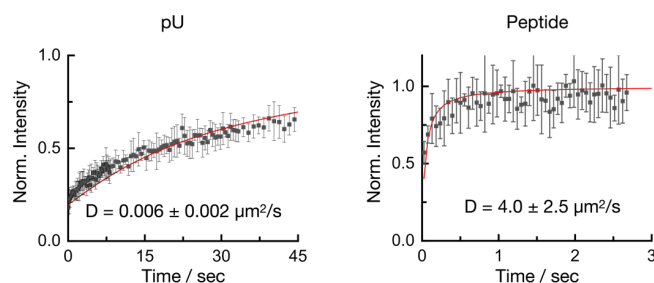
Figure S13: *Diffusivity of pU and the peptide in pU-only active droplets. FRAP spot bleaching experiments of pU-only droplets with 50 mM fuel at standard conditions (10 mM pU w/o pSS) with 0.15 μM Cy3-A$_{15}$-pU or 1 μM NBD-GRGRGRGD-OH during the first minutes after fuel addition. Red lines indicate fitting functions with corresponding diffusion coefficient D. Errors bars show the standard deviation of 6 droplets from 2 experiments (N=6). Since the fluorescent peptide can react with the fuel, the measured recovery represents both peptide 2 and activated peptide 2.*
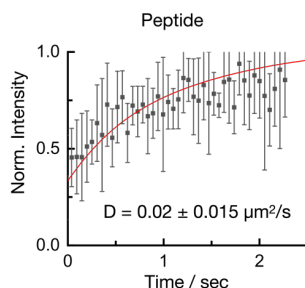
Figure S14: *Diffusivity of the peptide in the vacuole phase in active multiphase droplets. FRAP spot bleaching experiments of active droplets with 50 mM fuel at standard conditions with 1 μM NBD-GRGRGRGD-OH in the vacuole phase. Red lines indicate fitting functions with corresponding diffusion coefficient D. Errors bars show the standard deviation of 6 droplets from 2 experiments (N=6). Since the fluorescent peptide can react with the fuel, the measured recovery represents both peptide 2 and activated peptide 2.*

Figure S15: *Diffusivity of pSS and the peptide in pSS-only active droplets. FRAP spot bleaching experiments of pSS-only droplets with 50 mM fuel at standard conditions (10 mM pSS w/o pU) with 0.15 μM Cy5-pSS or 1 μM NBD-GRGRGRGD-OH during the first minutes after fuel addition. Red lines indicate fitting functions with corresponding diffusion coefficient D. Errors bars show the standard deviation of 6 droplets from 2 experiments (N=6). Since the fluorescent peptide can react with the fuel, the measured recovery represents both peptide 2 and activated peptide 2.*
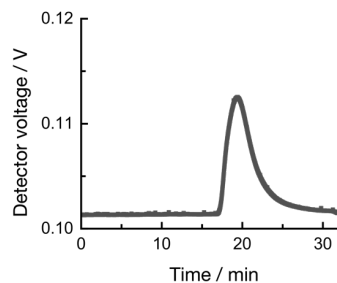
Figure S16: *Characterisation of the synthesized Cy5-pSS. Size Exclusion Chromatography (SEC) chromatogram of unmodified poly(styrene sulfonate) in a 1:1-mixture of H_2O and THF with 9 g/L tetra-n-butylammonium bromide (TBAB) and 340 mg/L 3,5-di-tert-butyl-4-hydroxytoluene (BHT) as the eluent at 40 °C and a flow rate of 0.6 mL/min. A combination of two Agilent PL PolargelM columns (7.5 x 300 mm) was used.*

19

References

[1]   a) M. Tena-Solsona, B. Riess, R. K. Grotsch, F. C. Lohrer, C. Wanzke, B. Kasdorf, A.
         R. Bausch, P. Muller-Buschbaum, O. Lieleg, J. Boekhoven, *Nat. Commun.* **2017**, *8*,
         15895; b) C. Donau, F. Spath, M. Sosson, B. A. K. Kriebisch, F. Schnitter, M. Tena-
         Solsona, H. S. Kang, E. Salibi, M. Sattler, H. Mutschler, J. Boekhoven, *Nat. Commun.*
         2020, *11*, 5167.
[2]   F. Spath, C. Donau, A. M. Bergmann, M. Kranzlein, C. V. Synatschke, B. Rieger, J.
         Boekhoven, *J. Am. Chem. Soc.* **2021**, *143*, 4782-4789.
[3]   S. A. G. Robert D. Phair, Tom Misteli, *Meth. Enzymol.* **2003**, *375*, 393-414.
[4]   A. B. Kayitmazer, H. B. Bohidar, K. W. Mattison, A. Bose, J. Sarkar, A. Hashidzume,
         P. S. Russo, W. Jaeger, P. L. Dubin, *Soft Matter* **2007**, *3*, 1064-1076.
[5]   J. C. M. David C. Duffy, Olivier J. A. Schueller, and George M. Whitesides, *Anal. Chem.*
         1998, *70*, 4974–4984.
[6]   a) M. Weiss, J. P. Frohnmayer, L. T. Benk, B. Haller, J. W. Janiesch, T. Heitkamp, M.
         Borsch, R. B. Lira, R. Dimova, R. Lipowsky, E. Bodenschatz, J. C. Baret, T. Vidakovic-
         Koch, K. Sundmacher, I. Platzman, J. P. Spatz, *Nat. Mater.* **2018**, *17*, 89-96; b) T. W.
         Hofmann, S. Hanselmann, J. W. Janiesch, A. Rademacher, C. H. Bohm, *Lab Chip*
         2012, *12*, 916-922.
[7]   F. Schnitter, J. Boekhoven, *ChemSystemsChem* **2020**, *3*, e2000037.
[8]   T. J. Nott, T. D. Craggs, A. J. Baldwin, *Nat. Chem.* **2016**, *8*, 569-575.
[9]   a) C. P. Brangwynne, C. R. Eckmann, D. S. Courson, A. Rybarska, C. Hoege, J.
         Gharakhani, F. Julicher, A. A. Hyman, *Science* **2009**, *324*, 1729-1732; b) B. Drobot, J.
         M. Iglesias-Artola, K. Le Vay, V. Mayr, M. Kar, M. Kreysing, H. Mutschler, T. D. Tang,
         Nat. Commun. **2018**, *9*, 3643.
[10]   U. Böhme, U. Scheler, *Macromol. Chem. Phys.* **2007**, *208*, 2254-2257.
[11]   G. A. Mountain, C. D. Keating, *Biomacromolecules* **2020**, *21*, 630-640.

20

Chapter 7

Continuous fueling of coacervate droplets and liquid spherical shells

The following chapter is based on a project that I share with Alexander M. Bergmann from the Boekhoven group that has not yet been peer-reviewed.

I have shown that coacervate droplets that are fueled with a batch of fuel show exciting new properties. In this chapter, I focus on such droplets that are continuously fueled to compare them with similar droplets in theoretical studies.

Introduction

In chapter 3, I discussed that droplets in numerical simulations show repetitive self-division when droplet building blocks are activated for phase separation outside of the droplets and deactivated within. Experimental models are thus needed to examine whether these theoretical predictions are of relevance for biology or the origin of life field. In chapter 5 and 6, I established a chemically fueled droplet model where activation is occurring outside of the droplets, and deactivation inside. However, these studies work under conditions where the fuel is continuously depleting unlike numerical simulations in theory-based studies. Also, biology uses steady-state levels of reactants.[152–154] Since examples of continuously fueled droplets are scarce, we aimed to design a droplet model that operates at steady-state levels of fuel. The steady state of fuel would result in steady-state levels of activated building blocks (anhydride).

Results and discussion

In previous work, re-pipetting of fuel into an emulsion containing oil droplets gave oscillating levels of the activated building block around a steady state.[133] We designed a similar approach based on chemically fueled coacervate droplets, *i.e.*, droplets made from peptide Ac-FRGRGRGD-OH and polystyrene sulfonate (pSS) (Figure 7.1a). We quantified the turbidity of the solution with a UV/Vis spectrophotometer as a measure for droplet formation. We set the fueling interval to 10 min, and varied the amount of fuel added, *i.e.*, 1-ethyl-3-(3-dimethylaminopropyl) carbodiimide (EDC), from 5 to 20 mM/hr fuel (Figure 7.1b). While 5 mM/hr fuel did not suffice to form droplets, we observed oscillating levels of turbidity in the range between 9 and
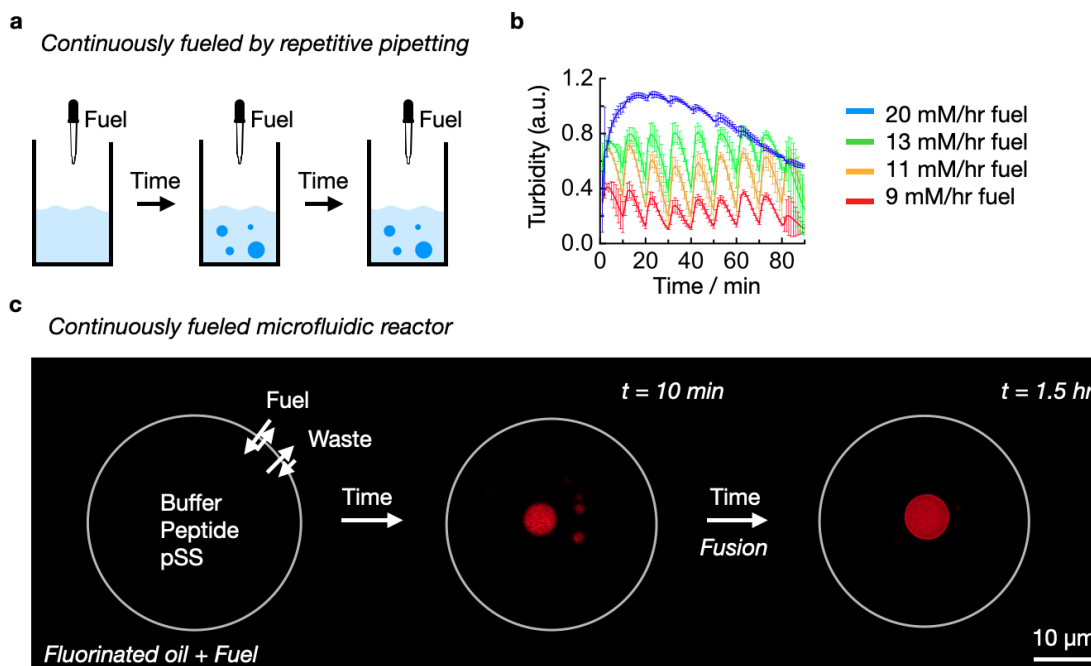
Figure 7.1: Methods to continuously fuel coacervate droplets. (a) Schematic representation of the repetitive addition of fuel via pipetting into a solution containing coacervate building blocks. (b) Absorbance of 600 nm light as a measure of turbidity as a function of time for different fueling rates. Addition of 1-ethyl-3-(3-dimethylaminopropyl) carbodiimide (EDC) in batches every 10 minutes. Complex coacervates from Ac-FRGRGRGD-OH (peptide) and polystyrene sulfonate (pSS) in MES buffer at pH = 5.3 (see materials and methods section). (c) Representative confocal micrographs of a microfluidic droplet over time containing coacervate droplets from peptide and pSS in MES buffer at pH = 5.3 (see materials and methods section). Fluorescence from sulforhodamine. For visualization, the container size is shown slightly reduced. The perfluorinated oil contained 0.5 M of the fuel N,N-diisopropylcarbodiimide (DIC). DIC and its waste product DIU have limited solubility in the water phase and partition preferentially in the oil phase. After the microfluidic droplet is formed, DIC can flow in and coacervate droplets are formed. These droplets sink to the bottom of the microfluidic droplet over time and fuse into a single coacervate droplet. While DIC is consumed to form the droplets, its concentration in the container is set by its solubility in the buffered solution. In other words, as long as there is enough DIC in the oil phase, its concentration in the container equals its solubility throughout the experiment.

13 mM/hr fuel for over an hour. Fueling with 20 mM/hr fuel resulted in precipitation after 30 min most probably due to the accumulation of waste.[139] All in all, repetitive pipetting of fuel into chemically fueled coacervate droplets leads to oscillating values of turbidity.

Repetitive addition of fuel allows to sustain droplets over time but this method comes with several downsides. First, the oscillations in the turbidity (Figure 7.1b) with a fueling interval of 10 min was high, indicating that many droplets had dissolved or had shrunk before the next batch of fuel was added. In other words, while the droplets were continuously fueled, their properties were changing notably due to the large oscillations in activated building blocks. While shortening the fueling interval considerably to a couple of minutes might solve this problem, the analysis of droplets in between the fueling steps in such an approach is inherently difficult, even in automated experimental setups. Moreover, analysis of droplet properties would only be possible on a macroscopic scale, *e.g.*, average droplet number and size, but tracking an individual droplet over the course of multiple fueling cycles via

pipetting would not be possible. Finally, waste accumulation in such continuously fueled conditions is also a considerable obstacle.

Therefore, we designed coacervate droplets that are continuously fueled in a microfluidic reactor adapted from previous work of the Boekhoven group (Figure 7.1c).[140] Instead of mixing EDC as fuel into the microfluidic droplet (container), we added 0.5 M *N,N*-diisopropylcarbodiimide (DIC) into the perfluorinated oil. DIC is more hydrophobic than EDC and is thus considerably more soluble in the perfluorinated oil than in the buffered solution in the container as determined by NMR (> 2 M vs. ~ 10 mM). In other words, the oil surrounding the container serves as a fuel reservoir for the chemical reaction cycle within the container. Once we formed the microfluidic droplet, coacervate droplets were formed within several minutes due to the diffusion of DIC from the oil into the container. Over time, these droplets sank to the bottom of the container and fused into a single coacervate droplet. This droplet was stable and did not grow or shrink for more than 2 hr. The urea waste product DIU is also very hydrophobic and its solubility in the buffered solution is low (~ 30 mM). As a result, most of the waste that is generated in this experiment leaves the container and partitions into the oil phase. Indeed, we typically observe the crystallization of DIU in the fluorinated oil phase.

Taken together, we have established an experimental setup where we create chemically fueled coacervate droplets in a microfluidic reactor. While fuel diffuses into the container from a reservoir surrounding the container, excess waste diffuses out of the container. Simply put, our setup avoids the accumulation of waste which is hampering the continuous fueling of assemblies.[155] Since gravitational-induced fusion always leads to a single droplet at the bottom of the container, this setup allows us to track individual droplets in steady-state, *i.e.*, minimal oscillations of fuel and activated peptide throughout the container (see materials and methods section).

What droplet properties and transitions can be studied in our continuously fueled microreactor? In chapter 5 and 6, I have shown that chemically fueled droplets dissolve through the formation of vacuoles due to the deactivation reaction inside the droplets. In other words, in their pathway towards decay, each droplet transitions into an aqueous phase surrounded by phase-separated material, *i.e.*, a spherical shell (Figure 7.2a-b). We first decided to study the vacuole formation in the bulk solution with a batch of fuel at the confocal microscope (Figure 7.2c). While individual droplets nucleated the vacuole first, most of the droplets transitioned into a spherical shell at the end of the reaction cycle (Figure 7.2d). We quantified the number and size of the droplets that nucleated a vacuole as a function of time (Figure 7.2e). Surprisingly, larger droplets nucleated vacuoles on average earlier than smaller droplets. Also, droplets smaller than 4 µm^3 did not form any vacuoles before dissolution. The interplay between this droplet size dependence on vacuole formation and the fact that their formation is triggered by a chemical reaction suggests a diffusion-limited phenomenon. Simply put, deactivated molecules might take longer to leave a large droplet than a small one which could induce an instability leading to the observed droplet transition.
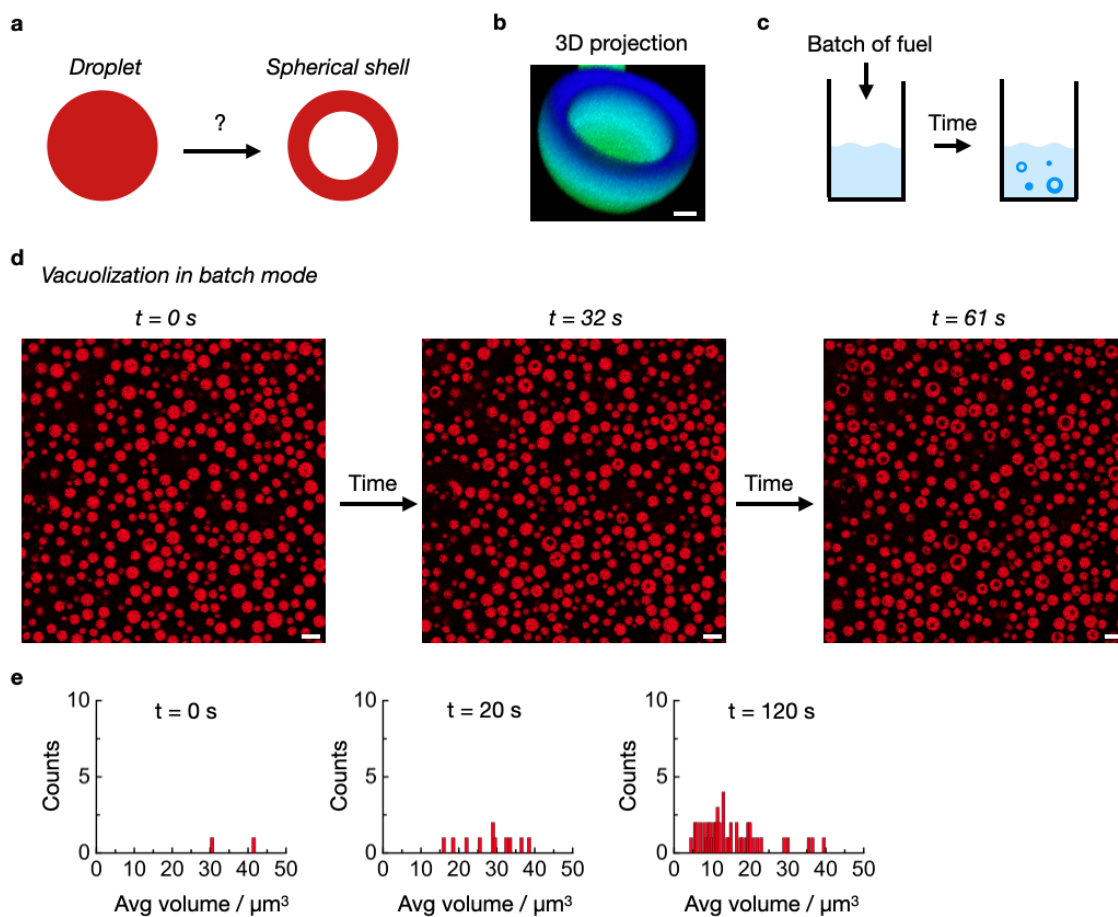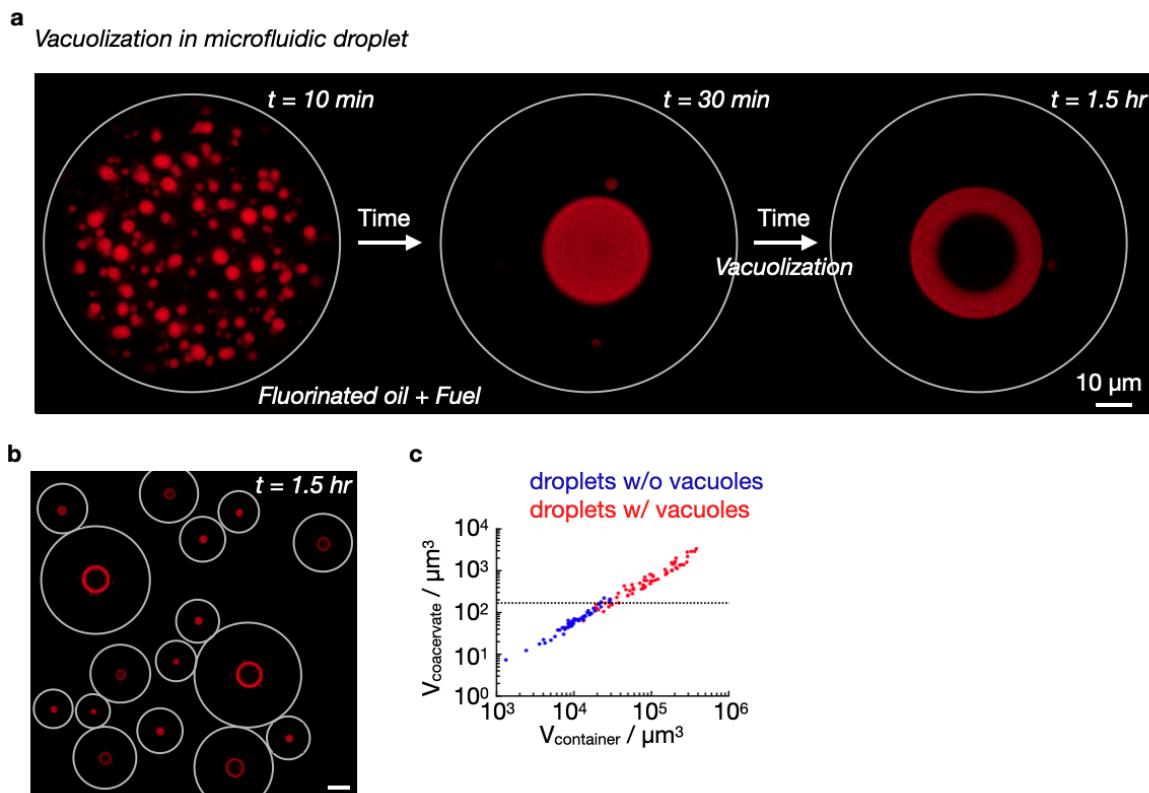
Figure 7.2: Vacuole formation in coacervate droplets that are fueled with a batch of fuel. (a) Schematic representation of a coacervate droplet transitioning to a spherical shell. (b) 3D projection of a representative chemically fueled coacervate droplet with a vacuole. Scale bar: $1\,\mu m$. (c) Schematic representation of the analysis of vacuole formation in batch-fueled droplets. (d) Time series of confocal micrographs of coacervate droplets in the bulk solution. Coacervates from Ac-FRGRGRGD-OH and pSS induced by a finite amount of EDC. Fluorescence from sulforhodamine. Vacuoles form once most fuel is consumed. Scale bar: $5\,\mu m$. (e) The number of droplets containing a vacuole as a function of total droplet size. Histograms over time from the experiment in (d).

We employed our setup from Figure 7.1c to induce vacuolization in a continuously fueled microreactor (Figure 7.3a). Here, we used the same concentrations of peptide and polyanion as in the previous microfluidic experiment (Figure 7.1c) but created a larger microfluidic container. However, the larger the container, the more droplet material is inside. As a result, many coacervate droplets form that then fuse into a large coacervate droplet within tens of minutes (Figure 7.3a). After more than 30 min, a vacuole started to form inside, leading to a spherical shell after 1.5 hr. Preliminary FRAP experiments suggest that this spherical shell is liquid, *i.e.*, the molecules diffuse rapidly inside the droplet. To examine whether vacuole formation is coupled to a certain droplet size as in the batch-fueled experiment, we created microfluidic containers of different sizes that led to differently sized coacervate droplets (Figure 7.3b). Large coacervate droplets transitioned into a spherical shell after 1.5 hr whereas small droplets did not. We quantified the coacervate sizes in relation to the size of the individual containers (Figure 7.3c). There is a linear relationship between the container size and the coacervate volume, *i.e.*, larger containers make bigger coacervate droplets. Excitingly, we could determine a threshold coacervate radius of about 3 µm for vacuole formation. In other words, smaller droplets did not nucleate a vacuole whereas larger droplets mostly transitioned into a spherical shell.

This result has tremendous implications for assemblies away from equilibrium. Unlike in the batch-fueled setup in Figure 7.2c-d, the coacervate droplets in the microfluidic reactors are stable and exist in steady-state. Thus, the transition to a spherical shell is not part of the dissolution process of the droplet as in experiments where only a finite amount of fuel is present. We note that when the DIC-containing oil is exchanged for oil without fuel, the spherical shell vanishes again. This observation suggests that the spherical shell is in an unstable state that is only sustained by the steady state of the chemical reaction cycle. Why do the droplets in the steady-state form a vacuole in the first place? The formation of a vacuole increases the surface area of the droplet significantly due to the additional interface inside the droplet. Also, the droplet swells and grows during that process which further increases the interface between the dilute and droplet phase. Energetically speaking, the formation of a vacuole should not be favorable.

Figure 7.3: Vacuole formation in coacervate droplets that are fueled continuously. (a) Representative confocal micrographs of a microfluidic droplet over time containing Ac-FRGRGRGD-OH and pSS, surrounded by perfluorinated oil containing DIC (Fuel). Fluorescence from sulforhodamine. For visualization, the container size is shown slightly reduced. Many coacervate droplets form in a large container and fuse into one large coacervate droplet. Over time, the coacervate droplet transitions into a spherical shell. (b) Confocal micrograph of microfluidic containers of various sizes of the solution from (a) from various z-planes. The concentrations of peptide and polyanion are identical in all microfluidic containers. The larger the microfluidic container, the more coacervate material it contains. As a result, larger microfluidic containers contain larger coacervates. Not all coacervate droplets contain a vacuole. Scale bar: 20 µm. (c) The size of the fused coacervate in a microfluidic container as a function of the size of the container. Colors show coacervates without (blue) and with (red) a vacuole. The dotted line indicates the transition from droplets to spherical shells.

We explain this behavior by a diffusion-limited mechanism that takes into account the localization of activation and deactivation of our chemical reaction cycle (Figure 7.4a). In our cycle, building block molecules predominantly reside outside of the droplets due to a low affinity to the polyanion. Therefore, the activation by the fuel occurs in the dilute phase. The activated building block in turn has an increased affinity for polyanions and the coacervate phase and thus diffuses into the droplet. Since coacervate droplets are highly hydrated and the activated building block is unstable in water, it is deactivated inside the droplet to the building block which preferentially diffuses out of the droplet again. If we assume a small coacervate droplet, diffusion of the molecules across the droplet boundary should occur readily resulting in a shallow gradient of activated building block inside the droplet (Figure 7.4b). However, in the case of a large droplet, activated building blocks that diffuse into the droplet might be deactivated before they reach the core of the droplet. In other words, a considerable gradient of activated building blocks can build up in large droplets with more product molecules at the droplet boundary, and fewer activated building blocks at the droplet core (Figure 7.4c). As a result, the concentration of activated building blocks in the droplets changes, and its distribution is heterogenous in very large droplets. Normally, the concentration of activated building block inside the droplet is set by the intersection point with the binodal line inside the phase diagram (see chapter 2, Figure 2.4). However, if there is a large gradient of activated building blocks inside the droplet, the concentration of activated building blocks at the droplet core shifts and reaches the spinodal line (Figure 7.4c). Once this occurs, a new phase can spontaneously nucleate within the droplets that is more dilute than the surrounding coacervate phase (spinodal decomposition).

Taken together, we designed chemically fueled droplets under steady-state conditions. We observe non-equilibrium transitions dependent on the size of the droplet which is not possible for droplets that are not regulated by chemical reactions. This droplet model demonstrates the importance of chemical reactions regulating droplets and where they take place. I believe this work serves as an inspiring example of how the behavior of assemblies changes when their properties are coupled to non-equilibrium processes.

While the preliminary work presented here is very promising, more experiments need to be performed to validate the proposed mechanism. For example, we need to build a phase diagram for this droplet model to better understand the transition toward the spinodal line. For that, we are currently collaborating with Prof. Christoph A. Weber and his group with a background in theoretical physics. Moreover, we need to understand better how the increase in the droplet's free energy due to the transition to the spherical shell is compensated, *e.g.*, by the production of entropy. Finally, further experiments are needed to validate the empirical data, *e.g.*, HPLC, NMR, and FRAP experiments.
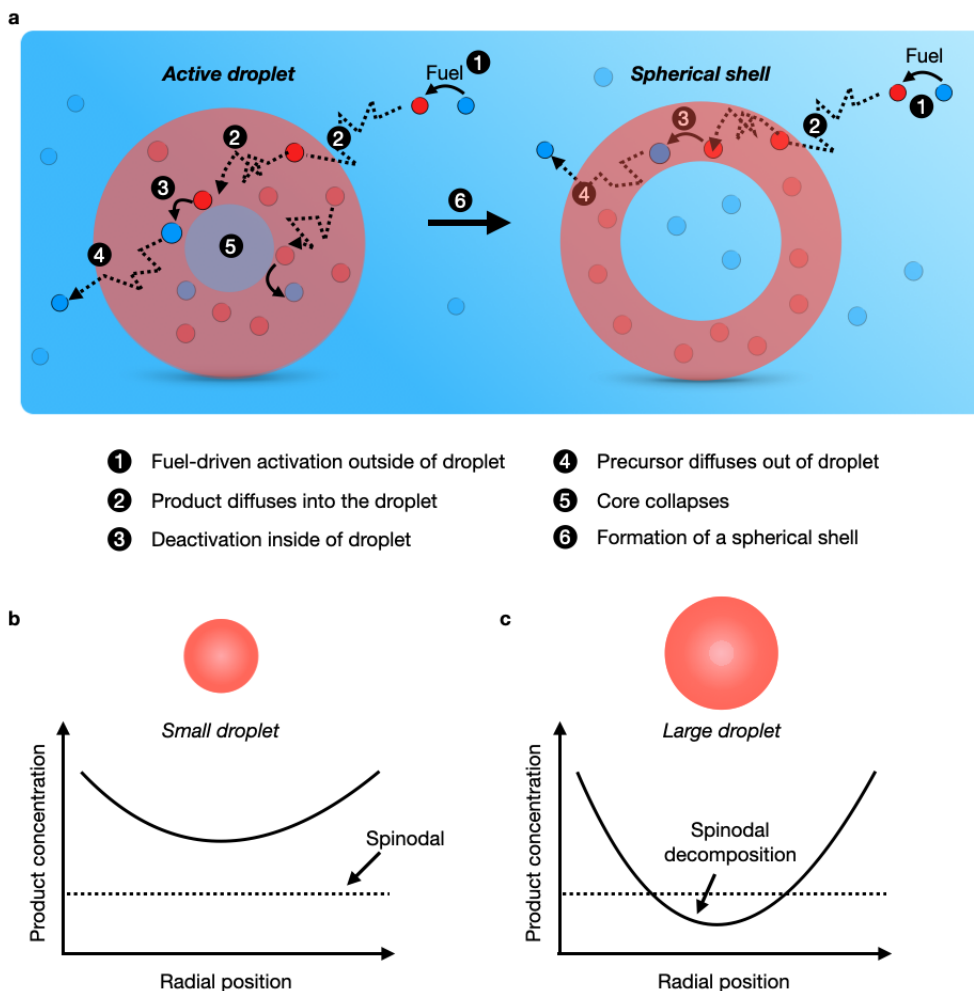
Figure 7.4: Mechanism of the transition of a chemically fueled coacervate droplet transitioning into a spherical shell. (a) Schematic representation of the influx and efflux of molecules into and out of a chemically fueled droplet (active droplet). Disks represent the building block (precursor, blue) and activated building block (product, red) of the chemical reaction cycle. Polyanion strands are not shown. (b-c) Schematic representation of the gradient of product inside a small (b) and large (c) droplet where the product is deactivated in the droplet phase. The concentration of product in the core of a large droplet is significantly lowered and crosses the spinodal line inside the phase diagram, resulting in spinodal decomposition, *i.e.*, the nucleation of a new phase.

Materials and methods

This section contains additional information for chapter 7.

Materials. All solvents were purchased in analytical grade from Sigma Aldrich and used without further purification. Trifluoroacetic acid (TFA, 99 %), polystyrene sulfonic acid (pSS, 75 kDa, 18 % in water), 1-ethyl-3-(3-dimethylaminopropyl)carbodiimide (EDC), *N*,*N*'-diisopropylcarbodiimide (DIC), sulforhodamine B, 4-morpholine-ethanesulfonic acid (MES) buffer were all purchased from Sigma-Aldrich and used without any further purification. Ac-FRGRGRGD-OH was purchased from CASLO Aps. 2 wt% 008-Fluorosurfactant in HFE7500 was purchased from RAN Biotechnologies.

Sample preparation. Stock solutions of Ac-FRGRGRGD-OH (100-150 mM), MES buffer (500-650 mM), pSS (75 kDa, 9 mg/mL), sulforhodamine B (5 μM), and EDC (0.05-2 M) were prepared in MQ water. The pH of the peptide and MES stock were adjusted to 5.3. Typically, stock solutions of EDC, as well as the resulting peptide-polymer solution in MES, were prepared freshly for each experiment. For the batch-fuel experiments, these standard conditions were used: 6 mM Ac-FRGRGRGD-OH, 2.3 mM pSS (monomer units), 200 mM MES, pH 5.3. For the microfluidic experiments, these standard conditions were used: 10 mM Ac-FRGRGRGD-OH, 5 mM pSS (monomer units), 200 mM MES, pH 5.3. Reaction networks were started by the addition of fuel to the peptide-polymer solution in MES.

UV/Vis Spectroscopy. The UV/Vis measurements were carried out using a Microplate Spectrophotometer (Thermo Scientific Multiskan GO). Samples (100 μL) were directly prepared into a 96 well-plate (tissue culture plate non-treated) and the absorbance as a measure for turbidity was monitored at 600 nm every minute. Measurements were performed at 25 °C. Each experiment was performed in triplicate.

High Performance Liquid Chromatography (HPLC). The concentration profiles of the activated Ac-FRGRGRGD-O (anhydride) were monitored over time using analytical HPLC (ThermoFisher,Vanquish Duo UHPLC, HPLC) with a Hypersil Gold 100 2.1 mm C18 column (3 mm pore size). The separation was performed using a linear gradient of acetonitrile (2 to 98 %) and water with 0.1 % TFA and the chromatogram was analyzed using detectors at 220 nm and 254 nm. All measurements were performed at 25 °C.

Confocal fluorescence microscopy. A lightning SP8 confocal microscope (Leica) with a 63x water immersion objective (1.2 NA) was used to analyze the coacervates in the bulk and in a microfluidic droplet. Sulforhodamine B was added to track the coacervates via fluorescence, and the dye was excited at 552 nm and imaged at 565-700 nm. The pinhole was set to 1 Airy unit. For droplets in batch fueling, poly(vinyl alcohol)-coated micro-well plates (ibidi, -Slide Angiogenesis Glass Bottom) were used.[156] To analyze the evolution of coacervates in the entire microfluidic droplet (container), time series imaging of a single microfluidic container was acquired in z-stacks with 1 μm between z-planes.

Nuclear magnetic resonance (NMR). ^{1}H-NMR spectra were recorded with 16 to 64 scans at room temperature on a Bruker AVHD500 spectrometer.

Continuous fueling via repetitive pipetting. To Ac-FRGRGRGD-OH and pSS at standard conditions in a 96 well-plate was added an aqueous solution of EDC (75-300 mM). The turbidity of the sample was measured via UV/Vis spectroscopy and interrupted every 10 min for the next batch of EDC. The dilution of the sample

through the addition of fuel was kept below 8 % and considered negligible.

Microfluidic droplet formation. Surfactant-stabilized water in oil droplets was produced using 1 % 008-FluoroSurfactant in 3M HFE7500 as the oil phase. To form water droplets of varying size, 5 µL of a solution containing Ac-FRGRGRGD-OH, pSS in MES at standard conditions were added to 50 µL of the oil phase in a 200 µL Eppendorf tube. For the preparation of fuel-driven coacervates, DIC was added to the oil phase before the addition of the solution containing Ac-FRGRGRGD-OH and pSS. Snipping of the centrifugal tube resulted in the formation of droplets with a random size distribution. The droplets were imaged at the confocal microscope in untreated observation chambers consisting of a 24 mm x 60 mm glass cover slide and a 16 mm x 16 mm glass cover slide that were separated by two slices of double-sided sticky tape and sealed with two-component glue.

Image analysis. Coacervate-based droplets and coacervate-based spherical shells were analyzed with ImageJ (Fiji). For the analysis, images of coacervate-based droplets were binarized with the moments thresholding algorithm and a gaussian blur was applied. Subsequently, the images were analyzed with the analyze particle plugin in ImageJ, with the option to include or exclude holes. The volume of coacervate-based spherical shells was calculated assuming a spherical shape and considering the half-sphere shape due to wetting of the coacervate droplet between the microfluidic container and oil interface. The volume of coacervate-based droplets without vacuoles was calculated assuming a spherical droplet.

Estimating the concentration of activated building block in the microfluidic container. To validate whether the continuously fueled microfluidic reactor contains a steady-state level of activated building block (anhydride), we chose an indirect quantification method using an HPLC vial. We assumed that the diffusion of fuel (DIC) from the surrounding oil phase into microfluidic droplets smaller than 100 µm in diameter is fast and should be comparable to a two-phase system in an HPLC vial under stirring. For that, we added 250 µL of a mixture containing 10 mM Ac-FRGRGRGD-OH in 200 mM MES buffer at pH 5.3 on top of 250 µL of perfluorinated oil. We started the reaction network by the addition of 0.5 M DIC into the oil phase and continuously stirred the reaction mixture. To determine the concentration of the activated building block, 10 µL of the aqueous phase was quenched with 20 µL of ethylamine (1 M) every 30 min. From preliminary results, we observed that the integral of the resulting amide is constant over the course of more than 2 hr. These results strongly indicate that the concentration of activated building blocks in the microfluidic experiments is constant.

Estimating the concentration of DIC in the microfluidic droplet. To validate whether the continuously fueled microfluidic reactor contains a steady-state level of fuel (DIC), we performed a similar experiment as described in the method *Estimating the concentration of activated building block in the microfluidic container*. Instead of quenching the sample with ethylamine and injecting it into the HPLC, 500 µL of 10 mM Ac-FRGRGRGD-OH in 200 mM MES at pH 5.3 was added to 500 µL HFE 7500 containing 0.5 M DIC in an HPLC vial. The mixture was vortexed for 20 s and left to separate for 1 min. 250 µL of the aqueous solution were then added to 250 µL of quenching solution containing 640 mM borate buffer at pH 10 with 20 vol% D_2O and 80 mM acetonitrile as a standard for the determination of the DIC concentration. The high pH inhibits DIC hydrolysis to ensure that the time until the sample is measured is not influencing the measured DIC concentration. The resulting

DIC integrals were compared with the ACN peak reference. A similar procedure was performed to quantify the waste (DIU) over time. From preliminary results, we observed that the integrals of the resulting DIC and DIU peaks are constant over the course of more than 2 hr. These results strongly indicate that the concentration of DIC in the microfluidic experiments is constant, and that excess of DIU is diffusing into the oil phase.

Chapter 8

Conclusion and outlook

Chemically fueled droplets have gained traction in recent years. As discussed in chapter 1, droplet models are needed to understand better how today's cellular droplets work and to examine the possible role of membrane-less compartments at the origin of life. Efforts have been made to understand the physics behind droplet formation and how to design similar synthetic droplets in the laboratory (see chapter 2). I discussed how these droplets can be regulated and emphasized the role of chemical reactions in controlling their properties. In chapter 3, I outlined what behavior can be expected when droplet building block formation is coupled to a chemical reaction cycle. Importantly, theory-based and experimental work revealed that the localization of the individual reactions plays a crucial role. For instance, numerical simulations predict that chemically fueled droplets can evolve to stable droplet size and even show cycles of self-division and re-growth if the activation and deactivation of droplet building blocks are delocalized into separate phases.

The practical work in this thesis aimed to design a liquid droplet model that is regulated by a chemical reaction cycle. In contrast to previous work from the Boekhoven group based on oil droplets, I wanted to create aqueous droplets where reactions could also take place within the droplets. I screened for peptide sequences that could bind a homo-polymeric RNA to form complex coacervate droplets (see chapter 5). Importantly, a carbodiimide-fueled reaction cycle increases the peptide's affinity for the polyanion and activates it for phase separation. As a result, droplets were formed that closely followed the kinetics of the reaction cycle. Finally, functional RNA could remain in its active folded state inside these droplets. In chapter 6, I included a second polyanion to examine how chemical reactions influence the internal hierarchy of multiphase droplets. In chapter 7, I discussed unpublished work in collaboration with Alexander M. Bergmann. Here, we extended my work from chapters 5 and 6 and developed a method to continuously fuel these droplets. We use this setup to study a non-equilibrium transition of chemically fueled droplets resulting in the formation of spherical shells.

The work presented in this thesis shows one of the first examples of coacervate droplets being regulated by chemical reactions and the first to demonstrate this without the need for enzymes or changes in pH. This droplet model thus fulfills one important aspect that is needed to understand cellular droplets, *i.e.*, their regulation by active processes. The chemical reaction cycle dynamically changes the composition of molecules inside and outside of the droplets whereas a droplet model close to equilibrium inherently retains a fixed position inside the phase diagram. This feature

of chemically fueled droplets led to the discovery of new physics such as irregular self-division and the formation of vacuoles towards the droplets' decay pathway. These morphological transitions can also happen in droplets with multiple phases where chemically fueled droplets have access to regimes inside the phase diagram not possible for droplets close to equilibrium (passive droplets). Excitingly, this work demonstrates that these new regimes can be stabilized in steady-state, *e.g.*, the formation of a vacuole, and the resulting spherical shell. In other words, droplets that are regulated by chemical reactions show disparate behavior in comparison to passive droplets even though the composition of a solution containing chemically fueled droplets is not changing in a steady state. This work represents thus an exciting tool to uncover how active processes regulate droplets in today's cells and potential prebiotic compartments that harbor primitive forms of metabolism where chemical energy is transduced.

Future work needs to examine whether the continuous fueling of these droplets leads to size control and self-division, as predicted by theory. For that, experimental setups need to be developed that consider the propensity of coacervate droplets to fuse which could out-compete the size control mechanism through the chemical reaction cycle. Moreover, future droplet models need to couple active processes to droplet building blocks with a higher degree of complexity. For example, MLOs are composed of hundreds of different molecules which is poorly reflected in complex coacervate droplets made from only one polycation and one polyanion. Also, the components in MLOs do not only assemble through charge-driven interactions but use the full spectrum of supramolecular effects. One exciting research direction that emerged recently is the design of simple coacervates, *i.e.*, molecules that do not need a second binding partner but phase-separate into aqueous droplets on their own. Finally, chemically fueled droplets as protocell models must be designed to exert feedback on molecules and the phase separation process. For example, one could couple the activation of building blocks with the presence of functionalized beads. Droplets would thus compete for the compartmentalization of these solid particles and droplets with beads would have an advantage in starvation periods where fuel is scarce. Also, one could design a reaction that is orthogonal to the chemical reaction cycle, *i.e.*, a polymerization of guest molecules to increase the droplets' stability. Droplets that would take up the necessary components for this second reaction, *e.g.*, an enzyme, could grow faster or become more resilient to changes in the environment. Finally, the compartmentalization of (self-)replicating molecules such as ribozymes into chemically fueled droplets would be an important step towards a self-sustained compartment. Chemically fueled droplets that follow these designs would fulfill the requirements for a protocell model capable of evolution.

Chapter 9

Further publications

Besides the two publications reprinted in chapters 5 and 6 and the review discussed in chapter 3, I contributed to two more publications in the group of Prof. Job Boekhoven. The following section is a full list of my achievements during my Ph.D.

1. Donau, C.; Späth, F.; Sosson, M.; Kriebisch, B. A. K.; Schnitter, F.; Tena-Solsona, M.; Kang, H.-S.; Salibi, E.; Sattler, M.; Mutschler, H.; Boekhoven, J. Active coacervate droplets as a model for membraneless organelles and protocells. *Nat. Commun.* **2020**, *11*, 5167, DOI: 10.1038/s41467-020-18815-9

2. Späth, F.; Donau, C.; Bergmann, A. M.; Kranzlein, M.; Synatschke, C. V.; Rieger, B.; Boekhoven, J. Molecular Design of Chemically Fueled Peptide-Polyelectrolyte Coacervate-Based Assemblies. *J. Am. Chem. Soc.* **2021**, *143*, 4782–4789, DOI: 10.1021/jacs.1c01148

3. Bergmann, A. M.; Donau, C.; Späth, F.; Jahnke, K.; Göpfrich, K.; Boekhoven, J. Evolution and Single-Droplet Analysis of Fuel-Driven Compartments by Droplet-Based Microfluidics. *Angew. Chem. Int. Ed.* **2022**, e202203928, DOI: 10.1002/anie.202203928

4. Donau, C.; Späth, F.; Stasi, M.; Bergmann, A. M.; Boekhoven, J. Phase Transitions in Chemically Fueled, Multiphase Complex Coacervate Droplets. *Angew. Chem. Int. Ed.* **2022**, e202211905, DOI: 10.1002/ange.202211905

5. Donau, C.; Boekhoven, J. The chemistry of chemically fueled droplets. *Trends in Chemistry* **2022**, under review

Chapter 10

Acknowledgements

These four years have passed so rapidly. When looking back at the summer of '69..eh I mean 2018, I had just come back from a trip to South America together with two friends after our master's degree. I had applied for a Ph.D. position in Job Boekhoven's group before the summer but unfortunately, he had already given the open position to another person (thanks Paddi). So here I was sitting in South Italy for three months and writing applications. Not the worst place to do that. And through a strange twist of fate, Job contacted me again after having secured additional funding (he's good at doing that).

So Job, I want to thank you for offering me the position. Looking back, I'm happy to have decided to join your group which had been only about three years old back then. When I started, we didn't know anything about coacervates or membraneless organelles. We didn't have our own confocal. We were merely a group of nine people that had a newly discovered chemical reaction cycle at hand, ready to be implemented. The research idea was simple: Make oil droplets, but with water inside, and let them self-divide. It is still somewhat mesmerizing to me that we accomplished that in only 13 months after I had started. And the reason for this success story is not because I'm particularly great (OK maybe a little), or that I had worked countless hours in the first months to make things that didn't work initially work in the end (for crying out loud), but it was because of several factors that have nothing to do with me.

On the one hand, it was Job's availability and willingness to sit down with me that made me grow as a scientist, ultimately pushing the project. I sincerely thank you for that. On the other hand, there were many group members whom I have shared the lab space and time with, that not only helped me on the science part but made these four years very enjoyable.

I want to thank the first generation of group members that were there when the group started, namely Marta Tena-Solsona, Raphael Grötsch, Caren Wanzke, and Benedikt Rieß. I thank Marta for helpful advice and intriguing group retreat stories, Rapha for taking a big part in setting up the labs, Caren for teaching me the confocal, and Benno for so many things, but foremost being such a relaxed dude, thank you for that!

Furthermore, I thank the second generation of group members that includes myself, namely Fabian Schnitter, Patrick Schwarz, and Kun Dai. I thank Schnitti for all the helpful advice during and after my thesis submission, Paddi for taking care of so many instrument problems and being an awesome lab mate, and Kun for

the countless funny stories that he had brought to the lab and trying to teach me some Chinese, xie xie for that!

Going on with the list, I want to thank the third generation, namely Michaela Würbser, Alexander Bergmann, Laura Tebcharani, Xiaoyao Chen, Michele Stasi, Fabian Späth, and Brigitte & Christine Kriebisch. I thank Michi for the Wrap Wednesday and the Dürüm Donnerstag, Alex for being one of the few who actually drinks and stays late in the evening, as well as countless chess hours that we've spent together (I will get you at some point), Laura for improving the group atmosphere with things such as the tiki bar, Xiaoyao for teaching us (and Kun) how to make a real hot pot, Michele for being a lexicon that I could go to and have my random scientific questions answered, as well as giving me a safe haven where I could let my Italian side blossom, Spabi for bringing some Bavarian culture into the lab as well as introducing the coacervate research topic to the group together with me, Brigitte for having synthesized the first batch of rg3, and Christine for trying to convince me that other interesting building blocks are not meant to make coacervates.

Finally, I want to thank the fourth generation (yes it's a big group now), namely Judit Sastre, Jennifer Rodon-Fores, Anna-Lena Holtmannspötter, Oleksii Zozulia, Monika Wenisch, and Simone Poprawa. I thank Judit for trying endlessly to teach us some basics in statistics and for her Sangria, Jenny for being a great scientific advisor and for bringing lab dog Savanna into our lives, Anna-Lena for being always someone to have a chat with and for her willingness to take over the organization of group events from me, Oleksii for making our research feel a bit more organic chemistry-like, Monika for her exquisite cord-making skills, and Simone for being such a relaxed person with a great sense of humor.

I won't forget the countless lunch hours when we played Schafkopf, our nerf gun fights, and the other smaller or bigger activities that we did over the years. I want to generally thank everyone who got convinced that coacervates are the coolest assemblies to work with, told you so.

Outside of our group, there are many others whom I want to thank. First, I want to thank my committee, Prof. Matthias Feige for agreeing to be the chairman of my examination committee, as well as Prof. Cathleen Zeymer and Prof. Christine Keating for their interest in my work and acceptance to review my thesis.

Second, I want to thank my collaborators who worked with me on many projects. I want to thank Marilyne Sosson for helping me in my first months as a Ph.D. student, both experimentally and growing as a scientist. I thank the Mutschler lab, namely Elia Salibi and Hannes Mutschler, for giving us the biochemical expertise that we truly lacked. Elia, mi raccomando rimani qui intorno e non andare troppo lontano con Claudia. I thank the Sattler group, especially Hyun-Seo Kang and Clara Hipp, for helping me with ITC. I also thank the Weber group, namely Giacomo Bartolucci, Jonathan Baumann, and Christoph Weber for their passionate and ardent monologues about how great phase diagrams are. Moreover, I thank also the members of the Feige and the Lang lab whom I've met over the years. I also want to thank everyone who was part of the CRC235 Emergence of Life. It was just such a great platform for young scientists which helped me to grow as a person, to grow my network, and to enjoy the Ph.D. time as a whole. I also thank all of my friends that helped to distract me outside of the lab. I especially thank Roberto D'Angelo for trying hard to feed me with neuroscience knowledge and correcting my thesis.

Finally and most importantly, I want to thank my family for their support and

helping me to make it this far. Particularly my mum Anna and my brother Conrad. Dziękuję za wszystko, co dla mnie zrobiliście. Wspieraliście mnie we wszystkim, co mi przychodziło do głowy. I want to thank my wife Roberta for her love and support. Grazie amore per esserci stato per tutto questo tempo. Tu sei una parte importante del mio successo.

Chapter 11

References

(1) Wilson, E. B. Structure of protoplasm. *Science* **1899**, *10*, 33–45, DOI: 10.1126/science.10.237.33.

(2) Hardy, W. B. On the structure of cell protoplasm: Part I. The Structure produced in a Cell by Fixative and Post-mortem change. The Structure of Colloidal matter and the Mechanism of Setting and of Coagulation. *J. Physiol.* **1899**, *24*, 158–210, DOI: 10.1113/jphysiol.1899.sp000755.

(3) Brangwynne, C. P.; Eckmann, C. R.; Courson, D. S.; Rybarska, A.; Hoege, C.; Gharakhani, J.; Jülicher, F.; Hyman, A. A. Germline P granules are liquid droplets that localize by controlled dissolution/condensation. *Science* **2009**, *324*, 1729–1732, DOI: 10.1126/science.1172046.

(4) Li, P.; Banjade, S.; Cheng, H.-C.; Kim, S.; Chen, B.; Guo, L.; Llaguno, M.; Hollingsworth, J. V.; King, D. S.; Banani, S. F.; Russo, P. S.; Jiang, Q.-X.; Nixon, B. T.; Rosen, M. K. Phase transitions in the assembly of multivalent signalling proteins. *Nature* **2012**, *483*, 336–340, DOI: 10.1038/nature10879.

(5) Banani, S. F.; Lee, H. O.; Hyman, A. A.; Rosen, M. K. Biomolecular condensates: organizers of cellular biochemistry. *Nat. Rev. Mol. Cell Biol.* **2017**, *18*, 285–298, DOI: 10.1038/nrm.2017.7.

(6) Shin, Y.; Brangwynne, C. P. Liquid phase condensation in cell physiology and disease. *Science* **2017**, *357*, eaaf4382, DOI: 10.1126/science.aaf4382.

(7) Lyon, A. S.; Peeples, W. B.; Rosen, M. K. A framework for understanding the functions of biomolecular condensates across scales. *Nat. Rev. Mol. Cell Biol.* **2021**, *22*, 215–235, DOI: 10.1038/s41580-020-00303-z.

(8) Decker, C. J.; Parker, R. P-bodies and stress granules: possible roles in the control of translation and mRNA degradation. *Cold Spring Harb. Perspect. Biol.* **2012**, *4*, a012286, DOI: 10.1101/cshperspect.a012286.

(9) Protter, D. S. W.; Parker, R. Principles and Properties of Stress Granules. *Trends Cell. Biol.* **2016**, *26*, 668–679, DOI: 10.1016/j.tcb.2016.05.004.

(10) Kedersha, N.; Anderson, P. Mammalian Stress Granules and Processing Bodies. *Meth. Enzymol.* **2007**, *431*, 61–81, DOI: 10.1016/s0076-6879(07)31005-7.

(11) Jain, S.; Wheeler, J. R.; Walters, R. W.; Agrawal, A.; Barsic, A.; Parker, R. ATPase-Modulated Stress Granules Contain a Diverse Proteome and Substructure. *Cell* **2016**, *164*, 487–498, DOI: 10.1016/j.cell.2015.12.038.

(12) Wheeler, J. R.; Matheny, T.; Jain, S.; Abrisch, R.; Parker, R. Distinct stages in stress granule assembly and disassembly. *eLife* **2016**, *5*, e18413, DOI: `10.7554/eLife.18413`.

(13) Feric, M.; Vaidya, N.; Harmon, T. S.; Mitrea, D. M.; Zhu, L.; Richardson, T. M.; Kriwacki, R. W.; Pappu, R. V.; Brangwynne, C. P. Coexisting Liquid Phases Underlie Nucleolar Subcompartments. *Cell* **2016**, *165*, 1686–1697, DOI: `10.1016/j.cell.2016.04.047`.

(14) Correll, C. C.; Bartek, J.; Dundr, M. The Nucleolus: A Multiphase Condensate Balancing Ribosome Synthesis and Translational Capacity in Health, Aging and Ribosomopathies. *Cells* **2019**, *8*, 869, DOI: `10.3390/cells8080869`.

(15) Lafontaine, D. L. J.; Riback, J. A.; Bascetin, R.; Brangwynne, C. P. The nucleolus as a multiphase liquid condensate. *Nat. Rev. Mol. Cell Biol.* **2021**, *22*, 165–182, DOI: `10.1038/s41580-020-0272-6`.

(16) Boisvert, F.-M.; van Koningsbruggen, S.; Navascues, J.; Lamond, A. I. The multifunctional nucleolus. *Nat. Rev. Mol. Cell Biol.* **2007**, *8*, 574–585, DOI: `10.1038/nrm2184`.

(17) Alberti, S.; Hyman, A. A. Biomolecular condensates at the nexus of cellular stress, protein aggregation disease and ageing. *Nat. Rev. Mol. Cell Biol.* **2021**, *22*, 196–213, DOI: `10.1038/s41580-020-00326-6`.

(18) Alberti, S.; Dormann, D. Liquid-Liquid Phase Separation in Disease. *Annu. Rev. Genet.* **2019**, *53*, 171–194, DOI: `10.1146/annurev-genet-112618-043527`.

(19) Nedelsky, N. B.; Taylor, J. P. Bridging biophysics and neurology: aberrant phase transitions in neurodegenerative disease. *Nat. Rev. Neurol.* **2019**, *15*, 272–286, DOI: `10.1038/s41582-019-0157-5`.

(20) Gomes, E.; Shorter, J. The molecular language of membraneless organelles. *J. Biol. Chem.* **2019**, *294*, 7115–7127, DOI: `10.1074/jbc.TM118.001192`.

(21) Snead, W. T.; Gladfelter, A. S. The Control Centers of Biomolecular Phase Separation: How Membrane Surfaces, PTMs, and Active Processes Regulate Condensation. *Mol. Cell* **2019**, *76*, 295–305, DOI: `10.1016/j.molcel.2019.09.016`.

(22) Hondele, M.; Heinrich, S.; De Los Rios, P.; Weis, K. Membraneless organelles: phasing out of equilibrium. *Emerg. Top Life Sci.* **2020**, *4*, 343–354, DOI: `10.1042/ETLS20190190`.

(23) Saito, M.; Hess, D.; Eglinger, J.; Fritsch, A. W.; Kreysing, M.; Weinert, B. T.; Choudhary, C.; Matthias, P. Acetylation of intrinsically disordered regions regulates phase separation. *Nat. Chem. Biol.* **2019**, *15*, 51–61, DOI: `10.1038/s41589-018-0180-7`.

(24) Kim, T. H.; Tsang, B.; Vernon, R. M.; Sonenberg, N.; Kay, L. E.; Forman-Kay, J. D. Phospho-dependent phase separation of FMRP and CAPRIN1 recapitulates regulation of translation and deadenylation. *Science* **2019**, *365*, 825–829, DOI: `10.1126/science.aax4240`.

(25) Tanikawa, C.; Ueda, K.; Suzuki, A.; Iida, A.; Nakamura, R.; Atsuta, N.; Tohnai, G.; Sobue, G.; Saichi, N.; Momozawa, Y.; Kamatani, Y.; Kubo, M.; Yamamoto, K.; Nakamura, Y.; Matsuda, K. Citrullination of RGG Motifs in FET Proteins by PAD4 Regulates Protein Aggregation and ALS Susceptibility. *Cell Rep* **2018**, *22*, 1473–1483, DOI: 10.1016/j.celrep.2018.01.031.

(26) Greening, C.; Lithgow, T. Formation and function of bacterial organelles. *Nat. Rev. Microbiol.* **2020**, *18*, 677–689, DOI: 10.1038/s41579-020-0413-0.

(27) Oparin, A. I. *Origin of life*, MacMillan, New York, 1938.

(28) Haldane, J. B. S. The origin of life. *Rationalist Annual* **1929**, *148*, 3–10.

(29) Bungenberg de Jong, H.; Kruyt, H. Coacervation (partial miscibility in colloid systems). *Proc. K. Ned. Akad. Wet.* **1929**, *32*, 849–856.

(30) Evreinova, T. N.; Karnaukhov, W. N.; Mamontova, T. W.; Ivanizki, G. R. The interaction of biological macromolecules in coacervate systems. *J. Colloid Interface Sci.* **1971**, *36*, 18–23, DOI: 10.1016/0021-9797(71)90236-0.

(31) Evreinova, T.; Mamontova, T.; Karnauhov, V.; Stephanov, S.; Hrust, U. Coacervate Systems and Origin of Life. *In Cosmochemical Evolution and the Origins of Life*, Eds.: Oró, J., Miller, S.L., Ponnamperuma, C., Young, R.S., Springer: Dordrecht, 1974, 201–205, DOI: 10.1007/978-94-015-1118-6_15.

(32) Ghosh, B.; Bose, R.; Tang, T.-Y. D. Can coacervation unify disparate hypotheses in the origin of cellular life? *Curr. Opin. Colloid Interface Sci.* **2021**, *52*, 101415, DOI: 10.1016/j.cocis.2020.101415.

(33) Oparin, A. I.; Gladilin, K. L. Evolution of self-assembly of probionts. *BioSystems* **1980**, *12*, 133–145, DOI: 10.1016/0303-2647(80)90011-8.

(34) Lazcano, A. Historical development of origins research. *Cold Spring Harb. Perspect. Biol.* **2010**, *2*, a002089, DOI: 10.1101/cshperspect.a002089.

(35) Crowe, C. D.; Keating, C. D. Liquid-liquid phase separation in artificial cells. *Interface Focus* **2018**, *8*, 20180032, DOI: 10.1098/rsfs.2018.0032.

(36) Sing, C. E.; Perry, S. L. Recent progress in the science of complex coacervation. *Soft Matter* **2020**, *16*, 2885–2914, DOI: 10.1039/d0sm00001a.

(37) Abbas, M.; Lipiński, W. P.; Wang, J.; Spruijt, E. Peptide-based coacervates as biomimetic protocells. *Chem. Soc. Rev.* **2021**, *50*, 3690–3705, DOI: 10.1039/d0cs00307g.

(38) Koga, S.; Williams, D. S.; Perriman, A. W.; Mann, S. Peptide-nucleotide microdroplets as a step towards a membrane-free protocell model. *Nat. Chem.* **2011**, *3*, 720–724, DOI: 10.1038/nchem.1110.

(39) Drobot, B.; Iglesias-Artola, J. M.; Le Vay, K.; Mayr, V.; Kar, M.; Kreysing, M.; Mutschler, H.; Tang, T.-Y. D. Compartmentalised RNA catalysis in membrane-free coacervate protocells. *Nat. Commun.* **2018**, *9*, 3643, DOI: 10.1038/s41467-018-06072-w.

(40) Pressman, A.; Blanco, C.; Chen, I. A. The RNA World as a Model System to Study the Origin of Life. *Curr. Biol.* **2015**, *25*, R953–R963, DOI: 10.1016/j.cub.2015.06.016.

(41) Poudyal, R. R.; Guth-Metzler, R. M.; Veenis, A. J.; Frankel, E. A.; Keating, C. D.; Bevilacqua, P. C. Template-directed RNA polymerization and enhanced ribozyme catalysis inside membraneless compartments formed by coacervates. *Nat. Commun.* **2019**, *10*, 490, DOI: 10.1038/s41467-019-08353-4.

(42) Sokolova, E.; Spruijt, E.; Hansen, M. M.; Dubuc, E.; Groen, J.; Chokkalingam, V.; Piruska, A.; Heus, H. A.; Huck, W. T. Enhanced transcription rates in membrane-free protocells formed by coacervation of cell lysate. *Proc. Natl. Acad. Sci. U.S.A.* **2013**, *110*, 11692–11697, DOI: 10.1073/pnas.1222321110.

(43) Tang, T.-Y. D.; van Swaay, D.; deMello, A.; Ross Anderson, J. L.; Mann, S. In vitro gene expression within membrane-free coacervate protocells. *Chem. Commun.* **2015**, *51*, 11429–11432, DOI: 10.1039/c5cc04220h.

(44) Küffner, A. M.; Prodan, M.; Zuccarini, R.; Capasso Palmiero, U.; Faltova, L.; Arosio, P. Acceleration of an Enzymatic Reaction in Liquid Phase Separated Compartments Based on Intrinsically Disordered Protein Domains. *ChemSystemsChem* **2020**, *2*, e200000, DOI: 10.1002/syst.202000001.

(45) Brangwynne, C. P.; Tompa, P.; Pappu, R. V. Polymer physics of intracellular phase transitions. *Nat. Phys.* **2015**, *11*, 899–904, DOI: 10.1038/nphys3532.

(46) Alberti, S.; Gladfelter, A.; Mittag, T. Considerations and Challenges in Studying Liquid-Liquid Phase Separation and Biomolecular Condensates. *Cell* **2019**, *176*, 419–434, DOI: 10.1016/j.cell.2018.12.035.

(47) Hyman, A. A.; Weber, C. A.; Jülicher, F. Liquid-liquid phase separation in biology. *Annu. Rev. Cell Dev. Biol.* **2014**, *30*, 39–58, DOI: 10.1146/annurev-cellbio-100913-013325.

(48) Boeynaems, S.; Alberti, S.; Fawzi, N. L.; Mittag, T.; Polymenidou, M.; Rousseau, F.; Schymkowitz, J.; Shorter, J.; Wolozin, B.; Van Den Bosch, L.; Tompa, P.; Fuxreiter, M. Protein Phase Separation: A New Phase in Cell Biology. *Trends Cell Biol.* **2018**, *28*, 420–435, DOI: 10.1016/j.tcb.2018.02.004.

(49) Van der Gucht, J.; Spruijt, E.; Lemmers, M.; Cohen Stuart, M. A. Polyelectrolyte complexes: bulk phases and colloidal systems. *J. Colloid Interface Sci.* **2011**, *361*, 407–422, DOI: 10.1016/j.jcis.2011.05.080.

(50) Srivastava, S.; Tirrell, M. V. Polyelectrolyte complexation. *Adv. Chem. Phys.* **2016**, *161*, 499–544, DOI: 10.1002/9781119290971.ch7.

(51) Yewdall, N. A.; André, A. A. M.; Lu, T.; Spruijt, E. Coacervates as models of membraneless organelles. *Curr. Opin. Colloid Interface Sci.* **2021**, *52*, DOI: 10.1016/j.cocis.2020.101416.

(52) Aumiller W. M., J.; Pir Cakmak, F.; Davis, B. W.; Keating, C. D. RNA-Based Coacervates as a Model for Membraneless Organelles: Formation, Properties, and Interfacial Liposome Assembly. *Langmuir* **2016**, *32*, 10042–10053, DOI: 10.1021/acs.langmuir.6b02499.

(53) Faltova, L.; Küffner, A. M.; Hondele, M.; Weis, K.; Arosio, P. Multifunctional Protein Materials and Microreactors using Low Complexity Domains as Molecular Adhesives. *ACS Nano* **2018**, *12*, 9991–9999, DOI: 10.1021/acsnano.8b04304.

(54) Schuster, B. S.; Reed, E. H.; Parthasarathy, R.; Jahnke, C. N.; Caldwell, R. M.; Bermudez, J. G.; Ramage, H.; Good, M. C.; Hammer, D. A. Controllable protein phase separation and modular recruitment to form responsive membraneless organelles. *Nat. Commun.* **2018**, *9*, 2985, DOI: 10.1038/s41467-018-05403-1.

(55) Abbas, M.; Lipiński, W. P.; Nakashima, K. K.; Huck, W. T. S.; Spruijt, E. A short peptide synthon for liquid-liquid phase separation. *Nat. Chem.* **2021**, *13*, 1046–1054, DOI: 10.1038/s41557-021-00788-x.

(56) Sun, Y.; Lau, S. Y.; Lim, Z. W.; Chang, S. C.; Ghadessy, F.; Partridge, A.; Miserez, A. Phase-separating peptides for direct cytosolic delivery and redox-activated release of macromolecular therapeutics. *Nat. Chem.* **2022**, *14*, 274–283, DOI: 10.1038/s41557-021-00854-4.

(57) Fu, J.; Schlenoff, J. B. Driving Forces for Oppositely Charged Polyion Association in Aqueous Solutions: Enthalpic, Entropic, but Not Electrostatic. *J. Am. Chem. Soc.* **2016**, *138*, 980–990, DOI: 10.1021/jacs.5b11878.

(58) Flory, P. J. *Principles of Polymer Chemistry*, Cornell University Press, Ithaca, NY, 1953.

(59) Debye, P.; Hückel, E. Zur Theorie der Elektrolyte. *Phys. Z.* **1923**, *24*, 185.

(60) Michaeli, I.; Overbeek, J. T. G.; Voorn, M. J. Phase Separation of Polyelectrolyte Solutions. *J. Polym. Sci.* **1957**, *23*, 443–450, DOI: 10.1002/pol.1957.1202310337.

(61) Overbeek, J. T. G.; Voorn, M. J. Phase separation in polyelectrolyte solutions. Theory of complex coacervation. *J. Cell. Comp. Physiol.* **1957**, *49*, 7–26, DOI: 10.1002/jcp.1030490404.

(62) Biesheuvel, P. M.; Cohen Stuart, M. A. Electrostatic free energy of interacting ionizable double layers. *Langmuir* **2004**, *20*, 4764–4770, DOI: 10.1016/j.jcis.2004.02.069.

(63) Veis, A. Phase separation in polyelectrolyte solutions. II. Interaction effects. *J. Phys. Chem.* **1961**, *65*, 1798–1803, DOI: 10.1021/j100827a026.

(64) Blocher, W. C.; Perry, S. L. Complex coacervate-based materials for biomedicine. *Wiley Interdiscip. Rev. Nanomed. Nanobiotechnol.* **2017**, *9*, e1442, DOI: 10.1002/wnan.1442.

(65) Spruijt, E.; Westphal, A. H.; Borst, J. W.; Cohen Stuart, M. A.; van der Gucht, J. Binodal Compositions of Polyelectrolyte Complexes. *Macromolecules* **2010**, *43*, 6476–6484, DOI: 10.1021/ma101031t.

(66) Tian, L.; Martin, N.; Bassindale, P. G.; Patil, A. J.; Li, M.; Barnes, A.; Drinkwater, B. W.; Mann, S. Spontaneous assembly of chemically encoded two-dimensional coacervate droplet arrays by acoustic wave patterning. *Nat. Commun.* **2016**, *7*, 13068, DOI: 10.1038/ncomms13068.

(67) Chollakup, R.; Smitthipong, W.; Eisenbach, C. D.; Tirrell, M. Phase Behavior and Coacervation of Aqueous Poly(acrylic acid)Poly(allylamine) Solutions. *Macromolecules* **2010**, *43*, 2518–2528, DOI: 10.1021/ma902144k.

(68) Spruijt, E.; Sprakel, J.; Cohen Stuart, M. A.; van der Gucht, J. Interfacial tension between a complex coacervate phase and its coexisting aqueous phase. *Soft Matter* **2010**, *6*, 172–178, DOI: 10.1039/b911541b.

(69) Fares, H. M.; Marras, A. E.; Ting, J. M.; Tirrell, M. V.; Keating, C. D. Impact of wet-dry cycling on the phase behavior and compartmentalization properties of complex coacervates. *Nat. Commun.* **2020**, *11*, 5423, DOI: 10.1038/s41467-020-19184-z.

(70) De Kruif, C. G.; Weinbreck, F.; de Vries, R. Complex coacervation of proteins and anionic polysaccharides. *Curr. Opin. Colloid Interface Sci.* **2004**, *9*, 340–349, DOI: 10.1016/j.cocis.2004.09.006.

(71) Turgeon, S. L.; Schmitt, C.; Sanchez, C. Protein–polysaccharide complexes and coacervates. *Curr. Opin. Colloid Interface Sci.* **2007**, *12*, 166–178, DOI: 10.1016/j.cocis.2007.07.007.

(72) Aumiller W. M., J.; Keating, C. D. Phosphorylation-mediated RNA/peptide complex coacervation as a model for intracellular liquid organelles. *Nat. Chem.* **2016**, *8*, 129–137, DOI: 10.1038/nchem.2414.

(73) Priftis, D.; Tirrell, M. Phase behaviour and complex coacervation of aqueous polypeptide solutions. *Soft Matter* **2012**, *8*, 9396–9405, DOI: 10.1039/c2sm25604e.

(74) Priftis, D.; Megley, K.; Laugel, N.; Tirrell, M. Complex coacervation of poly(ethylene-imine)/polypeptide aqueous solutions: thermodynamic and rheological characterization. *J. Colloid Interface Sci.* **2013**, *398*, 39–50, DOI: 10.1016/j.jcis.2013.01.055.

(75) Cakmak, F. P.; Choi, S.; Meyer, M. O.; Bevilacqua, P. C.; Keating, C. D. Prebiotically-relevant low polyion multivalency can improve functionality of membraneless compartments. *Nat. Commun.* **2020**, *11*, 5949, DOI: 10.1038/s41467-020-19775-w.

(76) Jain, A.; Vale, R. D. RNA phase transitions in repeat expansion disorders. *Nature* **2017**, *546*, 243–247, DOI: 10.1038/nature22386.

(77) Merindol, R.; Loescher, S.; Samanta, A.; Walther, A. Pathway-controlled formation of mesostructured all-DNA colloids and superstructures. *Nat. Nanotechnol.* **2018**, *13*, 730–738, DOI: 10.1038/s41565-018-0168-1.

(78) Fanalista, F.; Deshpande, S.; Lau, A.; Pawlik, G.; Dekker, C. FtsZ-Induced Shape Transformation of Coacervates. *Adv. Biosyst.* **2018**, *2*, 1800136, DOI: 10.1002/adbi.201800136.

(79) Monterroso, B.; Zorrilla, S.; Sobrinos-Sanguino, M.; Robles-Ramos, M. A.; López-Álvarez, M.; Margolin, W.; Keating, C. D.; Rivas, G. Bacterial FtsZ protein forms phase-separated condensates with its nucleoid-associated inhibitor SlmA. *EMBO Rep.* **2019**, *20*, e45946, DOI: 10.15252/embr.201845946.

(80) Te Brinke, E.; Groen, J.; Herrmann, A.; Heus, H. A.; Rivas, G.; Spruijt, E.; Huck, W. T. S. Dissipative adaptation in driven self-assembly leading to self-dividing fibrils. *Nat. Nanotechnol.* **2018**, *13*, 849–855, DOI: 10.1038/s41565-018-0192-1.

113

(81) Nott, T. J.; Craggs, T. D.; Baldwin, A. J. Membraneless organelles can melt nucleic acid duplexes and act as biomolecular filters. *Nat. Chem.* **2016**, *8*, 569–575, DOI: 10.1038/nchem.2519.

(82) Elbaum-Garfinkle, S.; Kim, Y.; Szczepaniak, K.; Chen, C. C.; Eckmann, C. R.; Myong, S.; Brangwynne, C. P. The disordered P granule protein LAF-1 drives phase separation into droplets with tunable viscosity and dynamics. *Proc. Natl. Acad. Sci. U.S.A.* **2015**, *112*, 7189–7194, DOI: 10.1073/pnas.1504822112.

(83) Kayitmazer, A. B.; Seeman, D.; Minsky, B. B.; Dubin, P. L.; Xu, Y. Protein–polyelectrolyte interactions. *Soft Matter* **2013**, *9*, 2553–2583, DOI: 10.1039/c2sm27002a.

(84) Horn, J. M.; Kapelner, R. A.; Obermeyer, A. C. Macro- and Microphase Separated Protein-Polyelectrolyte Complexes: Design Parameters and Current Progress. *Polymers* **2019**, *11*, 578, DOI: 10.3390/polym11040578.

(85) Chuanoi, S.; Anraku, Y.; Hori, M.; Kishimura, A.; Kataoka, K. Fabrication of polyion complex vesicles with enhanced salt and temperature resistance and their potential applications as enzymatic nanoreactors. *Biomacromolecules* **2014**, *15*, 2389–2397, DOI: 10.1021/bm500127g.

(86) Magana, J. R.; Sproncken, C. C. M.; Voets, I. K. On Complex Coacervate Core Micelles: Structure-Function Perspectives. *Polymers* **2020**, *12*, 1953, DOI: 10.3390/polym12091953.

(87) Liu, Y.; Winter, H. H.; Perry, S. L. Linear viscoelasticity of complex coacervates. *Adv. Colloid Interface Sci.* **2017**, *239*, 46–60, DOI: 10.1016/j.cis.2016.08.010.

(88) Perry, S. L.; Li, Y.; Priftis, D.; Leon, L.; Tirrell, M. The Effect of Salt on the Complex Coacervation of Vinyl Polyelectrolytes. *Polymers* **2014**, *6*, 1756–1772, DOI: 10.3390/polym6061756.

(89) Gallivan, J. P.; Dougherty, D. A. Cation-π interactions in structural biology. *Proc. Natl. Acad. Sci. U.S.A.* **1999**, *96*, 9459–9464, DOI: 10.1073/pnas.96.17.9459.

(90) Fisher, R. S.; Elbaum-Garfinkle, S. Tunable multiphase dynamics of arginine and lysine liquid condensates. *Nat. Commun.* **2020**, *11*, 4628, DOI: 10.1038/s41467-020-18224-y.

(91) Tsuchida, E. Formation of Polyelectrolyte Complexes and Their Structures. *J. Macromol. Sci. A* **1994**, *31*, 1–15, DOI: 10.1080/10601329409349713.

(92) Kudlay, A.; Ermoshkin, A. V.; Olvera de La Cruz, M. Complexation of oppositely charged polyelectrolytes: effect of ion pair formation. *Macromolecules* **2004**, *37*, 9231–9241, DOI: 10.1021/ma048519t.

(93) Schmitt, C.; Turgeon, S. L. Protein/polysaccharide complexes and coacervates in food systems. *Adv. Colloid Interface Sci.* **2011**, *167*, 63–70, DOI: 10.1016/j.cis.2010.10.001.

(94) Bohidar, H.; Dubin, P. L.; Majhi, P. R.; Tribet, C.; Jaeger, W. Effects of protein polyelectrolyte affinity and polyelectrolyte molecular weight on dynamic properties of bovine serum albumin poly (diallyldimethylammonium chloride) coacervates. *Biomacromolecules* **2005**, *6*, 1573–1585, DOI: 10.1021/bm049174p.

(95) Antonov, M.; Mazzawi, M.; Dubin, P. L. Entering and exiting the protein polyelectrolyte coacervate phase via nonmonotonic salt dependence of critical conditions. *Biomacromolecules* **2010**, *11*, 51–59, DOI: 10.1021/bm900886k.

(96) Cheng, S. Z. D. *Phase transitions in polymers: the role of metastable states*, Elsevier, Amsterdam, 2008.

(97) Martin, N.; Sharma, K. P.; Harniman, R. L.; Richardson, R. M.; Hutchings, R. J.; Alibhai, D.; Li, M.; Mann, S. Light-induced dynamic shaping and self-division of multipodal polyelectrolyte-surfactant microarchitectures via azobenzene photomechanics. *Sci. Rep.* **2017**, *7*, 1–12, DOI: 10.1038/srep41327.

(98) Martin, N.; Tian, L.; Spencer, D.; Coutable-Pennarun, A.; Anderson, J. L. R.; Mann, S. Photoswitchable Phase Separation and Oligonucleotide Trafficking in DNA Coacervate Microdroplets. *Angew. Chem. Int. Ed.* **2019**, *58*, 14594–14598, DOI: 10.1002/anie.201909228.

(99) Wee, W. A.; Sugiyama, H.; Park, S. Photoswitchable single-stranded DNA-peptide coacervate formation as a dynamic system for reaction control. *iScience* **2021**, *24*, 103455, DOI: 10.1016/j.isci.2021.103455.

(100) Merindol, R.; Martin, N.; Beneyton, T.; Baret, J.-C.; Ravaine, S. Fast and Ample Light Controlled Actuation of Monodisperse All-DNA Microgels. *Adv. Funct. Mater.* **2021**, *31*, 2010396, DOI: 10.1002/adfm.202010396.

(101) Reed, E. H.; Hammer, D. A. Redox sensitive protein droplets from recombinant oleosin. *Soft Matter* **2018**, *14*, 6506–6513, DOI: 10.1039/c8sm01047a.

(102) Matsuo, M.; Kurihara, K. Proliferating coacervate droplets as the missing link between chemistry and biology in the origins of life. *Nat. Commun.* **2021**, *12*, 5487, DOI: 10.1038/s41467-021-25530-6.

(103) Garenne, D.; Beven, L.; Navailles, L.; Nallet, F.; Dufourc, E. J.; Douliez, J. P. Sequestration of Proteins by Fatty Acid Coacervates for Their Encapsulation within Vesicles. *Angew. Chem. Int. Ed.* **2016**, *55*, 13475–13479, DOI: 10.1002/anie.201607117.

(104) Douliez, J. P.; Martin, N.; Gaillard, C.; Beneyton, T.; Baret, J. C.; Mann, S.; Beven, L. Catanionic Coacervate Droplets as a Surfactant-Based Membrane-Free Protocell Model. *Angew. Chem. Int. Ed.* **2017**, *56*, 13689–13693, DOI: 10.1002/anie.201707139.

(105) Martin, N.; Douliez, J. P.; Qiao, Y.; Booth, R.; Li, M.; Mann, S. Antagonistic chemical coupling in self-reconfigurable host-guest protocells. *Nat. Commun.* **2018**, *9*, 3652, DOI: 10.1038/s41467-018-06087-3.

(106) Cingil, H. E.; Meertens, N. C. H.; Voets, I. K. Temporally Programmed Disassembly and Reassembly of C3Ms. *Small* **2018**, *14*, 1802089, DOI: 10.1002/smll.201802089.

(107) Karoui, H.; Seck, M. J.; Martin, N. Self-programmed enzyme phase separation and multiphase coacervate droplet organization. *Chem. Sci.* **2021**, *12*, 2794–2802, DOI: 10.1039/d0sc06418a.

(108)   Banerjee, P. R.; Milin, A. N.; Moosa, M. M.; Onuchic, P. L.; Deniz, A. A. Reentrant Phase Transition Drives Dynamic Substructure Formation in Ribonucleoprotein Droplets. *Angew. Chem. Int. Ed.* **2017**, *56*, 11354–11359, DOI: 10.1002/anie.201703191.

(109)   Nakashima, K. K.; Baaij, J. F.; Spruijt, E. Reversible generation of coacervate droplets in an enzymatic network. *Soft Matter* **2018**, *14*, 361–367, DOI: 10.1039/c7sm01897e.

(110)   Yang, S.; Li, B.; Wu, C.; Xu, W.; Tu, M.; Yan, Y.; Huang, J.; Drechsler, M.; Granick, S.; Jiang, L. Steering Coacervation by a Pair of Broad-Spectrum Regulators. *ACS Nano* **2019**, *13*, 2420–2426, DOI: 10.1021/acsnano.8b09332.

(111)   Deshpande, S.; Brandenburg, F.; Lau, A.; Last, M. G. F.; Spoelstra, W. K.; Reese, L.; Wunnava, S.; Dogterom, M.; Dekker, C. Spatiotemporal control of coacervate formation within liposomes. *Nat. Commun.* **2019**, *10*, 1800, DOI: 10.1038/s41467-019-09855-x.

(112)   Spoelstra, W. K.; van der Sluis, E. O.; Dogterom, M.; Reese, L. Nonspherical Coacervate Shapes in an Enzyme-Driven Active System. *Langmuir* **2020**, *36*, 1956–1964, DOI: 10.1021/acs.langmuir.9b02719.

(113)   Zhou, L.; Fan, Y.; Liu, Z.; Chen, L.; Spruijt, E.; Wang, Y. A Multiresponsive Transformation between Surfactant-Based Coacervates and Vesicles. *CCS Chem.* **2021**, *3*, 358–366, DOI: 10.31635/ccschem.021.202000702.

(114)   Nakashima, K. K.; van Haren, M. H. I.; André, A. A. M.; Robu, I.; Spruijt, E. Active coacervate droplets are protocells that grow and resist Ostwald ripening. *Nat. Commun.* **2021**, *12*, 3819, DOI: 10.1038/s41467-021-24111-x.

(115)   Shimokuri, T.; Kaneko, T.; Akashi, M. Effects of thermoresponsive coacervation on the hydrolytic degradation of amphipathic poly(gamma-glutamate)s. *Macromol. Biosci.* **2006**, *6*, 942–951, DOI: 10.1002/mabi.200600183.

(116)   Ding, Y.; Zhao, Q.; Wang, L.; Huang, L.; Liu, Q.; Lu, X.; Cai, Y. Polymerization-Induced Self-Assembly Promoted by Liquid-Liquid Phase Separation. *ACS Macro. Lett.* **2019**, *8*, 943–946, DOI: 10.1021/acsmacrolett.9b00435.

(117)   Jia, T. Z.; Chandru, K.; Hongo, Y.; Afrin, R.; Usui, T.; Myojo, K.; Cleaves H. J., 2. Membraneless polyester microdroplets as primordial compartments at the origins of life. *Proc. Natl. Acad. Sci. U.S.A.* **2019**, *116*, 15830–15835, DOI: 10.1073/pnas.1902336116.

(118)   Mountain, G. A.; Keating, C. D. Formation of Multiphase Complex Coacervates and Partitioning of Biomolecules within them. *Biomacromolecules* **2020**, *21*, 630–640, DOI: 10.1021/acs.biomac.9b01354.

(119)   Lu, T.; Spruijt, E. Multiphase Complex Coacervate Droplets. *J. Am. Chem. Soc.* **2020**, *142*, 2905–2914, DOI: 10.1021/jacs.9b11468.

(120)   Boeynaems, S.; Holehouse, A. S.; Weinhardt, V.; Kovacs, D.; Van Lindt, J.; Larabell, C.; Van Den Bosch, L.; Das, R.; Tompa, P. S.; Pappu, R. V.; Gitler, A. D. Spontaneous driving forces give rise to protein-RNA condensates with coexisting phases and complex material properties. *Proc. Natl. Acad. Sci. U.S.A.* **2019**, *116*, 7889–7898, DOI: 10.1073/pnas.1821038116.

(121) Simon, J. R.; Carroll, N. J.; Rubinstein, M.; Chilkoti, A.; López, G. P. Programming molecular self-assembly of intrinsically disordered proteins containing sequences of low complexity. *Nat. Chem.* **2017**, *9*, 509–515, DOI: 10.1038/nchem.2715.

(122) Chen, Y.; Yuan, M.; Zhang, Y.; Liu, S.; Yang, X.; Wang, K.; Liu, J. Construction of coacervate-in-coacervate multi-compartment protocells for spatial organization of enzymatic reactions. *Chem. Sci.* **2020**, *11*, 8617–8625, DOI: 10.1039/d0sc03849k.

(123) Moreau, N. G.; Martin, N.; Gobbo, P.; Tang, T.-Y. D.; Mann, S. Spontaneous membrane-less multi-compartmentalization via aqueous two-phase separation in complex coacervate micro-droplets. *Chem. Commun.* **2020**, *56*, 12717–12720, DOI: 10.1039/d0cc05399f.

(124) Kaur, T.; Raju, M.; Alshareedah, I.; Davis, R. B.; Potoyan, D. A.; Banerjee, P. R. Sequence-encoded and composition-dependent protein-RNA interactions control multiphasic condensate morphologies. *Nat. Commun.* **2021**, *12*, 872, DOI: 10.1038/s41467-021-21089-4.

(125) Choi, S.; Meyer, M. O.; Bevilacqua, P. C.; Keating, C. D. Phase-specific RNA accumulation and duplex thermodynamics in multiphase coacervate models for membraneless organelles. *Nat. Chem.* **2022**, *14*, 1110–1117, DOI: 10.1038/s41557-022-00980-7.

(126) Donau, C.; Boekhoven, J. The chemistry of chemically fueled droplets. *Trends in Chemistry* **2022**, under review.

(127) Rieß, B.; Grötsch, R. K.; Boekhoven, J. The Design of Dissipative Molecular Assemblies Driven by Chemical Reaction Cycles. *Chem* **2020**, *6*, 552–578, DOI: 10.1016/j.chempr.2019.11.008.

(128) Zwicker, D.; Hyman, A. A.; Jülicher, F. Suppression of Ostwald ripening in active emulsions. *Phys. Rev. E Stat. Nonlin. Soft Matter Phys.* **2015**, *92*, 012317, DOI: 10.1103/PhysRevE.92.012317.

(129) Wurtz, J. D.; Lee, C. F. Chemical-Reaction-Controlled Phase Separated Drops: Formation, Size Selection, and Coarsening. *Phys. Rev. Lett.* **2018**, *120*, 078102, DOI: 10.1103/PhysRevLett.120.078102.

(130) Weber, C. A.; Zwicker, D.; Jülicher, F.; Lee, C. F. Physics of active emulsions. *Rep. Prog. Phys.* **2019**, *82*, 064601, DOI: 10.1088/1361-6633/ab052b.

(131) Zwicker, D.; Seyboldt, R.; Weber, C. A.; Hyman, A. A.; Jülicher, F. Growth and division of active droplets provides a model for protocells. *Nat. Phys.* **2017**, *13*, 408–413, DOI: 10.1038/nphys3984.

(132) Seyboldt, R.; Jülicher, F. Role of hydrodynamic flows in chemically driven droplet division. *New J. Phys.* **2018**, *20*, 105010, DOI: 10.1088/1367-2630/aae735.

(133) Tena-Solsona, M.; Janssen, J.; Wanzke, C.; Schnitter, F.; Park, H.; Rieß, B.; Gibbs, J. M.; Weber, C. A.; Boekhoven, J. Accelerated ripening in chemically fueled emulsions. *ChemSystemsChem* **2021**, *3*, e2000034, DOI: 10.1002/syst.202000034.

(134) Illien, P.; Golestanian, R.; Sen, A. 'Fuelled' motion: phoretic motility and collective behaviour of active colloids. *Chem. Soc. Rev.* **2017**, *46*, 5508–5518, DOI: 10.1039/c7cs00087a.

(135) Meredith, C. H.; Castonguay, A. C.; Chiu, Y. J.; Brooks, A. M.; Moerman, P. G.; Torab, P.; Wong, K.; Sen, A.; Velegol, D.; Zarzar, L. D. Chemical design of self-propelled Janus droplet. *Matter* **2022**, *5*, 616–633, DOI: 10.1016/j.matt.2021.12.014.

(136) Zwicker, D. The intertwined physics of active chemical reactions and phase separation. *Curr. Opin. Colloid Interface Sci.* **2022**, *61*, 101606, DOI: 10.1016/j.cocis.2022.101606.

(137) Golestanian, R. Division for multiplication. *Nat. Phys.* **2017**, *13*, 323–324, DOI: 10.1038/nphys3998.

(138) Mukherjee, A.; Lutkenhaus, J. Dynamic assembly of FtsZ regulated by GTP hydrolysis. *EMBO J.* **1998**, *17*, 462–469, DOI: 10.1093/emboj/17.2.462.

(139) Donau, C.; Späth, F.; Sosson, M.; Kriebisch, B. A. K.; Schnitter, F.; Tena-Solsona, M.; Kang, H.-S.; Salibi, E.; Sattler, M.; Mutschler, H.; Boekhoven, J. Active coacervate droplets as a model for membraneless organelles and protocells. *Nat. Commun.* **2020**, *11*, 5167, DOI: 10.1038/s41467-020-18815-9.

(140) Bergmann, A. M.; Donau, C.; Späth, F.; Jahnke, K.; Göpfrich, K.; Boekhoven, J. Evolution and Single-Droplet Analysis of Fuel-Driven Compartments by Droplet-Based Microfluidics. *Angew. Chem. Int. Ed.* **2022**, e202203928, DOI: 10.1002/anie.202203928.

(141) Späth, F.; Donau, C.; Bergmann, A. M.; Kränzlein, M.; Synatschke, C. V.; Rieger, B.; Boekhoven, J. Molecular Design of Chemically Fueled Peptide-Polyelectrolyte Coacervate-Based Assemblies. *J. Am. Chem. Soc.* **2021**, *143*, 4782–4789, DOI: 10.1021/jacs.1c01148.

(142) Zwicker, D.; Decker, M.; Jaensch, S.; Hyman, A. A.; Jülicher, F. Centrosomes are autocatalytic droplets of pericentriolar material organized by centrioles. *Proc. Natl. Acad. Sci. U.S.A.* **2014**, *111*, E2636–E2645, DOI: 10.1073/pnas.1404855111.

(143) Zwicker, D.; Baumgart, J.; Redemann, S.; Müller-Reichert, T.; Hyman, A. A.; Jülicher, F. Positioning of Particles in Active Droplets. *Phys. Rev. Lett.* **2018**, *121*, 158102, DOI: 10.1103/PhysRevLett.121.158102.

(144) Decker, M.; Jaensch, S.; Pozniakovsky, A.; Zinke, A.; O'Connell, K. F.; Zachariae, W.; Myers, E.; Hyman, A. A. Limiting amounts of centrosome material set centrosome size in C. elegans embryos. *Curr. Biol.* **2011**, *21*, 1259–1267, DOI: 10.1016/j.cub.2011.06.002.

(145) Woodruff, J. B. The material state of centrosomes: lattice, liquid, or gel? *Curr. Opin. Struct. Biol.* **2021**, *66*, 139–147, DOI: 10.1016/j.sbi.2020.10.001.

(146) Tena-Solsona, M.; Wanzke, C.; Rieß, B.; Bausch, A. R.; Boekhoven, J. Self-selection of dissipative assemblies driven by primitive chemical reaction networks. *Nat. Commun.* **2018**, *9*, 2044, DOI: 10.1038/s41467-018-04488-y.

(147) Wanzke, C.; Tena-Solsona, M.; Rieß, B.; Tebcharani, L.; Boekhoven, J. Active droplets in a hydrogel release drugs with a constant and tunable rate. *Mater. Horiz.* **2020**, *7*, 1397–1403, DOI: 10.1039/c9mh01822k.

(148) Tena-Solsona, M.; Rieß, B.; Grötsch, R. K.; Löhrer, F. C.; Wanzke, C.; Käsdorf, B.; Bausch, A. R.; Muller-Buschbaum, P.; Lieleg, O.; Boekhoven, J. Non-equilibrium dissipative supramolecular materials with a tunable lifetime. *Nat. Commun.* **2017**, *8*, 15895, DOI: 10.1038/ncomms15895.

(149) Schwarz, P. S.; Laha, S.; Janssen, J.; Huss, T.; Boekhoven, J.; Weber, C. A. Parasitic behavior in competing chemically fueled reaction cycles. *Chem. Sci.* **2021**, *12*, 7554–7560, DOI: 10.1039/d1sc01106e.

(150) Deng, J.; Walther, A. Programmable and Chemically Fueled DNA Coacervates by Transient Liquid-Liquid Phase Separation. *Chem* **2020**, *6*, 3329–3343, DOI: 10.1016/j.chempr.2020.09.022.

(151) Chen, Y.; Erickson, H. P. Rapid in vitro assembly dynamics and subunit turnover of FtsZ demonstrated by fluorescence resonance energy transfer. *J. Biol. Chem.* **2005**, *280*, 22549–22554, DOI: 10.1074/jbc.M500895200.

(152) Llaneras, F.; Pico, J. Stoichiometric modelling of cell metabolism. *J. Biosci. Bioeng.* **2008**, *105*, 1–11, DOI: 10.1263/jbb.105.1.

(153) Hofmeyr, J. H. S.; Cornish-Bowden, A. Regulating the cellular economy of supply and demand. *FEBS Lett.* **2000**, *476*, 47–51, DOI: 10.1016/S0014-5793(00)01668-9.

(154) Brand, M. D. Regulation analysis of energy metabolism. *J. Exp. Biol.* **1997**, *200*, 193–202, DOI: 10.1242/jeb.200.2.193.

(155) Weißenfels, M.; Gemen, J.; Klajn, R. Dissipative Self-Assembly: Fueling with Chemicals versus Light. *Chem* **2021**, *7*, 23–37, DOI: 10.1016/j.chempr.2020.11.025.

(156) Donau, C.; Späth, F.; Stasi, M.; Bergmann, A. M.; Boekhoven, J. Phase Transitions in Chemically Fueled, Multiphase Complex Coacervate Droplets. *Angew. Chem. Int. Ed.* **2022**, e202211905, DOI: 10.1002/ange.202211905.